Design and Optimization of Lithium-Ion Batteries for Electric-Vehicle Applications

by

Nansi Xue

A dissertation submitted in partial fulfillment
of the requirements for the degree of
Doctor of Philosophy
(Aerospace Engineering)
in the University of Michigan
2014

Doctoral Committee:

Associate Professor Joaquim R. R. A. Martins, Chair
Professor Wei Lu
Professor Anna G. Stefanopoulou
Professor Margaret S. Wooldridge

To my parents, who have given me so much.

ACKNOWLEDGMENTS

Many people have helped me in my pursuit of the doctorate degree. First and foremost, I would like to thank my advisor, Professor Joaquim R.R.A. Martins for his continued guidance and support throughout my Ph.D. You gave me a chance when I was running out of options. Your insight and dedication have always been a source of inspiration for me. And your self-deprecating humor certainly made long group meetings much more bearable.

Special thanks go to Professor Wei Shyy and Professor Werner Dahm, who got me interested in pursuing a graduate degree and helped me across the finish line. I would also like to acknowledge my committee, Professor Wei Lu, Professor Anna Stefanopoulou and Professor Margaret Wooldridge, for their help and input that went into this thesis.

My research work would not have gone so smoothly if not for my fellow MDOLab-mates, especially Wenbo Du, John Hwang and Peter Lyu. All the best in your pursuit of academic, career and personal success. To my housemates, Lynn and Yunyuan, thank you for all the road trips, golf sessions, pig-outs and sports days. You are my closest to a family on this side of the Pacific Ocean, and families don't say goodbyes.

Lastly, I owe everything to my parents, and no amount of words can express my gratitude to you. As I move foward to the next chapter of my life, I will continue to give it all and live my life to the fullest, just like you have taught me.

TABLE OF CONTENTS

Chapter

LIST OF FIGURES

LIST OF TABLES

LIST OF ABBREVIATIONS

ALPSO	augmented Lagrangian particle swarm optimization
DOH	degree of hybridization
EV	electric vehicle
GHG	greenhouse gases
ICE	internal combustion engine
KKT	Karush–Kuhn–Tucker
MCMB	mesocarbon microbead
MEA	more electric aircraft
OCV	open circuit voltage
PHEV	plug-in hybrid electric vehicle
SEI	solid electrolyte interface
SOC	state of charge
SQP	sequential quadratic programming
SNOPT	Sparse Nonlinear OPTimizer
UAV	unmanned aerial vehicle
XDSM	eXtended Design Structure Matrix

LIST OF SYMBOLS

Electrochemistry variables

a	interfacial surface area
A	cross-section area of an electrochemical cell
b	material unit cost
c	salt concentration in electrolyte
c_s	salt concentration in solid matrix
D	diffusion coefficient of electrolyte
D_s	diffusion coefficient of solid matrix
$f_\pm$	mean molar activity coefficient of electrolyte
F	Faraday's constant
i_n	transfer current density at the surface of active material
i_o	exchange current density
i_2	current density in electrolyte
l	thickness
m	number of electrochemical cell in parallel
n	number of electrochemical cell in series
Q	charge capacity
R	universal gas constant
T	temperature
U	surface overpotential
α_a, α_c	anodic and cathodic transfer quotient
ϵ	volume fraction
κ	ionic conductivity in electrolyte
σ	ionic conductivity in solid matrix
Φ_1	potential in solid matrix
Φ_2	potential in electrolyte
ρ	material density
Subscripts	
o	initial state value
s	value in solid matrix
$+$	positive electrode
$-$	negative electrode

Optimization variables

A	Jacobian of constraints w.r.t. design variables
c_j	inequality constraints

$\hat{c}_k$	equality constraints
g	gradient vector of objective w.r.t. design variables
p^i	best position of the ith particle
p^g	global best position
r_1, r_2	random numbers between 0 and 1
s	solution to the quadratic subproblem in SQP
V	velocity of particle in design space
w_0	inertia weight in ALPSO
w_1, w_2	confidence parameters in ALPSO
W	estimate of second-order derivatives in SQP
$\boldsymbol{x}$	position of particle in design space
Δt	time step value in ALPSO, normally taken to be 1

ABSTRACT

Design and Optimization of Lithium-Ion Batteries for Electric-Vehicle Applications

by

Nansi Xue

Chair: Joaquim R. R. A. Martins

Development of alternate energy storage systems for transportation use has been driven by a combination of environmental preservation, fossil fuel price volatility and energy security concerns. Lithium-ion battery has emerged as a favored choice, however its energy density is still orders of magnitude lower than the fossil fuel. There is significant room for improvement in the battery cell and electric vehicle system designs. The objective of this thesis is to automate the design optimization of the lithium-ion battery pack. To achieve this goal three separate optimization problems were formulated to provide guidelines on the cell parameters at optimal solutions. The single cell design optimization is able to quantify the variations of morphological parameters as a constant active mass ratio; the plug-in hybrid vehicle battery design demonstrates an automated design process that considers realistic performance constraints; the multi-cell design approach minimizes the battery pack mass by utilizing separate cell designs to satisfy different constraints. The usefulness of the current framework can be further enhanced by considering various aging mechansims and to perform a design-control coupled multidisciplinary optimization.

CHAPTER 1

Introduction

1.1 Motivation

People's mobility has been significantly enhanced in the last two centuries by the invention of new means of transportation, such as automobiles and airplanes. Due to their higher speeds, these inventions have shortened the travel time across both continents and oceans. While these means of transportation allow us to reach all corners of the world, they are energy intensive and depend primarily on fossil fuels. In the past half century or so, humans' demand for fossil fuels has steadily climbed, as both the larger population and their economic prosperity has increased.

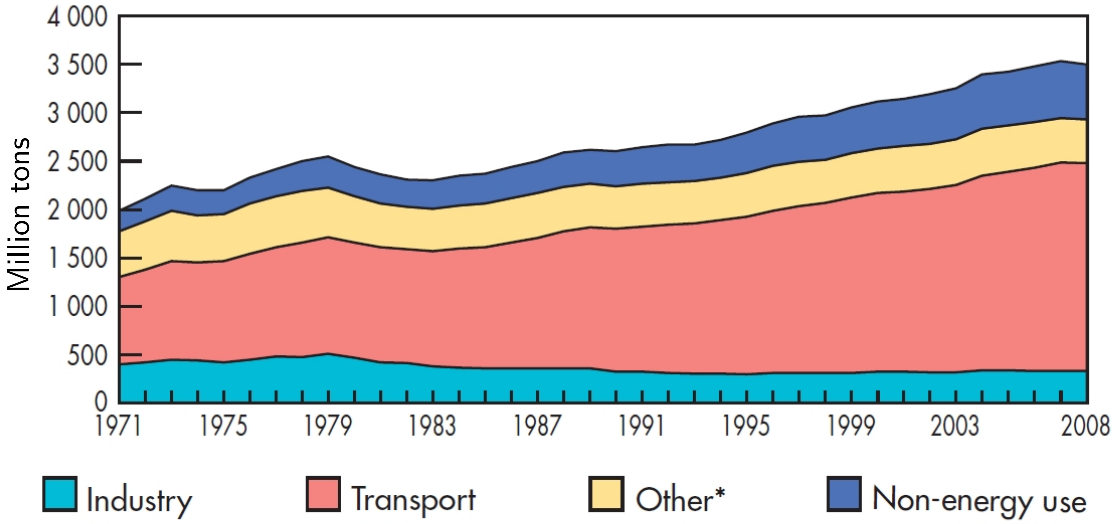

Figure 1.1: Total oil consumption by sector from 1971 to 2008 [1]. 'Other' includes agriculture, commercial and public services, residential oil consumption.

The rise in fuel demand is shown in Figure 1.1. In 2008, 3502 million tons of oil were consumed globally, and a significant portion of it (61.4%) was used for transport [1]. In 1971, transport only accounted for 45.3% of world oil consumption. For countries without their own reserve, or countries that do not produce enough oil, importing oil is the only option to sustain domestic demand. Dependence on foreign oil is most evident in the United States, where foreign oil accounted for more than one quarter of the world's crude oil import in 2008 [1]. Such dependence on foreign oil makes a country vulnerable to volatility in foreign oil supplies, potentially leading to international crisis such as the oil embargo of 1973.

Table 1.1: Net importers of crude oil (2008 Data) [1]

Net importer	**Weight (10^6 tons)**
United States	564
Japan	199
P. R. China	175
India	128
Korea	116
Germany	106
Italy	88
France	83
Spain	61
Netherlands	57
Others	514
Total	**2090**

Consumption of such large quantities of fossil fuels for transportation releases an equally large amount of greenhouse gases (GHG) as well. GHG have been blamed as the main cause of anthropogenic global warming. In 2011, transportation accounted for 28% of US primary energy consumption, 93% of which came from petroleum [10]. This directly translates to 28% of GHG emissions [11]. The ability to control the amount and the sources of energy used for transportation can result in a significant reduction in the amount of GHG released into the atmosphere as well.

The difficulties in controlling the GHG emissions and the over-dependence of fossil fuels play major roles in shaping the future of transportation. The impacts of these factors are most evident in the air transport industry. In the past 30 years, great strides have been made to make commercial airliners much more efficient by lowering the energy used per passenger mile traveled and by increasing the aircraft utilization factor [12]. However, the improvement in efficiency has been offset by the rising fuel costs. The crude oil prices have risen from US$20 per barrel from 1985 to the peak price of US$140 in 2008. The seven-

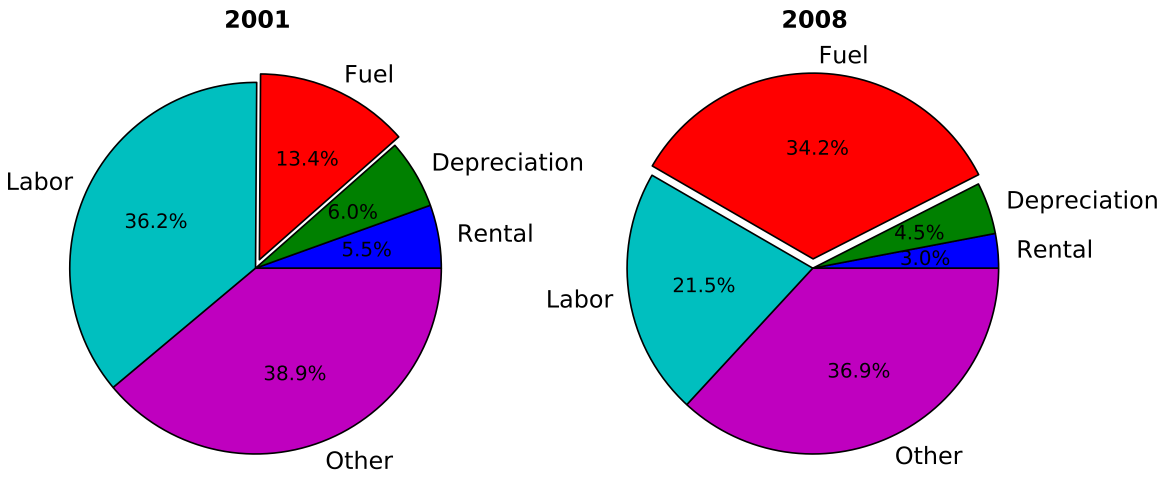

Figure 1.2: The fuel portion of direct operating costs of major North American airlines has increased significantly due to rising fuel costs [2]

fold increase in oil prices drastically increased the fuel portion of overall aircraft operating costs. As shown in Figure 1.2, fuel cost has increased from 13.4% in 2001 to 34.2% in 2008 for all major North American airlines. The net profit margins for airline industry globally were negative for six of the eight years in the corresponding time span [13]. The total fuel-related expenses for 2013 is expected to be about USD $213-billion, while the total profit is forecast to be about USD$ 11.7-billion (September 2013 forecast [14]), thus making the profit margin slim and extremely sensitive to fuel cost fluctuations.

While the air transport industry currently produces only 2% of anthropogenic CO_2 [15], the growth of air industry makes it one of the fastest growing sources of GHG. The problem is further compounded by the altitude effect of GHG. The aircraft emissions of NO_x at cruise altitude increase the production of ozone in the upper troposphere. The net effect is a higher radiative forcing than if the NO_x were emitted at lower altitudes. This increase in the contribution towards climate warming has been estimated to be 2–4 times the contribution of NO_x emissions at sea level [15].

The initiative to move away from using fossil fuels as the energy source for transport use, therefore, arises from the need to address the following concerns:

Energy security: reduce dependence on foreign oil and to sustain development while facing decreasing available resources.

Environmental conservation: sustain development without negatively impacting the environment.

Revenue protection: maintain profitability and reduce the operating costs by insulating against fluctuating fuel prices.

To address these issues, various green technologies, such as EVs, battery technology, and alternative propulsion systems have gained prominence. The development has been most obvious in the automotive industry, due to the need to improve vehicle fuel efficiency and to satisfy increasingly stringent emission standards. Spurred by the feasibility of hydrogen fuel cells and development of higher energy density batteries, EVs have been demonstrated as possible successors of traditional vehicles operating with an internal combustion engine (ICE). Various energy carriers are available to power EV of different architecture. Section 1.2 will explain various types of EVs, while Section 1.4 will discuss more about various energy storage systems.

One of the main advantages of electric-powered vehicles is the significantly lower operating costs compared to ICE powered vehicles. Table 1.2 shows an example comparing the cost of flying a piston-engine general aviation aircraft and a theoretical electric aircraft of the same design.

Table 1.2: Comparison of flying cost for an electric aircraft vs. a piston-engined aircraft. Electricity cost obtained from Michigan Public Commission Service [4]

Description	**Value**
1 gallon of 100LL fuel	35.3 kWh
100LL fuel cost	$6.63/gal (DTW price)
Unit cost of 100LL fuel	18.78 cents/kWh
MI electricity cost (09/2013)	7.05–18.37 cents/kWh
Electric drive system efficiency	90%
Aircraft engine at achieves .45 brake s.f.c.	30%
Decrease in flying cost due to electrification	3–8× lower

Electric powertrains are much more efficient than a piston-engines, converting up to 90% of the energy to useful shaft power. The cost of electricity varies depending on the local supplier, but it is either comparable or significantly lower than the cost per unit energy of aviation fuel. This results in 3–8 times lower operating cost from a purely energy perspective. With ever increasing fuel prices, the economic benefit of electrification of vehicles is only going to increase as well.

While EVs do not produce any in-situ pollutants, the electricity powering the vehicle is a formed of processed energy that has to be produced off-site. In terms of emissions produced, an EV is only as clean as the method used to produce the electricity. In the US, 67% of electricity is generated by fossil fuels, 37% of which is produced from coal [16], the dirtiest of all electricity production methods. While the electricity grid production methods vary across the country, studies have shown that the amount of emissions from the least clean electricity grid is comparable to the best non-hybrid vehicles, while the emissions from the clean grid is much less than the amount produced from hybrid vehicles [17]. Therefore, in addition to financial benefits, EVs can reduce transport-related pollution as well in countries where most of the energy comes from nuclear or renewable energy sources.

Large transport electrical aircraft are not feasible with current battery and electric propulsion technology. The current generation batteries cannot be used to power large airliners due to the low energy density. Therefore the development of electric aircraft has been restricted to small general aviation aircraft and partial electrification of pneumatic and hydraulic systems. While the development of electric flyers have been limited by technology, the benefits of such aircraft should be obvious. Even with the assumption that the future electric aircraft have the same level of emissions as current aircraft, the simple act of transferring emission sources for aircraft at altitude to ground-based power plant will help to reduce the net effect of GHG emissions on the climate.

1.2 Hybrid/Electric Vehicle Designs

EVs have existed for more than a century by now. In 1899, a Belgian electric vehicle powered by lead-acid battery was able to reach 30 m/s [18]. However, the lack of progress in batteries hindered the development of EVs and it was not until recently that electric and hybrid vehicles re-emerged. EVs are powered entirely by electric propulsion systems, while hybrid vehicles have two or more power sources—normally an ICE coupled to an electric motor/generator powered by an electric energy storage system. A useful way to define the powertrain characteristics of such vehicles is to use degree of hybridization (DOH), which is defined as [19]:

$$\text{DOH} = \frac{\text{electric motor power}}{\text{electric motor power} + \text{IC engine power}} \tag{1.1}$$

Depending on the DOH of the vehicle, a hybrid vehicle can be classified into the following groups:

Mild hybrid: vehicles which rely on secondary energy storage systems to assist ICE. A moderately-sized battery is normally used as the second power source. The battery has limited discharge range, low power output, and it offers slight fuel economy improvement. This type of vehicle requires little modification to the existing vehicles and incur the lowest incremental cost among the hybrid options. Vehicles belonging to this category of hybrids include Toyota Prius and Honda Insights.

Plug-in hybrid: vehicles with all-electric driving range. An ICE or turbine is available for extended range or to recharge the battery. They use a large battery pack with high power output that can be charged directly from the grid. Such vehicles offer significant fuel savings and reduced GHG emissions for short commutes. However, large battery packs incur significant additional vehicle costs and weight. GM's Chevrolet Volt and Ford C-Max Energi are two of the commercially available plug-in hybrid electric vehicle (PHEV)s.

Electric vehicle: vehicles with only all-electric driving capability. These use an extremely large battery pack, and can only be recharged with electricity from the grid. These vehicles have zero in-situ emissions, but they are currently either much more expensive than conventional vehicles or have very limited range. Nissan Leaf and Model S are both EVs that contain large lithium-ion battery packs to provide all of the onboard energy.

While the system design of an all-electric vehicle is straightforward, there are various ways to configure the drivetrain components of a hybrid vehicle. In a serial configuration, the electric motor is the only component connected directly to the drive-train. The decoupling of the engine from the wheels means it can always operate at an optimum torque and speed regime. It performs best for low-speed, high-torque applications, such as buses or other urban work vehicles. However, it is less efficient, as mechanical energy from the ICE needs to be converted to electrical energy in the generator and then converted back to mechanical energy again.

The parallel configuration allows wheel to be driven by either the electric motor, the ICE, or both. The benefit of this system is redundancy, which is important for both civilian and military vehicles. However, direct connection between the engine and the wheel means that the ICE may not operate at its most efficient regime, thereby limiting its efficiency.

Alternatively, a power-split configuration can be employed in which neither the ICE nor the electric motor are directly connected to the drivetrain. A planetary gear is used to transfer power from either the ICE or the motor to power the vehicle. Such a system offers increased efficiency and reduced emissions over the previous two systems. However, design complexity due to the coupling of the various sub-systems adds to the cost and control strategies required.

Hybrid or electric vehicles offer many advantages over the ICE-powered vehicles. The additional drivetrain components enable various operating modes to be engaged to maximize vehicle efficiency. Some of the benefits of hybrid and electric vehicles are [20]:

Idle-off: the average vehicle spends 20% idling, so turning off the engine at idle can significantly reduce fuel consumption by 5–8%. A 3–5 kW electric motor can spin the engine up to idle speed in less than .5 seconds, thus enabling a smooth transition.

Regenerative braking: the electric motor and energy storage system can be used to recapture some of the energy that would otherwise be lost during braking. 5–10% fuel savings can be expected, though the benefit is a function of electrical component sizes, and requires a brake-by-wire system and an additional clutch between engine and motor.

Engine downsizing: a smaller engine is usually more efficient for a given load, as it has lower frictional, heat, and pumping losses. Hybrid systems can be used to augment engine power during peak demand, thus allowing a smaller engine without loss of performance. Benefit of downsizing is proportional to electrical component sizes. A 10-20 kW electric motor and corresponding energy storage system coupled with a downsized engine can provide 5–15% fuel savings over an ICE of similar peak power.

Improved engine efficiency: a hybrid system can keep the engine at higher loads and minimize operation at less efficient modes. For example, the vehicle can be powered by the electric motor alone at low speeds and loads, and highway driving can be powered by the ICE at lower speed. In addition, hybrid systems allow integration of innovative engine designs, such as the Atkinson cycle gasoline engine.

Electrical accessories: most accessories (air conditioning compressor, water pump, power-steering pump) are currently driven directly by mechanical connections to engines. This creates inefficiency, as accessory speed varies with engine speeds. Hybrids allows accessories to be powered by electrical energy storage systems directly, allowing their operation to be independent from the ICE.

Hybrid/electric vehicles tend to be more expensive due to the additional drivetrain components. Lithium-ion battery packs are especially costly, and can account for up to 25% of the total vehicle cost in an all-electric vehicle, such as Nissan Leaf. EVs are a relatively new technology that just established its foothold in the mass market. As its design becomes more refined and gains wider acceptance, the volume of the battery production should increase accordingly, decreasing the cost [21].

The development of hybrid/electric vehicles in the past two decades have been the results of better batteries and tighter integration of electric drive systems with the vehicles. However, hybrid vehicles also face competition from improvements in ICEs. ICEs may be inefficient, viewed as inherently dirty, and exacerbate dependence on foreign oil. However, they also offer long driving range, are quick to refuel. Recent improvements both in reduced emissions and increased fuel economy limit the incremental improvements offered by alternative propulsion systems [20]. More sophisticated control strategies and additional electric components could improve the hybrid efficiency and at the same time provide the smoothness and adequate performance required by drivers. Optimizing all the interactions in a hybrid system would demand a great deal of engineering design and software development, but the benefits of improved efficiency could prove to be worthwhile in the long term [20].

1.3 Hybrid/Electric Aircraft Designs

While the development of electric aircraft has been encouraged by the recent progress in battery energy density, the idea has been proposed for close to a century. Patents for electric airplane propulsion systems have been filed as early as 1924 [22]. The first manned electric flight was achieved by Heino Brditschka in 1973, when he successfully flew in an electric variant of the HB-3 motor-glider powered by Ni-Cd batteries. While the flight only lasted 15 minutes, it demonstrated the feasibility of electric aircraft.

There are numerous advantages to using electric propulsion in aircraft. Electric propulsion introduces the possibility of using multiple small electric motors instead of large engines, thereby creating a distributed propulsion system [23]. Such a system would increase safety through redundancy. In addition, the smaller cross-section areas of multiple propulsion units would enable embedding them into the airframe, providing additional aerodynamic benefits, such as boundary layer ingestion, and reducing aircraft weight [24, 25].

The biggest issue hindering the development of electric aircraft is undoubtedly the energy density limitation of batteries. The energy density of current batteries is still orders of magnitude lower than that of jet fuel (0.54 MJ/kg for lithium-ion batteries versus 43.02 MJ/kg for Jet-A fuel). While ground-based vehicles can manage the increased weight due to electrification without drastic reduction in performance, the aircraft is much more sensitive to mass increase. To demonstrate how the additional battery mass affects the performance of the aircraft, a simplified equation based on conservation of energy is derived for electric aircraft to examine how battery energy density affects its range. The energy required for flying can be approximated by:

$$\begin{aligned} E_{tot} &= E_{grav} + E_{ke} + E_{range} \\ M_{batt}\tilde{E}_{batt} &= Mgh_{cruise} + \frac{1}{2}MV_{cruise}^2 + \frac{1}{2}\rho V_{cruise}^2 C_D S_{ref} R \end{aligned} \tag{1.2}$$

Table 1.3: Battery mass required to provide the kinetic and gravitational potential energy for a Boeing 737-800 to reach cruise altitude and speed [5]

B737-800 specifications	**Values**
Maximum landing weight	66349 kg
Maximum fuel capacity	26020 L
Maximum fuel mass	21076 kg
Eing area	124.58 m^2
Cruise altitude	10668 m
Cruise speed (IAS)	230 m/s
Cruise drag coefficient	0.03
Energy required to reach cruise altitude	8.70 x 10^3 MJ
Lithium-ion battery density	150 Wh/kg
Battery mass required to reach cruise altitude	1.61 x 10^4 kg

i.e., the total energy required by the aircraft is the sum of the gravitational potential energy at the cruising altitude (E_{grav}), the kinetic energy at cruise speed (E_{ke}), and the energy required to overcome drag during steady level flight (E_{range}). This is also the total amount of energy provided by the battery of mass $\mathrm{M_{batt}}$ with an energy density of $\tilde{\mathrm{E}}_{\mathrm{batt}}$.

Using Equation (1.2) and the data for a Boeing 737-800 aircraft, we perform the calculation listed in Table 1.3, which shows the battery required to reach the start of cruise.

Table 1.3 shows that the minimum battery mass required to reach cruise altitude and speed (assuming perfect propulsion efficiency) is already more than 2/3 of the maximum fuel mass that a Boeing 737-800 can carry. This suggests that even when taking into account the increased efficiency of the electric propulsion systems, the current generation batteries alone are unable to provide all the energy needed by a airliner for extended operation.

The battery mass as a fraction of the maximum landing mass for the Boeing 737 is plotted as a function of the achievable range of the aircraft in Figure 1.3. We show the variations of the range with respect to the energy density for the energy density of current lithium-ion batteries as well as the theoretical values of future battery systems. It is clear that in order for electric passenger airliners to be viable, the battery energy density has to be much higher than the current state of the art. However, even with the theoretical energy density of Li-air battery systems (which has the same energy density as Jet-A fuel), the proposed electric Boeing 737 is still unable to match the maximum range of the conventional 737. An electric aircraft with the same fuel mass and powered by lithium-air battery can only achieve 1/4 of the maximum range of the as the conventional B737-800. This is due to the fact that unlike a conventional aircraft, which become lighter as fuel is consumed, the battery mass remains constant during the flight. The additional mass of the battery requires the aircraft to produce more lift in order to maintain cruise condition, which in turn leads to reduced range.

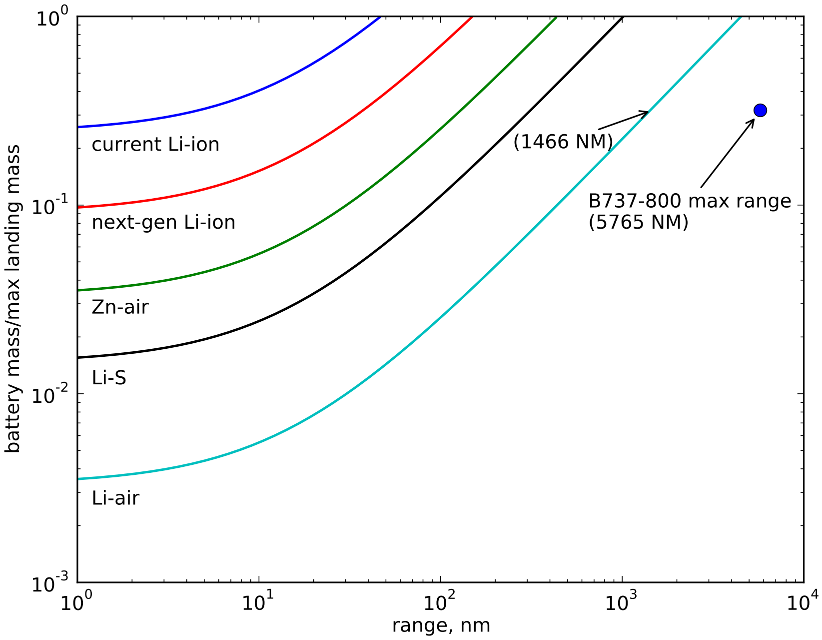

Figure 1.3: Fuel mass fraction as a function of range for different types of battery. The range of a proposed electric aircraft with the same fuel mass fraction and powered by lithium-air battery is about 4300 nautical miles shorter than that of the conventional B737-800.

One of the main issues challenging the wisdom of developing of an electric aircraft is the lack of energy recapture during flight. A hybrid system on a ground-based vehicle is able to regenerate energy during braking that would otherwise be lost in a conventional vehicle. However, there is no such advantage in an electric aircraft. The amount of energy that can be recuperated by allowing propellers or fans to wind-mill during descent is small, and since this happens only at the end of the flight, it would not be useful for extending the range of the aircraft. The problem is further compounded by the improvement in aircraft efficiency in terms of energy used per passenger mile traveled [12]. Unlike an automobile, the flight path and cruise conditions of an airliner are predetermined, and therefore the engine can be designed to be operate at optimum efficiency around cruise condition. Any off-design flight conditions can be accounted for in the design phase by utilizing a multi-point design method to maximize the aircraft efficiency over a range of flight plans [26]. Therefore, the improvement in aircraft efficiency from the energy perspective is likely to be even lower compared to the gains in ground-based electric vehicles.

Currently, the electrification of aircraft is limited to small general aviation aircraft and unmanned aerial vehicle (UAV)s. The electrification of large passenger aircraft is non-existent due to the lack of a suitable high-energy density charge carrier. The airline industry is currently promoting more electric aircraft (MEA) to improve aircraft performance and reliability. This results from the growing power requirements due to additional avionics systems, increased use of electro-mechanical actuators, and increased use of info-entertainment systems. MEA aims to replace onboard hydraulic, pneumatic and mechanical systems with the electrical equivalents in an effort to reduce weight, system complexity, and maintenance cost [27, 28].

To realize the full benefit afforded by an electric propulsion system, a complete aircraft redesign that takes advantage of future technologies should be considered. Boeing considered a 737 equivalent hybrid concept aircraft as on of the NASA N+3 studies [29]. The aircraft has strut-braced high aspect ratio wings and uses geared turboprop engines for propulsion. It is estimated that the battery density needs to be more than 750Wh/kg in order for the hybrid system to be viable. NASA developed a hybrid blended-wing body aircraft concept that takes advantage of distributed propulsion systems [23, 30]. Benefits of such a distributed propulsion concept include boundary layer ingestion, low noise level due to lower fan pressure ratio, and lower wing structural weight due to better weight distribution. While these aircraft designs demonstrate the possible benefits and improvements in future transport aircraft, they will remain as concepts until technologies such as high-capacity batteries and superconducting motors become viable.

1.3.1 General Aviation Aircraft

Electric-powered general aviation aircraft concepts have been developed as battery technology has improved. Numerous electric general aviation aircraft are already available on the market. In addition, various hybrid aircraft demonstrators have been produced as well. Just like in road vehicles, there can be different configurations of hybrid-electric systems. The DA36 E-Start motor glider, is the world's first aircraft with a serial configuration propulsion system and was showcased in 2011 [31]. Flight Design—a German company—coupled a 40 hp motor with a 115 hp Rotax 914 aircraft engine in a parallel configuration for a light-sport aircraft [32]. Electric aircraft are generally characterized by high aspect ratio wings, lightweight construction, low cruising speed, and limited endurance and range. The performance of the aircraft is limited by the size and energy capacity of the battery pack, which can easily make up to 1/3 of the empty aircraft weight [33]. However, given the low op-

Table 1.4: Results of the top two teams of the NASA Green Flight Challenge [6, 7]

Team	**Pipistrel**	**e-Genius**
Empty mass (kg)	632 kg	-
Battery mass (kg)	520 kg	-
Energy used (kWh)	65.4	34.7
Distance (miles)	195.9	193.7
Speed (mph)	107.4	105.7
ePMPG	403.5	375.7
Noise at 250 feet (dB)	71.1	59.5

erational cost of electric flying—as highlighted in Table 1.2—there is potential for electric aircraft as a mode of short-range transportation in the near future. The concept of utilizing electric aircraft as an on-demand vehicle has been explored [34, 35, 36]. Studies show that these aircraft will have significantly lower operating cost compared to existing general aviation aircraft, and they can be used for trips that are unprofitable for airliners and take too long in road vehicles. However they are likely to remain as low-range variants with limited payload capacity until battery technology improves dramatically. Careful integration of the propulsion system with the airframe that can represent significant variation from existing airframe is needed to maximize performance.

NASA organized a Green Flight Challenge in 2011 to demonstrate the feasibility of long distance sustainable flight. The entry aircraft was required to fly 200 miles at 100 mph while using less than one gallon of gasoline (or equivalent energy) per passenger. The top two winning aircraft were both electric-powered, with the winning aircraft achieving 403.5 equivalent passenger MPG. Both aircraft are much quieter than a typical piston-engined aircraft. The noise produced by a typical general aviation aircraft is about 92 dB at 200 feet away, or more than 20 dB higher than the noise produced by the electric aircrafts at 250 feet away.

The main benefits of electric general aviation aircraft are lower operating cost, improved efficiency, and reduced noise levels. However such aircraft requires significant redesign from existing airframes in order to be practical and take full advantage of electric propulsion. The winning aircraft of the NASA Green Flight Challenge, for instance, has a battery pack that weighs nearly as much as the empty weight of the aircraft [7] as shown in Table 1.4, yet it is still limited to a range of about 400 km. The degradation and loss of battery capacity is also a major issue that needs to be addressed.

1.3.2 Unmanned Aircraft

The propulsion systems and fuel mass for small UAVs can exceed 60% of the vehicle mass [37], rendering them more sensitive to propulsion system mass change. In addition, the decreased aerodynamic efficiency of these vehicles at lower Reynolds number and decreased efficiency of power/propulsion systems at smaller scale makes the efficiency of the power systems very critical to UAV design.

Electric propulsion is a better option than ICE for reconnaissance and surveillance UAVs due to lower required maintenance and lower noise. However, any benefits of a hybrid or electric system must be weighed against the loss in payload due to increased energy storage system mass. For small UAVs, two important criteria often determine the performance: loiter time (related to active operation time), and rate of climb (related to vehicle survivability and safety). These two criteria are at odds at each other in an electric UAV, as one maximizes the energy, while the other maximizes the power. Optimizing for either objective results in the other being zero [38]. Various research groups have examined innovative ways to design electric or hybrid UAVs, as they offer increased loiter time and range compared to an electric-powered one and reduced acoustic and thermal signatures over a gasoline-powered one [39]. Multiple propulsion systems also allow for more creative designs, such as the tail-dragger UAV proposed by Aksugur and Inalham [40]. Such designs can achieve two hours of flight endurance and required only three minutes for a vertical take-off and landing. A comprehensive review of hybrid propulsion systems for small UAV is given by Hung et al. [41].

The design of an electric UAV is a multidisciplinary problem that includes aerodynamic, structural, electric and performance analyses, and naturally lends itself to multidisciplinary design optimization [42]. A fine balance between the onboard energy availability and achieving the specific operational goals is needed for the best possible design. Future design of an electric aircraft can potentially take advantage of the structural rigidity of batteries and use the energy storage system as part of load-bearing structures [43, 44, 45]. Combining structure and energy functions into a single material could offer improvements in system performance that would otherwise be impossible through separate individual system optimizations. This is a long-term challenge that requires development of new procedures to examine the multi-functional efficiency of such system. Problems such as adequate load transfer from the structure through the energy storage materials and safety concerns of battery performance under mechanical stress must be addressed as well [44].

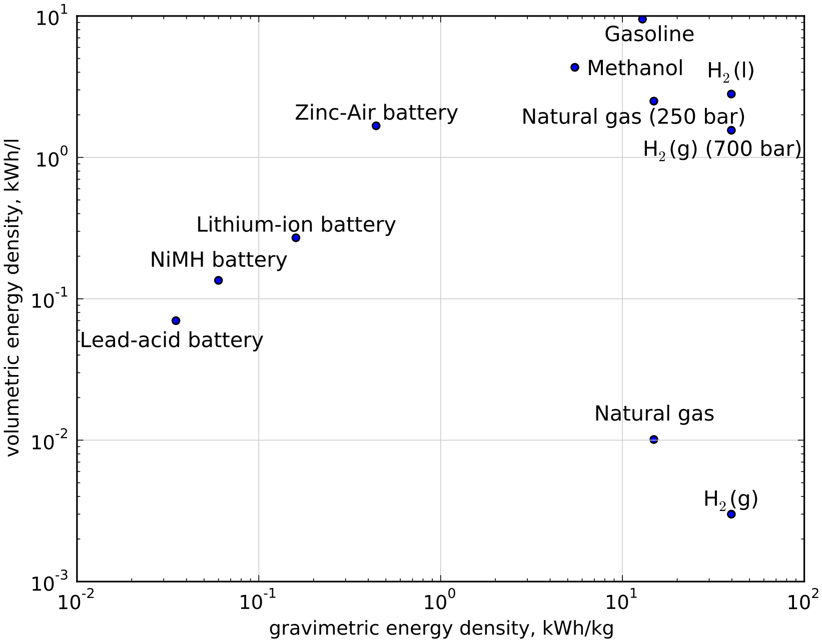

Figure 1.4: Energy density of representative energy storage systems

1.4 Energy Storage Systems

One of the most crucial aspects of a hybrid/electric vehicle design is the onboard energy storage devices. There are various options available for energy storage. Depending on the DOH of the vehicle, the energy storage system can be either battery, fuel-cell, supercapacitor, or flywheel. Less common choices such as pneumatic power are available as well [46]. Figure 1.4 shows the comparison of energy density between various systems.

Among the various energy storage systems, batteries in particular have been developed to power a diverse range of applications due to their ease of use and availability of existing electric infrastructure. The concept of the battery is simple, but the energy density of batteries have not been able to keep pace with the progress in electronics that follow Moore's law. This is mainly due to the lack of suitable electrode and electrolyte materials, and the difficulty in ensuring compatibility at the interfaces. Nevertheless, there have been some breakthroughs in new materials recently, most notably the development of various lithium-ion technologies that are the focus of this thesis.

Much progress has been made in the numerical modeling of battery systems to examine the physical phenomena occurring within the electrochemical cell, with varying levels of fidelity and computational cost. Single particle models represent each electrode as a single spherical particle [47, 48]. Liaw et al. [49, 50] developed an equivalent circuit model and subsequently used it to examine the impact of variation in cell properties on overall energy capacity. Solving the simplified algebraic equations of the equivalent circuit model enables real-time estimation of battery state of charge (SOC) and health [51]. Newman et al. [52] developed a pseudo-2D model that uses porous electrode and concentrated solution theories [53]. This is a macroscopic cell model that treats the electrode as a homogeneous continuum. A review of various models for predicting cycling performance was written by Santhanagopalan et al. [54]. Subsequently, various authors have studied the effects of microstructural variations on transport properties and cell performance using micro-scale models [55, 56, 57]. Additional work has been done to describe various degradation mechanisms and side reactions occurring within the cell [58, 59, 60, 61, 62] to account for differences in performance between ideal electrochemical cells and practical results.

Currently, there is yet to be one alternative energy storage system that is a clear-cut choice to replace fossil fuels. Despite the improvement in new electrode materials, battery energy densities are still orders of magnitude lower than that of fossil fuels. Hydrogen fuel cells can satisfy both the high energy density and the zero GHG emission requirement, but they have yet to be economically viable, as the electrode requires precious metals and the infrastructure cost of hydrogen fuel stations is extremely high [63]. Continued research and development on both the material science and the systems engineering fronts is crucial if we are to shift away from fossil fuels and towards a more sustainable energy future.

1.4.1 Lithium-Ion Batteries

Lithium-ion batteries are a family of rechargeable batteries that shuttle lithium ions between the two electrodes during cycling. These batteries have emerged as the preferred energy storage device for EV applications due to their relatively high energy density compared to other batteries. Lithium-ion batteries are economically more viable than hydrogen fuel cells as the associated infrastructure—a network of charging stations—has a much lower cost compared to hydrogen refuel stations. Lithium is favored as the anode material since it is the most electropositive (standard electrode potential = $-3.04\,\mathrm{V}$ [64]) and it is also the lightest metal (equivalent mass $= 6.94\,\mathrm{g/mol}$ [64]), both of which are essential for high energy density. The lithium-based rechargeable battery was first demonstrated in the 1970s by using lithium metal as the negative electrode and titanium sulphide as the positive electrode [65]. Such a battery system was found to have poor cycling behavior as dendritic growth due to lithium plating upon repeated cycling poses the potential hazards of short-circuiting and explosion. Lithium metal was subsequently substituted by a second insertion material as the negative electrode to avoid lithium plating problems [66]. The lithium-ion battery operates by reversibly incorporating lithium into the active material via an intercalation process, during which the ions are reversibly removed or inserted into a porous host without significantly changing its structure. The family of compounds of the form Li_xMO_2 (where 'M' is Co, Ni, or Mn) was proposed [67, 68] in the 1980s and has since gained wide-spread acceptance as the active material in cathodes.

The current generation of lithium-ion batteries consists of a cathode made of a metal oxide with either a layered structure, such as lithium cobalt oxide, or a tunneled structure, such as lithium manganese oxide. The negative electrode is usually a graphitic carbon. Given its high energy density (5 times greater than that of lead-acid, and twice that of Ni-MH), it has become the standard power source for a variety of electrical devices, from personal electronic devices to vehicles and satellites. In addition, lithium-ion batteries have low self-discharge rate, long cycle life, and a wide operating temperature range [69]. However, lithium-ion batteries are also more expensive than other battery types and require complicated power management units to prevent degradation or thermal runaway due to abusive use. Lack of overcharge or discharge tolerance has resulted in large battery packs with limited useful capacity in order to extend battery cycle life for EV operations. Permanent capacity loss also occurs at elevated temperatures. The high initial costs and restriction on useful capacities resulting in driver range anxiety are two of the biggest obstacles in EV acceptance. To circumvent these problems, lithium-ion battery costs need to be lowered through increased production volume [21] and more sustainable production methods [18]. Useful capacity can be improved with more refined battery design and higher energy density materials.

1.4.2 Future Batteries

The development of next-generation battery systems looks promising, as researchers are exploring multiple ways to increase the energy and power capabilities. Table 1.5 highlights some of the more promising battery chemistries and the theoretical capacities of such battery systems.

Much attention has been focused on increasing the energy density of lithium batteries with new electrode materials. Sulfur has been identified as a potential cathode material as it has the possibility of increasing the energy density by 10 fold over current lithium-ion batteries. Moreover, sulfur is an element that is naturally abundant, non-toxic and inexpensive to obtain [70, 71]. However, development of sulfur-based cathode has been plagued by low active material utilization, poor cycling, and low Coulombic efficiency [72]. Stable cycling behavior of lithium sulfide cathode with a poly-(vinylpyrrolidone) binder was recently demonstrated [73].

Table 1.5: Performance comparison of future battery systems [8]

Battery type	voltage (V)	Theoretical capacity (mAh/g)	Theoretical specific energy (Wh/kg)
Conventional lithium-ion	3.80	155	387
Li-S	2.20	1,672	2,567
Li-air (non-aqueous)	3.00	3,862	11,248
Al-air	2.70	2980	8,100
Zn-air	1.65	820	1,086

On the anode side, silicon has emerged as a viable replacement for carbon-based insertion materials. It has problems of its own as well, such as excessive volume expansion [74], and unstable electrolyte interphase growth on silicon surface [75]. Recent progress has been made by immersing silicon-based anode in a conducting polymer hydrogel [76], thereby creating a three-dimensional network that provides porous volume for expansion, as well as a continuous electrically conductive network.

Lithium-air batteries, which couple a lithium anode with an air cathode, have extremely high theoretical energy capacity that is comparable to that of gasoline. The first lithium-air battery was demonstrated in 1996 [77]. However, desirable rechargeable behavior has yet to be achieved. In order to achieve the desired performance for an Li-air battery, designers need to master both the lithium and oxygen electrodes and overcome a multitude of scientific and technical challenges [78].

One of the key areas of battery development has been application of nano-technology. Nano-materials improve battery performance by increasing the interfacial surface area and shortening the diffusion path for ions. They can also alter the reaction pathway in the electrode, increasing capacity and life cycle in general [79]. However, batteries based on nanomaterials need to overcome poor packing density and low energy efficiency before becoming viable.

1.4.3 Lithium-Ion Battery Recycling

Since EVs are estimated to make up 7% of the global transportation market by [80], the availability of lithium and other rare metals required for manufacturing batteries and the disposal of lithium-ion batteries will become more critical factors in the life cycle analysis of EVs. Unlike fossil fuel price fluctuations that only affect the running cost of vehicles, raw material prices directly affect the production cost of EVs.

Battery recycling can lead to over 50% saving of natural resources in terms of decreased mineral ore dependency and reduced energy consumption [81]. What is surprising is that lithium recovery is not the impetus for battery recycling. While lithium is the energy carrier in the battery, it makes up only 5–7% of the total battery mass [82]. The average lithium cost associated with battery production is less than 3% of the total battery production cost [83]. The driving force behind battery recycling is the recovery of more precious materials, such as cobalt and nickel. Lithium in batteries is 100% recoverable and technology is not the limiting factor in recycling process. However, it is typically not recovered as recycled lithium costs approximately five times more than brine-based mining process [83]. Current battery production accounts for only 1/4 of the total lithium consumption, and it is expected to increase to 40% by 2020. With price of lithium carbonate tripling in the past decade [84], lithium recycling could prove to be an option to hedge against fluctuations in raw material prices in future.

1.5 Objectives and Outline

Using alternative energy storage systems such as lithium-ion battery to replace fossil fuels grows out of the need to reduce emissions, provide energy security, and improve vehicle efficiency. Given that the most critical factor in determining the performance of the hybrid/electric vehicles and aircraft is the energy density of the energy storage system, it is imperative to maximize the amount of energy available while satisfying the mass, volume and cost constraints for practical applications. There are three ways to maximize the energy content of a battery:

1. Maximize the chemical potential difference between the two electrodes, such that the battery gives the most energy per electron.

2. Maximize the charge capacity of the electrode, such that the mass of reactant per unit of electron is as small as possible.

3. Minimize the non-energy contributing components of the battery.

The first two criteria are inherently chemical properties that depend on the materials used to construct the electrodes. To a large extent, the cell performance is determined by the properties of the material used. Dramatic improvements in the raw battery energy capacity can be achieved through the discovery of new electrode materials such as silicon and sulphur mentioned in the previous section. The third point relates the design and construction of battery to its performance of energy and power, and the problem is there is still a significant gap between theoretical and realizable energy density [85, 86]. The electrochemical cell is a multi-scale, multi-phase system that involves multiple processes occuring simultaeneously. An optimal cell design has to account for the various processes occuring within a cell and find a balance point that minimizes the cumulative effects of these factors. It is difficult to determine the best possible design in a highly nonlinear system such as the electrochemical cell using simple parameteric analysis.

What has been missing is an efficient numerical tool and a comprehensive numerical study to optimize the battery performance with respect to various cell parameters and subject to system-specific constraints. The objective of this thesis, therefore, is to devise a numerical framework that automates battery design and to apply it in the design and analysis of EV systems. By coupling a detailed electrochemical model that simulates all relevant transport processes within a battery cell with nonlinear optimizers, a mathematical framework for the complete and automatic battery optimization is demonstrated. The details of the framework are presented in Chapter 2. Using this framework, three representative battery design problems representing different phases of battery pack designs are investigated.

Chapter 3 presents the design of a single electrochemical cell to maximize its energy density subject to a power constraint. This chapter presents a design problem at the basic cell level and the main objective is to quantify the variations of design variables with respect to different cell power requirement. The design space encompasses all relevant variables, including both morphological variables (electrode thickness, porosity, and particle size) and transport parameters (conductivity and diffusivity). The optimal designs form a Pareto front of maximum cell energy density at constrained power requirements.

The optimization framework is expanded in Chapter 4 to find the optimal design of a battery pack for PHEV operation that minimizes the pack mass, volume or cost. The main motivation is to provide a numerical framework for automated design and analysis of a realistic PHEV battery design problem. The battery pack is made of uniform electrochemical cells that have to simultaneously satisfy performance requirements of energy and power to provide adequate vehicle performance. Additional voltage and current bounds as safety requirements are considered in the design problem formulation as well. Actual federal-testing driving cycles are used to simulate the real-life performance of the optimized battery pack designs.

Chapter 5 examines the possible advantages of a battery pack with multiple cell designs over one with uniform cells. This chapter is motivated by the discrepancies between optimal single cell design and the optimal battery pack cell design in the prveious two chapters. The contribution is to bridge the gap between an optimal cell design intended to perform best at its specific design point and the need of a battery pack to satisfy a range of discharge conditions that depends on the driver throttle input and road conditions. A multi-cell design scheme that considers a two-level design strategy that is outlined in this chapter. The individual cells are optimized based on the battery pack requirement and the combination of the individual cells to best satisfy the battery pack are optimized as well. The situations where the multi-cell design approach outperforms the conventional uniform-cell design are specified.

Finally, the inadequacies and potential for improvements of the numerical framework are addressed in the concluding chapter. Additional details such as cycling stability and cell degradation have not been included in the current framework and qualitative analyses are provided to address these issues. While the battery optimization problems are demonstrated with one type of lithium-ion cell chemistry, generalization of the numerical framework to include other materials is discussed here as well.

CHAPTER 2

Methodology

2.1 Introduction

An optimization framework requires three key components: a useful problem formulation, an efficient optimization algorithm, and an accurate model to evaluate the objective function and constraints. This chapter describes these three components in detail.

2.2 Cell Model

Battery cell cycling behavior is typically nonlinear, since a number of factors influence properties, such as the cell voltage and power output. Typically, as a battery discharges, the open circuit voltage (OCV) of the cell is SOC-dependent. In addition, factors such as activation polarization, concentration polarization, and internal resistance all contribute to the potential drop in the cell [9]. Activation and concentration polarizations are related to the charge and mass transfer kinetics, respectively, and internal resistance is the sum of ionic, electrical, and interfacial resistances. To accurately model the cycling behavior of the cell, a cell model has to account for all the major internal processes occurring between and within the electrodes. Alternatively, an algebraic model that represents cell components with simplified circuit components can be used as well to speed up computation. In the following two sections, both types of models are be described.

2.2.1 Physics-Based Cell Model

A physics-based model that accounts for fundamental transport laws in a pseudo 2-dimensional battery cell is used in this work [52, 87]. Specifically, we model the lithium ion transport in the direction perpendicular to the current collectors in a full lithium-ion sandwich cell,

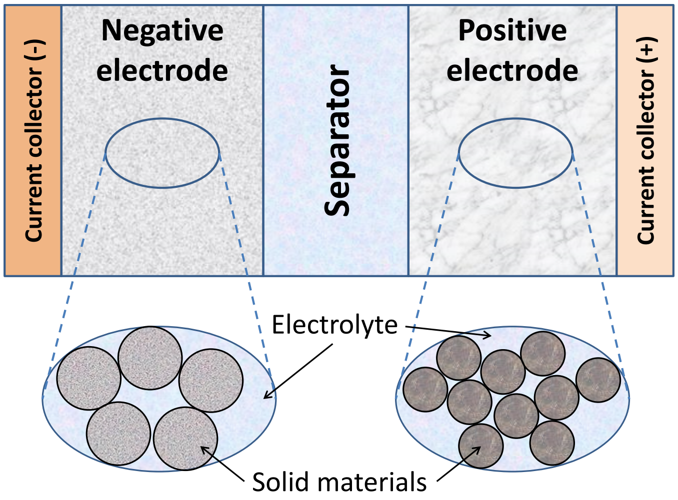

Figure 2.1: Structure of a lithium-ion insertion cell shows three separate regions and two different phases

as shown in Figure 2.1. The cell model incorporates an homogenous electrode formulation [52, 88] with concentrated solution theory [53]. The state variables solved in the model are the ion concentration in electrolyte, c, and in the solid matrix, c_s, the current density in the electrolyte, i_2, the interfacial current density at the solid matrix surface, i_n, and the potentials in the electrolyte and solid phases, Φ_2 and Φ_1, respectively. These state variables in turn provide the cell properties that are used to evaluate the cell energy density and power output.

The governing equations with the associated transport parameters are defined in all three regions of electrochemical cell: the positive electrode, the separator, and the negative electrode. The porous electrodes consist of solid active materials and liquid electrolyte. One key aspect of the pseudo-2D model is that the exact geometric details and microstructrual effects of the electrode are ignored, and instead the electrode is modeled as a continuum medium [52] that is a mixture of both phases. This avoids the additional work of explicitly defining solid and liquid phases and their boundaries. The influence of porosity is instead accounted for using Bruggeman's relation for spherical particles [89]. This relates the effective transport property to the bulk property and the porosity in the form of:

$$K_{\text{eff}} = \epsilon^{1.5} K \tag{2.1}$$

where K in this case is an arbitrary transport coefficient such as diffusivity or conductivity.

The main forces driving ion mass transfer in a cell are 1) the gradient in electrochemical potential, which causes migration, 2) the concentration gradient, which causes diffusion, and 3) the electrolyte bulk velocity, which causes convection. A material balance on the salt in the electrolyte is then given by:

$$\epsilon\frac{\partial c}{\partial t} = \nabla \cdot \epsilon D \left(1 - \frac{d\mathrm{ln}c_o}{d\mathrm{ln}c}\right) \nabla c + \frac{t^o_- \nabla \cdot \boldsymbol{i_2} + \mathbf{i_2} \cdot \nabla t^o_-}{z_+ \nu_+ F} - \nabla \cdot v_{\mathbf{o}} + aj_- \tag{2.2}$$

where the terms on the right hand side represent the diffusion, the migration, the convection, and the reaction rate of the anion in the solution. The electrolyte velocity is usually negligible [90], and the convection term can be ignored. The anion reaction term is zero in the absence of the side reactions, leaving diffusion and migration as the main mass transfer mechanisms. Initial conditions are prescribed for salt concentrations at every location in the cell.

Ion movement is accounted for in both the liquid and solid phases. In the solid phase, only the cations and electrons are mobile in the host matrix. If intercalation-induced stress and anisotropic diffusion are ignored, the transport of ions in the solid phase is given by:

$$\frac{\partial c_s}{\partial t} = \nabla \cdot D_s \left(1 - \frac{d\mathrm{ln}c_o}{d\mathrm{ln}c_s} \nabla c_s\right) + \frac{\boldsymbol{i_1} \cdot \nabla t^o_-}{z_+ \nu_+ F} - \nabla \cdot c_s v_o \tag{2.3}$$

If one further assumes that the conductive additives make the solid material a good electronic conductor and assumes small volume fraction change and uniform spherical particle shape, Equation (2.3) can be further simplified to a diffusion equation in radial coordinates:

$$\frac{\partial c_s}{\partial t} = \frac{1}{r^2}\frac{\partial}{\partial r}\left(D_s r^2 \frac{\partial c_s}{\partial r}\right) \tag{2.4}$$

where r is the radius of the solid particles. Note that in this treatment, there is no distinction between different types of solids. Any solid material property such as the solid diffusion coefficient, D_s, has a bulk value that is representative of the conglomerate of various solids. In this case, D_s is approximated as a constant, and therefore, Equation (2.3) is a linear partial differential equation. Instead of adding a second dimension to solve for the diffusion in the solid phase, the flux at the solid surface can be approximated by Duhamel's superposition integral [91, 52] to simplify computation.

The potential in the electrolyte is given by a modified Ohm's Law:

$$\nabla \phi_2 = -\frac{\boldsymbol{i_2}}{\kappa} + \frac{2RT}{F}\left(1 - t^o_+\right)\left(1 - \frac{d\mathrm{ln}f_\pm}{d\mathrm{ln}c}\right)\nabla \mathrm{ln}c \tag{2.5}$$

given that the potential is a relative value rather than an absolute one, $\mathit{\Phi}_2$ is set to zero at the positive electrode-current collector interface as a boundary condition.

For galvanostatic discharge or charge of the electrochemical cell, the total current in the cell is constant and specified as a boundary condition. Therefore, the potential in the solid phase is given by the Ohm's Law of the following form:

$$\boldsymbol{I} - \boldsymbol{i}_2 = \boldsymbol{i}_1 = -\sigma \nabla \phi_1 \tag{2.6}$$

where $\boldsymbol{I}$ is the sum of current densities in both the solid and electrolyte phases in the electrode. This value should equal to the liquid phase current density in the separator as well. The cell voltage is given by the solid phase potential difference between the two ends of the cell.

Finally the system is closed by accounting for the reaction rates at the solid-liquid interface via the Butler–Volmer equation:

$$i_n = i_o \left[\exp\left(\frac{\alpha_a F \left(\phi_1 - \phi_2 - U\right)}{RT} \right) - \exp\left(-\frac{\alpha_c F \left(\phi_1 - \phi_2 - U\right)}{RT} \right) \right] \tag{2.7}$$

which relates the local electrochemical reaction rate (i_n), or the net pore-wall flux due to reaction at the solid surface, to the local concentration and potential. By electroneutrality, the current balance requires the flux term to be equal to the divergence of the current in the electrolyte [88]:

$$\nabla \cdot \boldsymbol{i}_2 = a i_n \tag{2.8}$$

where a is the interfacial surface area. The governing equations (2.2)–(2.8) are implemented by Newman and his collaborators in a Fortran-based code called `dualfoil` [52, 87], which is modified for the work done in this thesis. The equations are solved on a one-dimensional grid traversing from the negative to positive current collectors for the state variables c, c_s, i_2, i_n, Φ_2 and Φ_1.

2.2.2 Numerical Treatment of the Cell Model

The model presented in Section 2.2.1 simulates the transient discharge process in an electrochemical cell. Some numerical treatment is required to ensure the smoothness and continuity of the cell output with respect to the design parameters to ensure accurate derivative output for the optimizers. Most notably, the discharge termination condition results in the see-saw pattern of energy density function with respect to design variables such as cycling rates (Figure 2.2).

The termination criterion for the galvnostatic discharge is determined by the cell voltage—a state variable—reaching the cutoff value. Given that it is difficult to determine the cell voltage a priori, the termination condition is instead given as the last time step that results in the cell voltage decreasing to below the cutoff voltage. This results in a final cell voltage in the original function that does not precisely match the cutoff voltage. Furthermore, the final cell voltage does not vary continuously with respect to the design variables, resulting in the see-saw pattern of the energy density function. While simulation with such termination condition is sufficient for estimating the cell performance, it is inadequate for gradient-based optimization, which assumed continuous smooth functions. The random termination condition results in erroneous derivatives with respect to the design variables. The inexactness of the cell voltage at termination also causes other numerical discontinuities in cell properties that depend on cell voltage values.

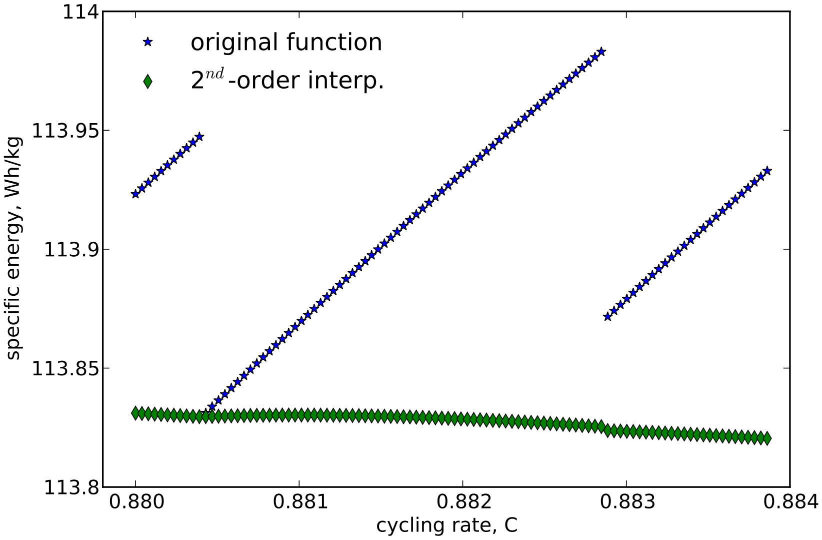

Figure 2.2: Original energy density function is see-saw shaped. The over-estimate of energy density increases as the final cell voltage decreases and is only reset when the number of time step is reduced. The error can be reduced using Lagrangian interpolation

Figure 2.2 shows how the energy density of the original cell model varies with the discharge cycling rate. As the cycling rate increases, the useful energy density extracted from the cell should decrease. However, this is not the case from the original objective function. As the cycling rate increases from 0.88 C to 0.884 C in Figure 2.2, the time step termination condition results in the final cell voltage being increasingly less than the cutoff voltage. This in turn causes an overestimate of the energy density due to the additional discharge below the cutoff voltage. The error is only corrected when the number of time step is reduced upon further increase in cycling rate, e.g., when the cycling rate is further increased to beyond 0.884 C. The reduction in time step causes the final cell voltage to reset to the cutoff voltage, and hence the loss of the final time step reduces the cell energy density. This issue is addressed by using dynamic step sizing and higher order interpolation. Dynamic step sizing reduces the final time step sizes as the cell voltage approaches the cutoff voltage, so as to reduce the cell voltage over-estimate. Lagrangian interpolation [92] is also applied to approximate the objective function such that it gives an accurate estimate of the cell property at the exact discharge termination condition. To ensure continuity of the derivatives, second order Lagrangian interpolation was used.

2.2.3 Equivalent-Circuit Model

A detailed model is useful to understand how design parameters affect the performance of the cell. However, it is too computationally intensive to perform control optimization, or to estimate battery performance and state of health in real-time. A simplified model is required that can offer a relative high degree of accuracy in terms of cell discharge characteristics with a reasonable computational cost. An equivalent circuit model represents the various characteristics of a battery using simplified circuit components. When accurate experimental data on cell characteristics are available, it can offer an accurate prediction of cell behavior.

There are various types of equivalent circuit representations for a battery cell [93]. Figure 2.3 shows a Thevenin model that takes into account all major factors contributing the potential drop of the cell voltage. It consists of a parallel RC circuit connected in series to a resistor. The resistor R_1 represents the internal resistance in the cell, R_2 represents the polarization resistance, and the capacitor C_1 describes the transient response due to mass transfer kinetics.

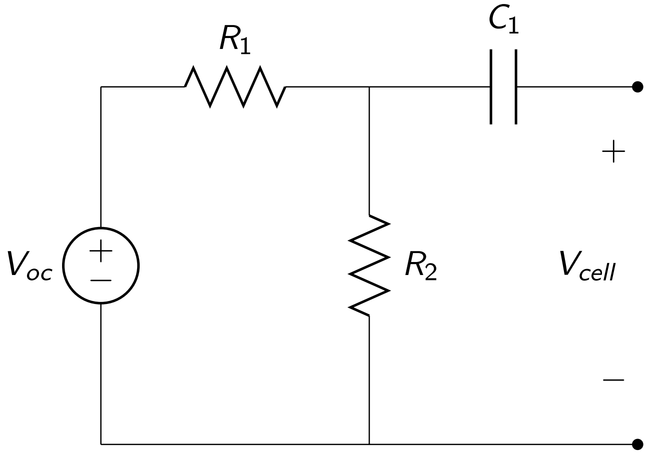

Figure 2.3: Thevenin equivalent circuit representation of a battery cell

The equivalent circuit model can be further simplified such that a single resistance term is used to describe the total Ohmic drop in the cell. The behavior of the cell can be represented by the following equation:

$$\begin{aligned} V_{cell} &= V_{oc} - IR_{int} \\ P_{cell} &= V_{oc}I - R_{int}I^2 \end{aligned} \tag{2.9}$$

The resistance term R_{int} and the OCV can be both functions of SOC to reflect how the internal impedance of the cell varies as the battery discharges. The current can be calculated by solving a quadratic equation in terms of the power output of the cell.

2.3 Vehicle Model

A simplified vehicle model is used to compute the battery power and energy needed to follow various driving cycles. The power required to propel the vehicle is defined to be:

$$P_{veh} = P_{climb} + P_{acc} + P_{drag} + P_{roll} + P_{mis} \tag{2.10}$$

where the total power required is the sum of the power required to overcome aerodynamic forces (P_{drag}), rolling resistance(P_{roll}), power miscellaneous systems (P_{mis}), and to achieve the required acceleration (P_{acc}) and rate of climb (P_{climb}) of the driving cycle. The miscellaneous power refers to the power required for various auxiliary systems not related to drivetrain. The total power required can be expressed in terms of vehicle parameters:

$$P_{veh} = MV\left(g\sin\theta + \frac{dV}{dt}\right) + \frac{1}{2}\rho_{air}C_{d,aero}AV^3 + C_{d,roll}MgV + P_{mis} \tag{2.11}$$

where M is the combined mass of vehicle plus passengers, V is the instantaneous vehicle velocity, A the frontal area of the vehicle, $C_{d,aero}$ and $C_{d,roll}$ are the aerodynamic drag and rolling resistance coefficients, respectively.

2.4 Optimization Technique

Numerical optimization is the selection of the design variables that best satisfies certain criteria. It differs from traditional engineering analysis by addressing the question of “is this the best possible” instead of “is this good enough”. The advantage of optimization process lies in the ability to quickly generate multiple alternative designs and to rigoriously analyze them using a set of prioritized criteria. The optimization process is iterative, repeatedly sampling the design space to locate the optimal design point, as shown in Figure 2.4. The convergence conditions can be either the local derivatives in the form of the Karush–Kuhn–Tucker (KKT) conditions [94], or the improvement in objective functions over successive iterations, depending on the type of optimizers.

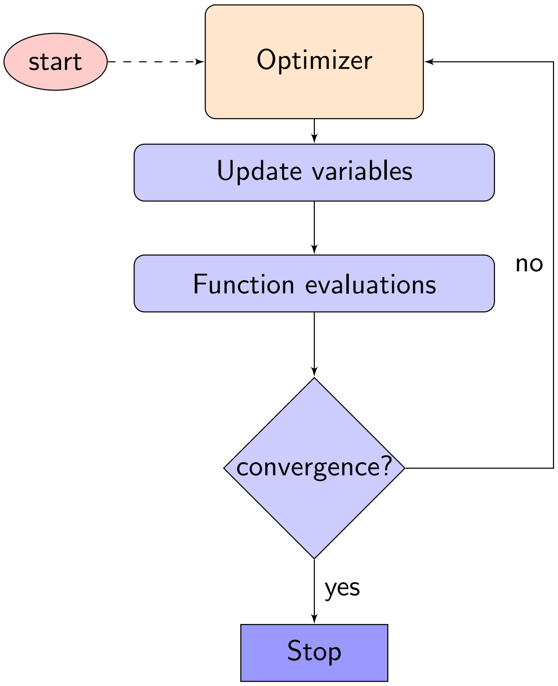

Figure 2.4: Optimization process

A general nonlinear optimization problem can be written as:

$$\begin{aligned} &\text{minimize} \quad f(\boldsymbol{x}), \qquad\qquad f:\mathbb{R}^n \to \mathbb{R} \\ &\text{subject to} \quad \begin{cases} \boldsymbol{x}_{min} \leq \boldsymbol{x} \leq \boldsymbol{x}_{max} \\ c_j(\boldsymbol{x}) = 0 \quad j = 1, ..., m \\ \hat{c}_k(\boldsymbol{x}) \leq 0, \quad k = 1, ..., \hat{m} \end{cases} \end{aligned} \tag{2.12}$$

where $f(\boldsymbol{x})$ is the objective function to be optimized with respect to the bounded variables $\boldsymbol{x}$, subject to equality constraints $c(\boldsymbol{x})$ and inequality constraints $\hat{c}(\boldsymbol{x})$. Both gradient-free and gradient-based optimizers can be employed to solve the battery pack optimization problem. The previous section described the cell models used to compute the objective function and the relevant constraints. This section will explain the optimizers and how they determine the search directions and convergence criteria in the process.

2.4.1 Gradient-Free Optimizers

Gradient-free optimizers, as the name suggests, depend only on function evaluations to locate the optimal solutions, and these class of optimizers are used to solve the battery pack optimization problem described in Chapter 4. The battery pack design problem is a nonlinear mixed-integer problem with nonlinear constraints. The optimizer has to traverse a discontinuous constrained design space and handle nonlinear problems efficiently. For this reason gradient-free optimizer, which is effective in solving noisy, non-differentiable and multi-modal problems, is selected for optimization problems with discontinuity in the design space. There are many different types of gradient-free optimizers available, and performance comparisons have been made of these optimizers on noisy optimization problems [95, 96]. For this work we use the ALPSO method implemented within the pyOpt framework [97, 98]. The ALPSO algorithm is a stochastic population-based method that employs a group of candidate solutions—known as particles—to search for the optimum [97]. These particles move about in the design space by updating their positions and velocities according to the following equations:

$$\begin{aligned}\boldsymbol{x}^i_{k+1} &= \boldsymbol{x}^i_k + \boldsymbol{V}^i_{k+1}\Delta t \\ \boldsymbol{V}^i_{k+1} &= w_0\boldsymbol{V}^i_k + w_1 r_1\left(\boldsymbol{p}^i_k - \boldsymbol{x}^i_k\right) + w_2 r_2\left(\boldsymbol{p}^g_k - \boldsymbol{x}^i_k\right)\end{aligned} \tag{2.13}$$

where $\boldsymbol{x}^i_k$ is the position of the *i*th particle at iteration *k*, $\boldsymbol{V}^i_k$ is its velocity vector, Δt is the time step size, $\boldsymbol{p}^i_k$ is the position with the best objective function for particle *i* (particle best), and $\boldsymbol{p}^g_k$ is the global position with the best objective function for all the particles up to the *k*th iteration (global best). The movement of the particles are hence governed by their own movement history as well as the collective influence of the entire swarm. The weights, w_0, w_1, and w_2 are assigned to each component of the velocity update. They are bound by the following relations to ensure stability and to guarantee convergence [97]:

$$\begin{aligned}&0 < w_1 + w_2 < 4 \\ &\tfrac{w_1+w_2}{2} - 1 < w_0 < 1\end{aligned} \tag{2.14}$$

The constraints are included by introducing explicit Lagrangian multiplier estimates for each constraint into the objective function. This approach transforms the constrained problem into an unconstrained one, while preserving the feasibility of the solution by including the KKT conditions in the optimization problem formulation. The Lagrange function is further augmented with a quadratic function to preserve the stationary properties of the solution, making the final function of the form [99, 100]:

$$\mathcal{J}_i(\mathbf{x}_k^i, \lambda, r_p) = f(\mathbf{x}_k^i) + \sum_{j=1}^{m} \lambda_j \theta_j(\mathbf{x}_k^i) + \sum_{j=1}^{m} r_{p,j} \theta_j^2(\mathbf{x}_k^i) \tag{2.15}$$

where $f(\mathbf{x}_k^i)$ is the objective function of the ith particle at kth iteration, λ_j and θ_j are the Lagrange multiplier and quadratic function extension for the jth constraint respectively, and r_p is the quadratic penalty factor.

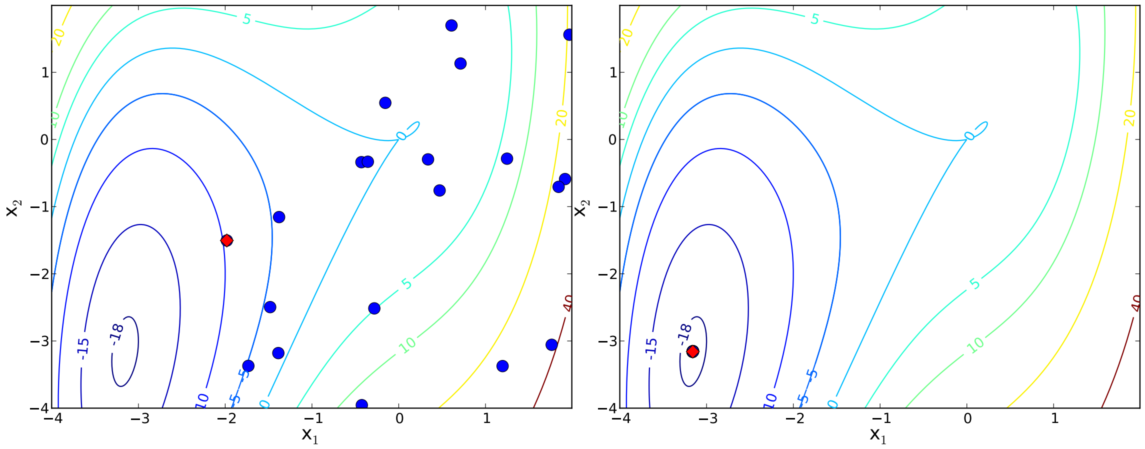

Figure 2.5: Solution history using ALPSO to solve a 2D problem. Left: initial distribution of particles. Right: converged optimization where all particles are at the global optimum

Figure 2.5 shows the iteration process of ALPSO applied to a simple 2-variable optimization problem. The optimization is initiated by distributing 20 particles randomly in the design space. At each iteration, the objective function values at all the particle positions are evaluated, and the position of the particle with the best objective function value (marked by the red diamond in Figure 2.5) is broadcast to every other particle. This provides a spatial step in the optimization, represented by the last term on the right-hand side of Equation (2.13). At the same time, each particle keeps track of its own best position throughout its iteration history. This ensures that past iteration information is not lost, and it is represented by the second term on the right-hand side in Equation (2.13). Lastly, a random component is added to each particle's velocity to prevent premature convergence to a local minimum. However, given the stochastic nature of this optimization algorithm and lack of enforcement of mathematical optimality conditions, it is essential that multiple optimization runs are conducted to fully explore the design space.

Gradient-free optimizers are apt at solving non-smooth optimization problems and can handle discrete variables relatively easily. However, there is less confidence in the final solution because of the absence of mathematical optimality conditions. The optimization process with gradient-free optimizers is computationally expensive, requiring a large number of function evaluations. This is problematic if the objective function evaluation is costly, or if there is a large number of variables. Therefore, gradient-free optimization algorithms are only suitable for problems with small number of design variables, which is the case of the optimization problem solved in Chapter 4.

2.4.2 Gradient-Based Optimizers

The performance and properties of a single electrochemical cell is determined by morphological parameters, such as the electrode porosity and thickness, as well as transport parameters, such as diffusivity and conductivity. The output of the cell should physically vary smoothly with these continuous variables, though the effects can be nonlinear. In this case, gradient-based optimization methods are preferable, as they are more efficient for solving nonlinear optimization problems that have a continuous and smooth design space that is convex near the optima. Gradient-based optimizers make use of both function evaluations and local derivatives to search for the optimal solutions in the design space.

There are various types of gradient-based optimizers available. One of the most efficient ways to solve nonlinear constrained optimization problems is by approximating the nonlinear problem as a quadratic subproblem at each iteration, also known as the sequential quadratic programming (SQP) method. SQP is an active-set method that assumes the design space near the optimum to be convex. It uses the optimal solution for each quadratic subproblem to define a new iterate point. This method can be viewed as the application of Newton's method to the KKT optimality conditions. An effective SQP algorithm has to be able to compute a step from the quadratic subproblem and to generate an estimate of the optimal active set. From the many different SQP implementations available, we use the SNOPT package [101], which is a line-search SQP implementation.

SQP solves the following subproblem:

$$\begin{aligned} \text{minimize} \quad & f_k + \nabla f_k^T p + \tfrac{1}{2} p^T \nabla_{xx}^2 \mathcal{L}_k p \\ \text{subject to} \quad & \nabla c_i(x_k)^T p + c_i(x_k) = 0 \\ & \nabla \hat{c}_i(x_k)^T p + \hat{c}_i(x_k) \leq 0 \end{aligned} \tag{2.16}$$

where p is the step size from the current iteration point that minimizes the quadratic subproblem, $\nabla \mathrm{f_k}$ is the gradient of the objective function with respect to the design variables, and $\nabla_{xx}^2 \mathcal{L}_k$ is the estimate of the second-order derivatives of the Lagrangian function. The second-order derivative can be estimated by using a quasi-Newton approximation, such

Broyden–Fletcher–Goldfarb–Shanno (BFGS) [94]. The matrices $\nabla c_i(x_k)$ and $\nabla \hat{c}_i(x_k)$ are the Jacobian of the equality and inequality constraints with respect to the design variables. At each iteration, the solution to the quadratic subproblem is obtained using a quasi-Newton approach.

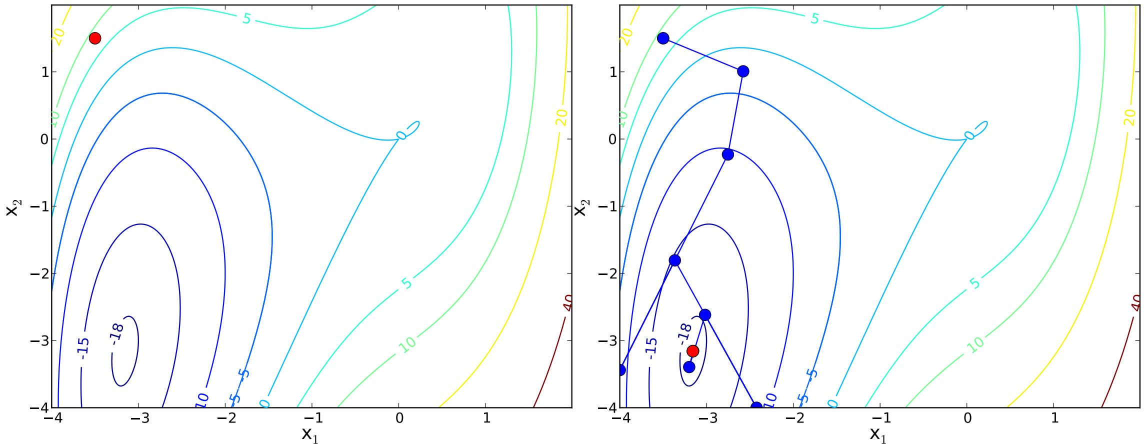

Figure 2.6: Solution history using SNOPT package with finite-difference derivative approximation on a 2D problem. Left: initial starting location of the optimization. Right: final iteration with the iteration history shown

Figure 2.6 shows the SQP applied to the same 2-variable problem as shown in Figure 2.5. Unlike ALPSO, SQP only requires one initial point. At each iteration, the optimizer evaluates both the objective function and the local derivatives to determine the search direction and step size that solves Equation (2.13). As shown in the figure, the optimizer converges quickly to the optimum solution in less than ten iterations. The iteration history shown in Figure 2.6 indicates that the optimizer has over-predicted the intermediate solution on two occasions, resulting in the intermediate solution being at the bounds. Given that this sample problem only has two variables, the quadratic approximation used in SQP should provide an exact approximation of the design space. The solution overshoot is most likely due to errors in the derivatives supplied by the finite-difference approximation. However, in each case, the optimizer is able to backtrack its steps and successfully determine a new search direction.

One of the issues with gradient-based optimization is the possibility of converging to local optima instead of the global one. Given that one of the convergence criteria is the local derivatives defined by the KKT conditions, it is foreseeable that the optimizer converges to a local optimal solution when the problem is multi-modal. Figure 2.6 shows that there exists a local minimum at $(x_1, x_2) = (0, 0)$. An optimization initiated on the top right

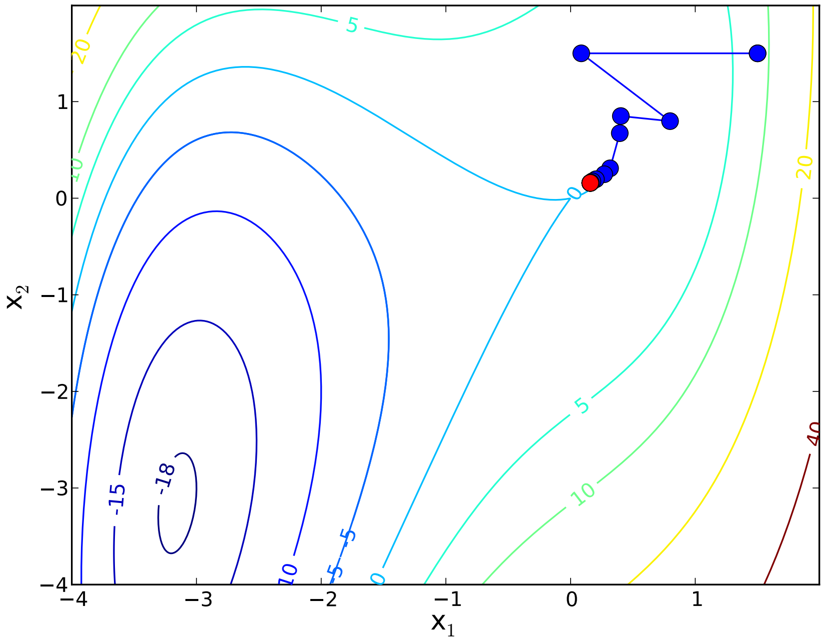

Figure 2.7: An optimization that is initiated from $(x_1, x_2) = (1.5, 1.5)$ converges to the local optimum at and fails to find the global optimum

corner of the design space can converge to the local minimum and fails to find the global minimum on the bottom right corner, as shown in Figure 2.7. One way to increase the chance of finding the global optimum is to initiate multiple optimization runs at random locations.

2.4.3 Derivative Computation

One of the keys to taking full advantage of gradient-based optimization is to use efficient and accurate method for computing derivatives derivatives. A range of derivative computation methods are available, depending on the nature of the optimization problem, the complexity of the derivative computation, and the number of design variables [102]. Given that the battery pack design problem has a relatively small number of variables, the complex-step approximation method [103] is used to obtain the derivatives due to its accuracy and the ease of implementation. The complex-step method is similar to the more common finite-difference approach, except that a small step is taken in the imaginary axis instead of the real axis. Taking the Taylor series expansion about a point in the real axis with a purely complex step:

$$f(x + i\Delta x) = f(x) + i\Delta x \frac{\mathrm{d}f}{\mathrm{d}x} - \frac{\Delta x^2}{2}\frac{\mathrm{d}^2 f}{\mathrm{d}x^2} + \frac{i\Delta x^3}{3!}\frac{\mathrm{d}^3 f}{\mathrm{d}x^3} + \cdots \tag{2.17}$$

A second-order approximation of the first-order derivative can be isolated from Equation (2.17):

$$\frac{\mathrm{d}f}{\mathrm{d}x} = \frac{\operatorname{Im}\left[f\left(x + i\Delta x\right)\right]}{\Delta x} + \mathcal{O}\left(\Delta x^2\right) \tag{2.18}$$

Equation (2.18) shows that the complex step derivative does not involve a subtraction operation, and hence it is not subject to cancellation errors resulting from finite-precision arithmetic, which is a problem with finite-difference derivative approaches. A step size study is often needed for finite-difference approximations to determine the step size that minimizes the cumulative effects of both approximation and cancellation error. However, this is not a problem with the complex-step method, as its step size can be made arbitrarily small. A comparison of the derivatives computed using the complex-step method and a forward-difference approach is shown in Figure 2.8. The normalized errors of the two approaches are plotted against the step size. Figure 2.8 shows how the cancellation error due to loss of significant digits dominates at small step size for the forward difference approach, whereas the error of the complex-step approximation remains at machine-zero (10^{-16} for double-precision arithmetic). The lack of cancellation error means that the complex-step method does not require a step-size study to determine the optimal step size to minimize the total error, and hence expedites the optimization process and saves computational time.

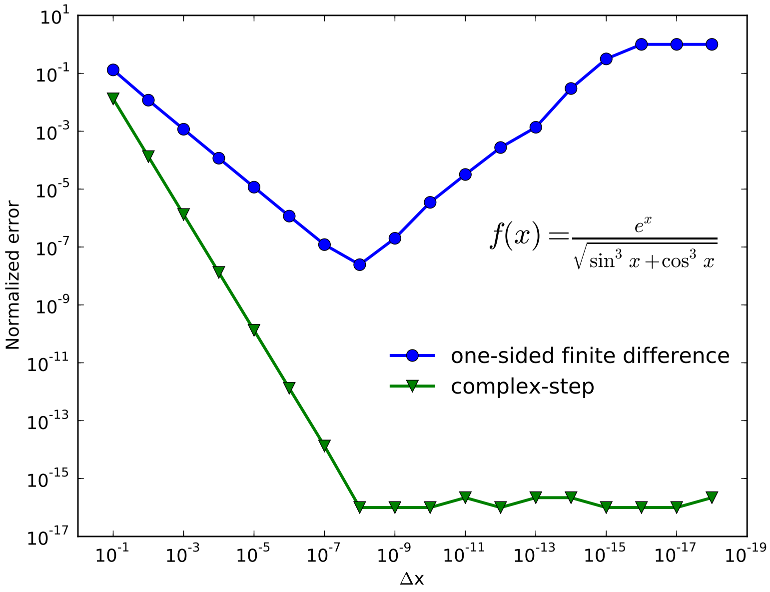

Figure 2.8: Error in the derivatives computed using finite-difference and complex-step approximations for varying step sizes. The complex-step approach is free of cancellation errors that dominates finite-differences at small step sizes.

The difference between the derivatives calculated using finite differences and the complex step applied to the physics-based electrochemical model is shown in Figure 2.9. Note that derivatives obtained from both the finite-difference and complex-step methods follow the same trend, but there is much more scattering in the derivatives obtained using the finite-difference method.

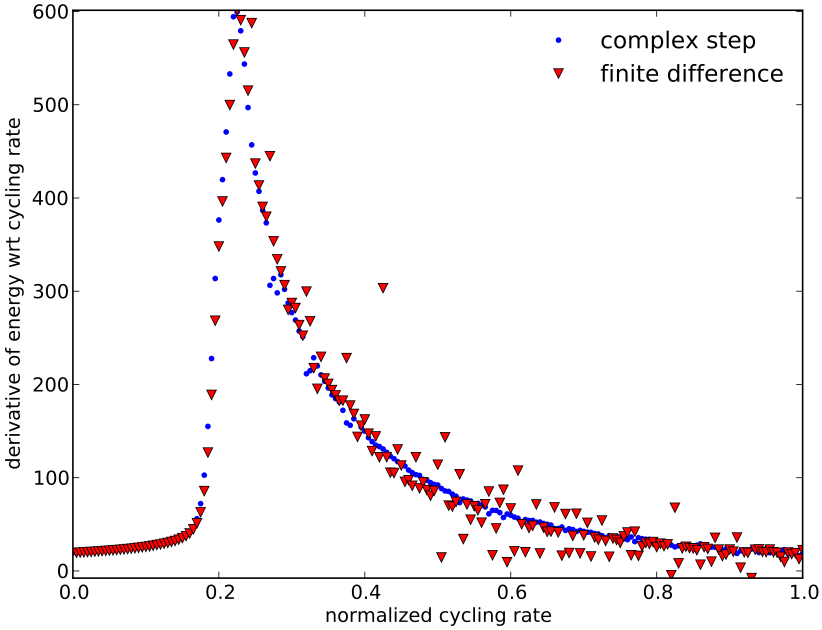

Figure 2.9: Derivatives of energy density with respect to cycling rate obtained using the finite-difference method show much more scattering compared to the complex-step approximation.

While the complex-step approximation offers the advantage of increased accuracy, it only works in cases where the design variable or objective function of interest are not already complex in the original function. The application of the complex-step to computational models requires the modification to the original source code, which can be non-trivial in certain instances. The increased accuracy in the function evaluation also comes with additional computational cost: changing all real variable operations to complex variable operations increases the computational time by 3 to 4 times. The increased accuracy of the derivatives computed by the complex-step approximation method as shown in Figures 2.8 and 2.9, however, make up for the additional computational cost in ensuring the optimizers locate the true optimal solutions.

2.4.4 Pareto Optimality

The optimization of a single objective function with respect to the design variables is straight-forward as it will be the solution of the optimization problem. It is often the case, however, that there are multiple competing objectives of interest. For instance, one may want to maximize the energy density of a battery cell while at the same time maximize the power output. Alternatively, one may want to minimize the mass, volume and cost of a battery pack. Given that the decision maker may not be the person performing the optimization, it is often difficult to determine a priori the compromise between the various objectives for the desired solution. Such multi-criteria decision making scenarios require a Pareto front, or Pareto optimal points to examine the relations and trade-offs between multiple objectives. By definition, a point is Pareto optimal if and only if none of the objectives can be improved without penalizing at least one of the others [104]. A Pareto front therefore contains solutions that are not dominated by any other points in the design space, i.e., the solutions on the Pareto front have the best objective functions at their respective constraints [105, 106]. This front offers valuable insight into multi-objective optimization in numerous engineering applications [105, 107], and it is used to examine the relation between energy and power of optimal cell designs in Chapters 3 and 5.

2.4.5 Hybrid Optimization Method

The advantages and the disadvantages of gradient-free and gradient-based optimizers were illustrated in Sections 2.4.1 and 2.4.2. While the different groups of optimizers work well on separate classes of problems, it is possible to employ a hybrid optimization scheme that combines the two types of optimizers, as shown in Figure 2.10 in the form of an XDSM diagram. The hybrid process is governed by the optimization control, which uses the rudimentary optimal results from the gradient-free optimization as the starting point of the gradient-based optimization. The main reason to use the hybrid approach is to take advantage of the different niches of the two classes of optimizers to facilitate an efficient optimization process. The gradient-free optimizer minimizes the chance of getting trapped in a local minimum in the nonlinear design space, and the gradient-based optimizer pinpoints the exactly location of the optimum with respect to the continuous variables. The hybrid optimization process is used to solve the battery pack design problem discussed in Chapter 4. While the design at the cell level involves continuous variables, the battery layout (number of cells in series and parallel) at the pack level requires integer values, thus making the battery pack design a mixed-integer optimization problem. For the pack design problem, the hybrid optimization scheme can take advantage of the independence between the cell design and the pack design.

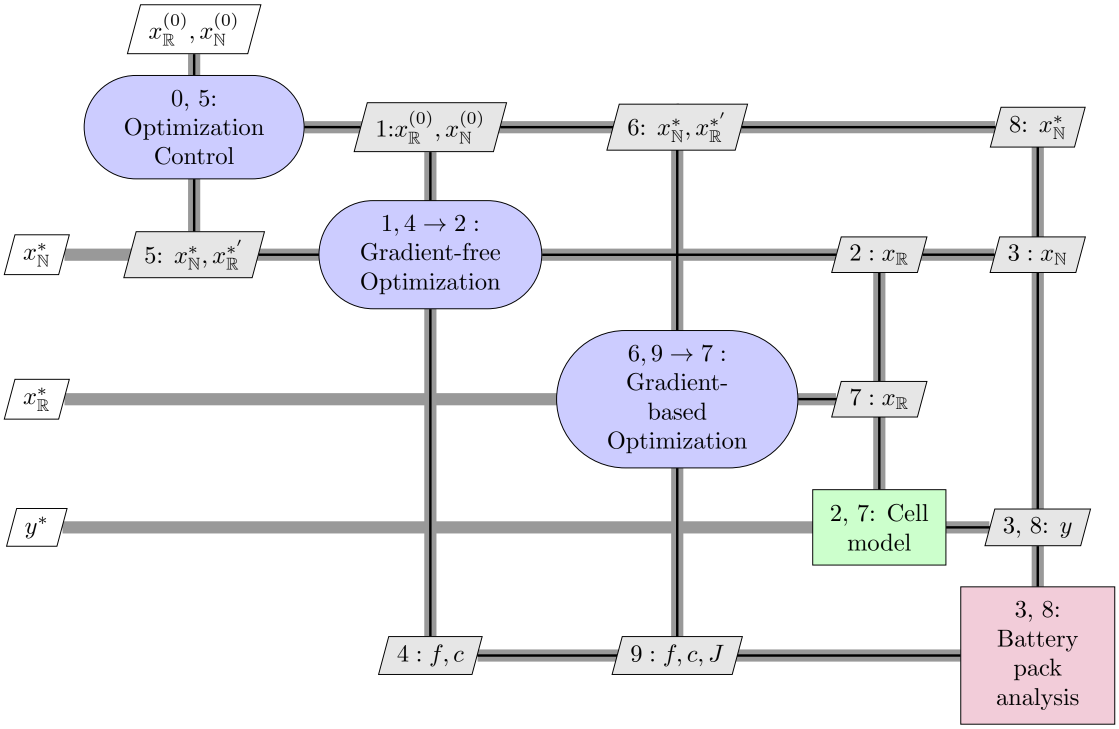

Figure 2.10: The XDSM for the hybrid optimization process [3]. The numbers represent the steps in the optimization process. The optimization control (Step 0) first initiates the gradient-free optimization (Loop 1–4), which provides a rudimentary optimal solution and determines the optimal integer design variables. The results from the gradient-free optimizion is then used to initialize the gradient-based optimization (Step 5). The gradient-based optimizater (Loop 6–9) refines the continuous design variables for the final optimal solution.

CHAPTER 3

Single-Cell Design Optimization

3.1 Introduction

An important aspect in lithium-ion cell design is to maximize the energy density to meet the demand of mass or volume sensitive applications. Conventional cell designs have relied on ad-hoc rules—such as using thicker electrodes for high energy density—or parametric analysis of one or two variables to guide the design process. Both experimental analyses and numerical simulations have been applied to examine how various properties of an electrochemical cell affect its performance. Choi et al. [108] investigated the particle size effects on performance of a $LiCoO_2$. Li et al. [109] studied carbon black and carbon nanotubes as conductive additives, and how they improve energy capacity and cycling stability. Doyle et al. [110] used numerical simulation to study the trade-off between conductivity and transference number for lithium-polymer batteries. While these efforts increased the understanding of how individual components affect cell performance, they are unable to fully maximize the cell performance, since the coupled interactions of the various parameters were not been considered. To identify optimal cell designs, the design process has to include all relevant design variables, and the coupling between various parameters during cycling needs to be considered.

Several authors have carried out numerical optimizations of lithium-ion cells. Newman [111] optimized the geometric design of a cell with respect to the positive electrode thickness and porosity using a simplified reaction zone model. By confining the lithium-ion intercalation to a narrow zone in the positive electrode, he obtained an analytical solution and related the dependence of energy capacity to the following dimensionless parameter:

$$T_{rz} = \frac{U\kappa t_{dis}}{q_+ L_s^2} \tag{3.1}$$

where U is the open-circuit potential, κ the electrolyte conductivity, t_{dis} the discharge time,

q_+ the capacity density of the active material, and L_s the separator thickness. Values for optimal electrode thickness and porosity were found by fixing the discharge time t_{dis}. Subsequent optimization efforts involved design of an iron phosphate lithium-ion cell while maintaining constant capacity ratio and porosity in the negative electrode [112], as well as coupling lithium-ion batteries with capacitors for hybrid electric vehicle operation [113]. In an optimization study with respect to cycling rate, particle size, diffusivity and conductivity using a surrogate model formulation, Du et al. [114] quantified the cell performance as a function of ratio of discharge time to diffusion time. Ramadesigan et al. [115] found that optimizing the spatial distribution of porosity can lower the internal resistance by 15–33% compared to a uniform distribution. Golmon et al. [116] went one step further and varied both the spatial porosity and the particle size distribution using a multi-scale model. They found that when both porosity and particle size distribution are varied, the improvement in energy capacity is less than 2% compared to a cell with optimized constant porosity and particle size. More recently De et al. [117] used the control vector parameterization method to sequentially optimize the electrode thicknesses and porosities with a reformulated model for improved computational efficiency.

The application of numerical optimization to battery design is still in its nascent stage. The high computational cost of a physics-based model and the lack of a complete mathematical description of the processes occurring in a battery system have hindered the implementation of optimization schemes in battery design. One way to reduce the computational cost of battery optimization is to speed up the cell model simulations. Specifically, approximations have been derived to accelerate the solid phase diffusion computation [118, 119, 55]. Additional improvements in computational efficiency are achieved by improving the model calculation in the direction normal to the electrode/separator interface [120, 121]. Reduction in computational cost can be realized by minimizing the number of function evaluations as well. Surrogate model analyses proposed by Du et al. [114, 122] reduces the design space by removing design variables that do not affect objective function. An efficient optimizer that requires relatively few function evaluations to converge to the optimum can be used as well. Various optimization methods can be used to tackle the battery optimization problem [98, 114, 123, 124, 125, 126]. Given the nonlinear nature of the battery problem and the computational cost (each function evaluation is on the order of minutes), a gradient-based optimization scheme, which makes use of derivatives to determine the search directions, is well suited to handle such a problem due to its numerical efficiency and accuracy [124].

In optimizing the battery design, both morphology and material transport properties need to be considered as variables in the design process. The design space should include all relevant parameters of a full lithium-ion sandwich cell with insertion compounds for both electrodes. With this goal in mind, a numerical framework that couples an optimization algorithm with a detailed electrochemistry model to optimize the cell design is presented here. The objectives are as follows:

1. Maximize the energy density of a lithium-ion cell subject to a power requirement.
2. Determine electrode morphological designs at optimal cell designs under various discharge rates.
3. Quantify the relative sensitivity of the design variables on cell performance.

3.2 Problem Formulation

A numerical optimization framework coupling the SQP method (Section 2.4.2) with the macroscopic cell model (Section 2.2.1) is used to maximize the gravimetric energy density of an ideal lithium-ion cell subject to power requirement. The materials of the cell and their respective properties are listed in Table 3.1. The cell used in this problem consists of a lithium-ion cell with spinel manganese oxide $LiMn_2O_4$ for the cathode and mesocarbon microbead (MCMB) graphite for the anode. Manganese oxide is used as the cathode material, since it is relatively inexpensive, easily disposable, and exhibits good capacity retention rate. Carbon is used as the anode active material as it experiences small volume change, which is essential in capacity retention. The validation of lithium-ion cell with spinel manganese cathode and graphite anode using the cell model outlined in Section 2.2.1 is provided by Doyle et al [127].

The cell performance is obtained through galvanostatic discharge of the cell until a cutoff voltage of 3.0 V is reached. This cutoff value is selected as further discharge of in a real cell could lead to irreversible damage to the battery. The energy density of the cell is calculated using the trapezoidal approximation to the integral over discharge time:

$$E_{cell} = \frac{1}{M_{cell}} \int_0^{t_{cut}} V_{cell}(t) I dt \approx I \sum_{k=0}^{n} \frac{V_{k+1} + V_k}{2} \left(t_{k+1} - t_k\right) \tag{3.2}$$

where *I* denotes the cell current, which is constant. *k* is the time step number and *n* is the number of time steps needed to reach the cutoff voltage. The cell mass, M_{cell}, in turn is given as follows:

$$M_{cell} = M_+ + M_{sep} + M_- + M_{misc} \tag{3.3}$$

Table 3.1: Lithium-ion cell material properties and fixed parameters [9]

Parameter	Value
Cathode material	Spinel Mn_2O_4
Cathode initial stoichiometric parameter (y in $Li_yMn_2O_4$)	0.2
Coulombic capacity of cathode material	148 mAh/g
Density of cathode material	4280 kg/m^3
Volume fraction of inert filler in cathode	0.1
Anode material	MCMB 2528 graphite
Anode initial stoichiometric parameter (x in Li_xC_6)	0.9
Coulombic capacity of anode	372 mAh/g
Density of anode material	2260 kg/m^3
Volume fraction of inert material in anode	0.05
Electrolyte material	$LiPF_6$ in EC:DMC
Initial salt concentration	1000 mol/m^3
Inert filler material	PVDF
Ambient temperature	298 K

where M_+ and M_- are the mass of the positive and negative electrode active materials respectively, M_{sep} is the mass of the electrolyte, and M_{misc} is the mass of all the other non-energy contributing materials such as current collectors. The mass of each component is a function of its thickness and porosities of various materials that make up its composition. Additional components, such as casings, are not considered; hence the energy densities obtained will be that for a jelly roll.

To maximize the energy density, the 12 design variables listed in Table 3.2 are selected. While cycling rate is an operating condition and not a cell design variable, it is necessary to allow it to vary freely within the design space in order to meet the power requirement. The simulation technique and the subsequent optimizations are not confined to any particular operating condition. Allowing cycling rate to vary freely enables us to obtain optimal cell designs to meet different application requirements. The remaining 11 design variables consist of 5 design variables for each of the electrodes, and the separator thickness. Among the 5 electrode variables, porosity, thickness, and to some extent, particle size, can be controlled during the manufacturing process, while the diffusivity and conductivity are material properties. However, there are substantial variations in the values reported in the literature for transport coefficients. These variations are due to experimental uncertainty, differences in electrode microstructure, manufacturing process, and experimental technique [9, 128, 129]. The bounds on the particle size, diffusivity and conductivity therefore represent the minimum and maximum reported values from published research. These

Table 3.2: Design variables and their bounds for single cell optimization

Design variable	**Lower bound**	**Upper bound**
Cycling rate (C)	0.1	10.0
Separator thickness (μm)	10.0	100.0
Cathode particle size (μm)	0.2	20.0
Cathode thickness (μm)	40.0	250.0
Cathode porosity	0.1	0.6
Cathode diffusivity (m^2/s)	10^{-16}	10^{-11}
Cathode conductivity (S/m)	1.0	100.0
Anode particle size ((μm)	0.5	50.0
Anode thickness (μm)	40.0	250.0
Anode porosity	0.1	0.6
Anode diffusivity (m^2/s)	10^{-16}	10^{-11}
Anode conductivity (S/m)	1.0	100.0

parameters are treated as bounded variables instead of given exact values as it is not the intent of this framework to optimize the design of a particular lithium-ion cell subject to a specific pre-fabrication treatment and manufacturing process. Rather, these variables are intended to provide guidelines on what combination of properties and cell designs would produce batteries of optimized performance, such as maximum achievable cell capacity.

To achieve optimality, the cell has to balance energy capacity with the ionic transport requirement, while at the same time minimize Ohmic losses. Among the 12 design variables, the cycling rate controls the current density, and hence galvanostatic boundary conditions. Low cycling rate is desired to maximize energy density, as it reduces Ohmic losses. Separator thickness controls the amount of electrolyte in the separator region. Out of the five electrode variables, thickness and porosity determine the amount of active materials available for lithium-ion intercalation process and the amount of electrolyte available for ionic transport. The electrode thicknesses and porosities, together with separator thickness, determine the mass of the cell and hence its energy density. Diffusivity and conductivity are transport parameters that affect the concentration overpotential in the cell, while the particle size affects the energy density by changing diffusion path length and interfacial surface area.

The range of the conductivities for both electrodes is high compared to the conductivities of the pure active materials in each electrode. These values reflect the increased electronic conductivity after the addition of carbon additives to the solid matrix. The cell model does not account for the effects of carbon additives on effective transport explicitly. However, using the high conductivity allows for theoretical cells that have performance more representative of what can be obtained in practice.

Nine different optimizations at each constrained power requirement were carried out. The optimizations are initiated from random design points to reduce the possibility of optimization converging to local optima. Due to the random nature of the initial points and the convergence tolerance of the optimization, there are some differences between the results in terms of number of iterations required and the optimal solutions. The results from the various optimization runs are collectively presented in the form of box plots. The box represents the interquartile range, with the line in the center representing the median. The whiskers extend from the boxes to show the full range of the data excluding the outliers, which are marked with the $+$ symbols.

3.3 Results

3.3.1 Power vs. Energy

In the absence of power requirement on the cell, the maximum energy density would achieved by using a very small discharge current such that there is minimal Ohmic drop in the cell. The cell voltage would be as close to the OCV as possible, and the resulting cell design would be one with maximum thickness, minimum porosity due to low ionic transport rate requirement. In this case, most (if not all) of the design variables listed in Table 3.2 would go to their respective bounds. Figure 3.1 shows a simple cell design problem where cycling rate and positive electrode particle size are the only two variables. Maximum energy density occurs in the lower left corner of the design space, resulting in the simple optimal solution where both the cycling rate and the positive electrode particle size are at their lower bounds.

A meaningful cell design problem, therefore, should consider how the cell designs are affected by the power requirements. Figure 3.2 shows the power density contours (in color) on top of the energy density contours (in gray) for the same 2-variable problem. As the power requirement increases, the design space that is able to satisfy the requirement becomes smaller. In this case the power density is mostly a function of the cycling rate. The graphical representation of the design space and objective function clearly shows that the cycling rate has to increase as the power increases while the cell design with maximum energy density has the smallest particle size regardless of the power requirement.

The optimization problem is expanded to the full design space of 12 design variables. The potential for using gradient-based optimization framework in cell design is demonstrated by maximizing its gravimetric energy density at various specific power require-

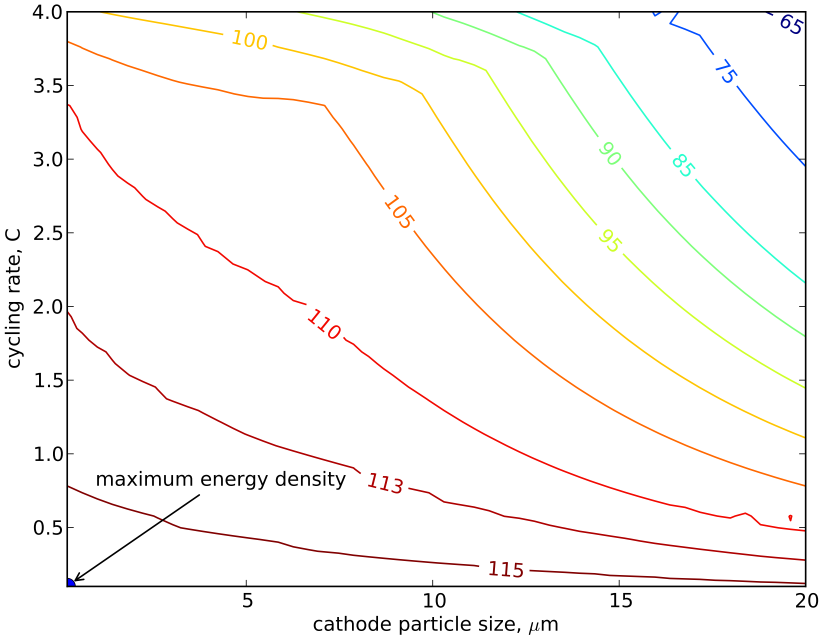

Figure 3.1: Contour plot of energy density shows monotonically decreasing energy density as cycling rate and particle size increases. Maximum energy density occurs at minimum cycling rate and particle size.

ments. The constrained power requirement increases from 50 W/kg/m^2 at increment of 50 W/kg/m^2 until 1500 W/kg/m^2 , at which point a further increase in power is only possible by expanding the upper bound of the cycling rate. The competing effects of increasing power and decreasing energy at higher power form a Pareto front. In this case the Pareto front is formed from the set of points with the maximum achievable cell energy capacity for each required power level.

Figure 3.3 shows the optimal energy density with respect to various power requirements. As expected, the maximum achievable energy density decreases as the power requirement increases. For all nine optimization runs at each specified power requirement, the final optimal energy densities converged to within 0.1% of one another. The Pareto front is contrasted with the Ragone plots. The Ragone plot compares the performance of the energy storage device at different power ratings by plotting its available energy density against power density [130]. While the Pareto front consists of cells optimized for each power requirement, the Ragone plot shows the variation of energy density versus power density for a specific cell. Four representative Ragone plots are shown in Figure 3.3. The 0.2-C cell corresponds to the power requirement of 50 W/kg/m^2, while the 2-C is at 400 W/kg/m^2, 4-C is at 800 W/kg/m^2, and the 9-C is at 1500 W/kg/m^2. Each Ragone plot intersects the optimal Pareto front at only one point, indicating that each cell design is optimized for only

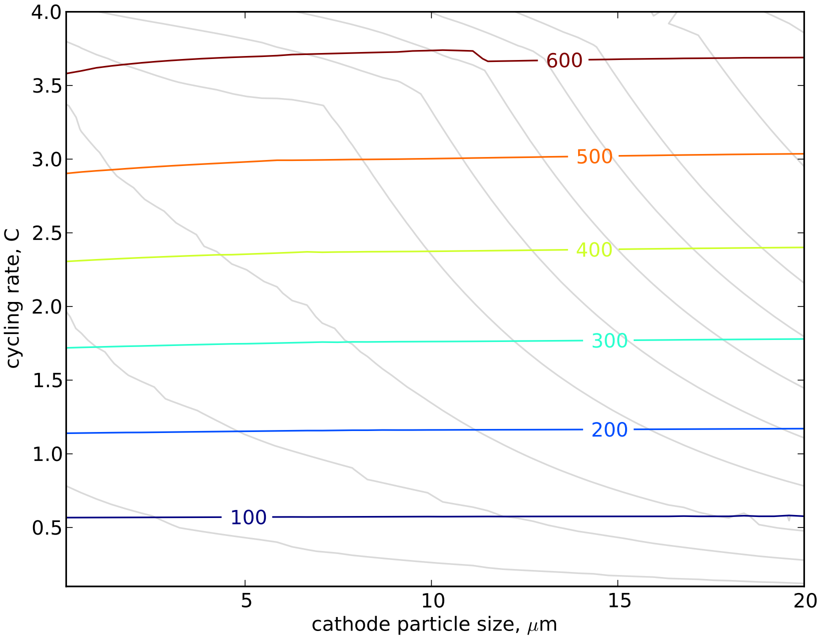

Figure 3.2: Contour plot of power density overlaid on top of energy density (light grey lines) shows how power requirements restrict the design space. The energy density increases when moving from the top right corner (high cycling rate, large particles) of the design space towards the bottom left (low cycling rate, small particles)

a specific power requirement and no single cell is the best design for all power requirements. The 0.2-C cell has the highest energy density at 50 W/kg/m^2. However, its energy capacity decreases rapidly if its discharge rate is increased. All four Ragone curves exhibit the typical knee, indicating the rapid deterioration of cell performance away from its specified design condition. Comparison between the Ragone plots and the optimal Pareto front demonstrates the importance of a properly designed cell for a specific operating condition. Any deviation of cell design away from its intended purpose will lead to rapid loss of energy capacity. Thereofore, it is important that the cell is properly designed using numerical algorithms so as to achieve maximum performance at its intended discharge rate.

Some representative energy and power density values from the literature [131, 132, 133] are also plotted in Figure 3.3 for comparison. The energy and power densities obtained from the optimization results are for an idealized lithium-ion battery jelly roll only, hence it is expected that their values are significantly higher than those achieved experimentally [131, 132]. Comparison of jelly-roll energy density with published simulation results [133] shows that the maximum achieved energy density shown here is about 4% higher.

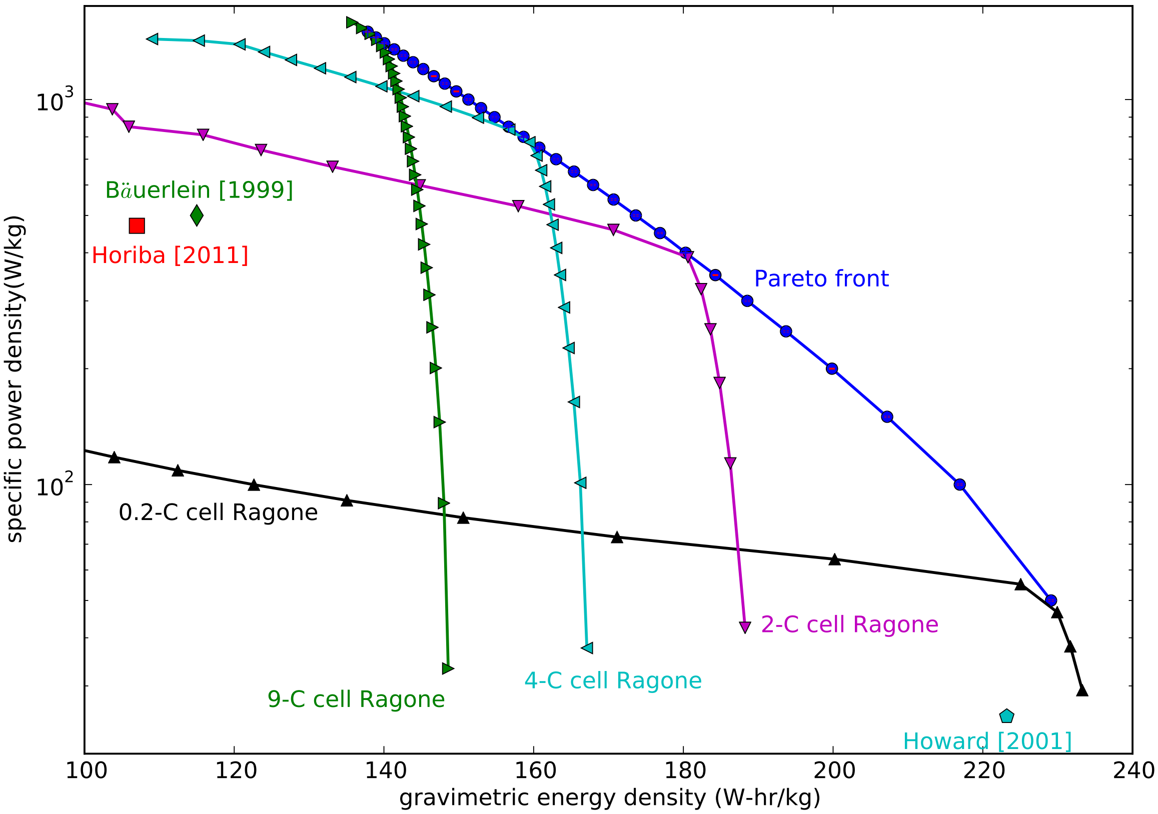

Figure 3.3: Pareto front of optimal energy density vs. specific power. Ragone plots at four discharge rates are also shown, which represent the variation of energy density with discharge rates for a particular cell.

3.3.2 Sensitivity at Optimal Designs

Next, the design variables of the optimal cell designs for various power requirements are quantified in terms of their numerical values and effects on optimal designs. Table 3.3 shows the sensitivities of energy density with respect to the variables at the optima. Note that since there is an optimal design point for each cell power requirement, it would be too cumbersome to show the sensitivity of each variable for all the optimum points. Therefore the average sensitivity across all optima is listed in Table 3.3 to give a qualitative comparison of the relative effects of variables on energy density. The sensitivity studies show that the morphological parameters such as cell thickness and particle sizes have much greater effect on energy density than transport parameters, such as diffusion and conduction coefficients. On average, the effects of transport parameters are an order of magnitude lower than those of other parameters. A more complete treatment of global sensitivity with respect to cathode variables is provided by Du et al. [122]. The relative effects of various design parameters will be elaborated on when discussing the transport parameters at optimal designs.

Table 3.3: Design variables and their sensitivities at optimal designs. Sensitivity is calculated as percentage change of objective function due to a percentage change in design variable.

Design variables	**Optimized design values**	**Average sensitivity (%)**
Cycling rate (C)	0.2–9.4	2.3
Separator thickness (μm)	10.0	0.25
Cathode particle size (μm)	0.2	0.34
Cathode thickness (μm)	133.4–250.0	0.34
Cathode porosity	0.13–0.54	0.30
Cathode diffusivity (m^2/s)	1.09×10^{-12}–10^{-11}	0.028
Cathode conductivity (S/m)	80.3–100.0	0.043
Anode particle size (μm)	0.5	0.054
Anode thickness (μm)	67.3–163.7	1.3
Anode porosity	0.14–0.33	0.37
Anode diffusivity (m^2/s)	1.66×10^{-12}–10^{-11}	0.029
Anode conductivity (S/m)	1.3–100.0	0.029

3.3.3 Separator Thickness and Electrode Particle Size

Table 3.3 also shows the ranges of design variables at the optima for all cell power requirements. While some design variables change with cell power requirements, the separator thickness and electrode particle sizes invariably converge to their respective minimum bounds. While these parameters go to the bound in an idealized cell design, their effects on practical cell designs cannot be ignored.

Separator thickness converges to its minimum bound for an optimal cell design. The separator does not contribute to the physics model of an ideal cell, since no electrochemical reactions occur there. The purpose of the ions in the separator is solely to transport charges from one electrode to the other. Therefore, the separator thickness only affects the weight of the cell, which is to be minimized in order to maximize the energy density. In practical cell design, there needs to be a minimum separator thickness to prevent short-circuiting due to dendritic growths from the electrodes [134].

Smaller particle sizes are preferred as they reduce diffusion path length for lithium ions in the electrodes, and also increase interfacial surface area. A large interfacial surface area is important for ensuring adequate rate of ion transport between the two phases. Reduction in particle size results in more interfacial surface area at a smaller porosity, and hence the electrode is able to pack more active material without sacrificing the mass transfer capability. This results in a cell design with higher energy density. Increased surface area has the additional benefit of reducing the current density and subsequently the transport overpotential in the cell. Various authors have shown improved the electrochemical performance of smaller particles in positive electrodes [135, 136]. Cells made with nanoscale particles demonstrate high energy capacities and fast charge and discharge kinetics of lithium ions compared to cells with micro-sized particles. On the other hand, the cycling stability of electrodes with small particles is unfavorable due to the polarization overpotential associated with small particles and the possible increase in manganese dissolution [61, 137].

The particle size is not uniform in the electrode, but exhibits a distribution of size and aspect ratio [138]. The effect of particle size distribution was examined by Darling and Newman [139]. The authors showed that the electrodes with a particle-size distribution have larger solid-phase resistance and longer relaxation time than an electrode with uniform particle size. Particles of different sizes also have varying packing density compared to uniform particles and the discrepancies affect the porosity of the electrode. It is possible to optimize the porosity in the electrode to maximize utilization by changing the particle size distribution [140]. However, such refined control over spatial distribution within an electrode is difficult to achieve in practice and the gain in energy density is insignificant compared to an optimally designed cell with uniform porosity distribution [116].

3.3.4 Electrode Thickness and Porosity

The electrode morphological variables at optimal solutions are examined next. Figure 3.4 plots the optimal values for electrode thickness and porosity as the discharge rate is varied. When the discharge rate increases, a thinner, more porous electrode is preferred to meet the transport rate requirements. The combination of decreased electrode thickness and increased porosity reduces the amount of active materials in the cell and hence reduces the energy capacity of the cell.

Figure 3.4 also shows that the optimal cell design requires a thicker and more porous positive electrode paired with a thinner, less porous negative electrode. This is due to the difference in volumetric Coulombic capacities between the two electrodes (633 mAh/cm^3 vs. 841 mAh/cm^3). The positive electrode is therefore thicker than the negative one to balance the charge capacity. Higher porosity is required in a thick electrode to provide adequate rate of ion transport, which in turn causes the electrode to be even thicker. This shows that to achieve optimal energy density, it is essential to that the thick electrode should either have very high transport coefficient or be made of small particles in order to meet mass transfer requirements and to maximize the packing efficiency of active materials.

The changes in electrode thickness and porosity can be quantified by plotting the mass

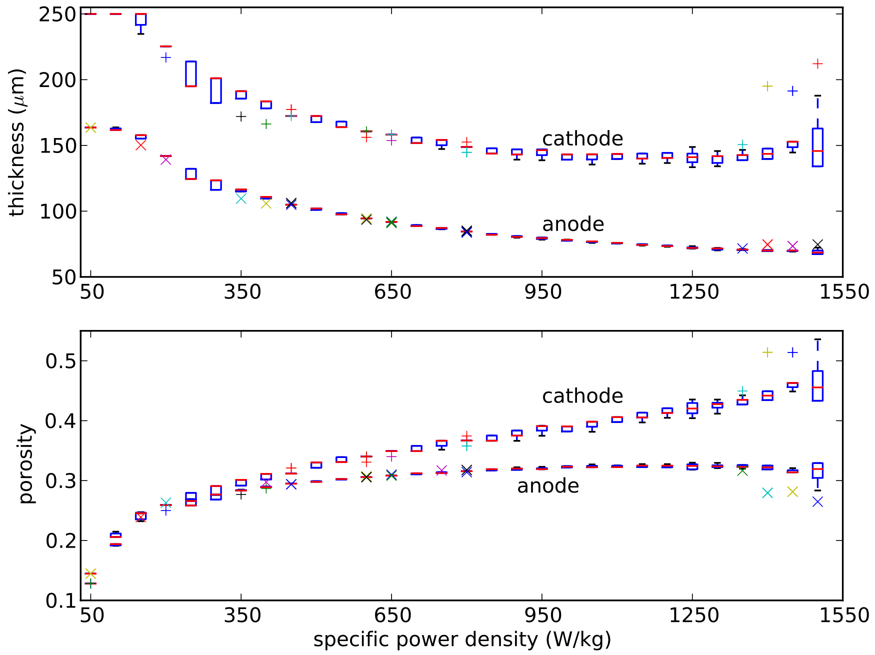

Figure 3.4: Variations of electrode thickness and porosity of optimal cell designs with respect to cell power requirement

ratio of positive to negative active materials, given by:

$$\gamma_M = \frac{L_+ \epsilon_+ \rho_+}{L_- \epsilon_- \rho_-} \tag{3.4}$$

where L is the electrode thickness, ϵ is the mass fraction of active materials, ρ is the solid density, and the $+$ and signs denote positive and negative electrodes, respectively. The optimal mass ratios range from 2.77 to 2.85, as shown in Figure 3.5, which is consistent with the optimal mass ratio of 2.8 reported by Tarascon and Guyomard [141]. The optimization results also show that the optimal mass ratio for a well-designed cell is not constant but is a linear function of the cell power, although the overall variation in the mass ratio is less than 3%.

The small variation in optimal mass ratio is attributed to the fixed cutoff voltage of 3 V, which results in a slightly different SOC at the end of simulation. The positive to negative electrode charge capacity ratio is also plotted in Figure 3.5, and is given by:

$$\gamma_C = \gamma_M \frac{q_+ \Delta y}{q_- \Delta x} \tag{3.5}$$

where q denotes the Coulombic capacity of active material in mAh/g, Δy and Δx represent the change in stiochiometric lithium coefficients in the cathode and anode, respectively.

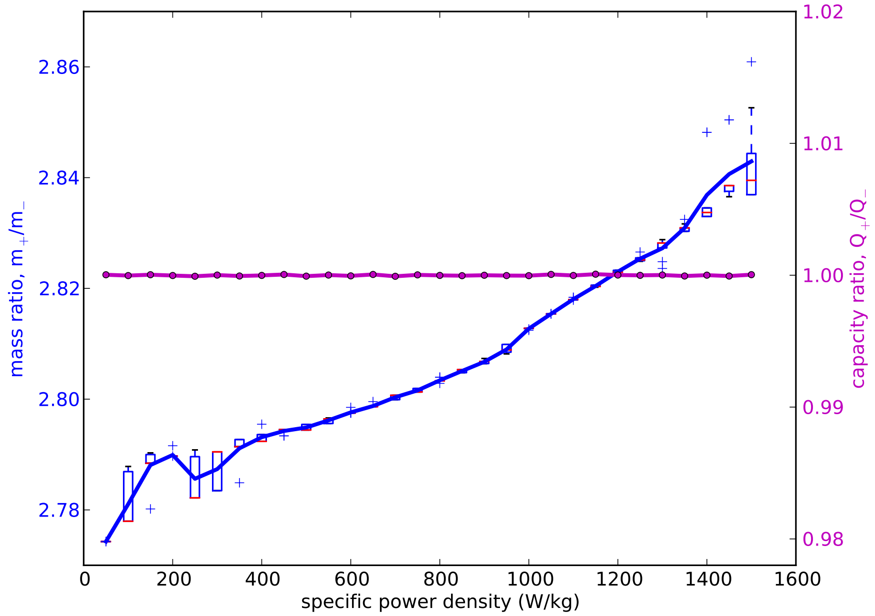

Figure 3.5: Active material mass ratio and charge capacity ratio for optimal cell designs

Note there is balance between positive and negative charge ratio for all optimized cells. This is the result of charge conservation. If the SOC remaining in the cell at the cutoff voltage is taken into account, the actual capacity ratio varies slightly from 0.99 to 1.02. The slight imbalance in capacity ratios maximizes the SOC range during which the cell voltage is above the cutoff voltage, and subsequently maximizes the amount of useful energy extracted during galvanostatic discharge. In practical cell designs, the negative electrode often has a larger capacity to ensure full utilization of the positive electrode and to compensate for loss of cyclable lithium due to side reactions such as solid electrolyte interface (SEI) layer formation. Such side reactions are not included in the current model and their effects on cell behavior are ignored. The proximity of the capacity ratios to unity for optimal cell designs at all power requirements validates the approach of requiring charge balance in the electrodes for preliminary cell design.

3.3.5 Conductivity and Diffusivity

The results from the various optimization runs initialized from different starting points indicate that the diffusivity and conductivity values do not converge to specific values at the optimal designs. Initialization from different starting points result in different final design points as well. The conductivity value range used in this study reflects cathode materials already doped with conduction-enhancing carbon additives [142]. While higher values are favored, in this range the cell performance is relatively insensitive to change in conductivity.

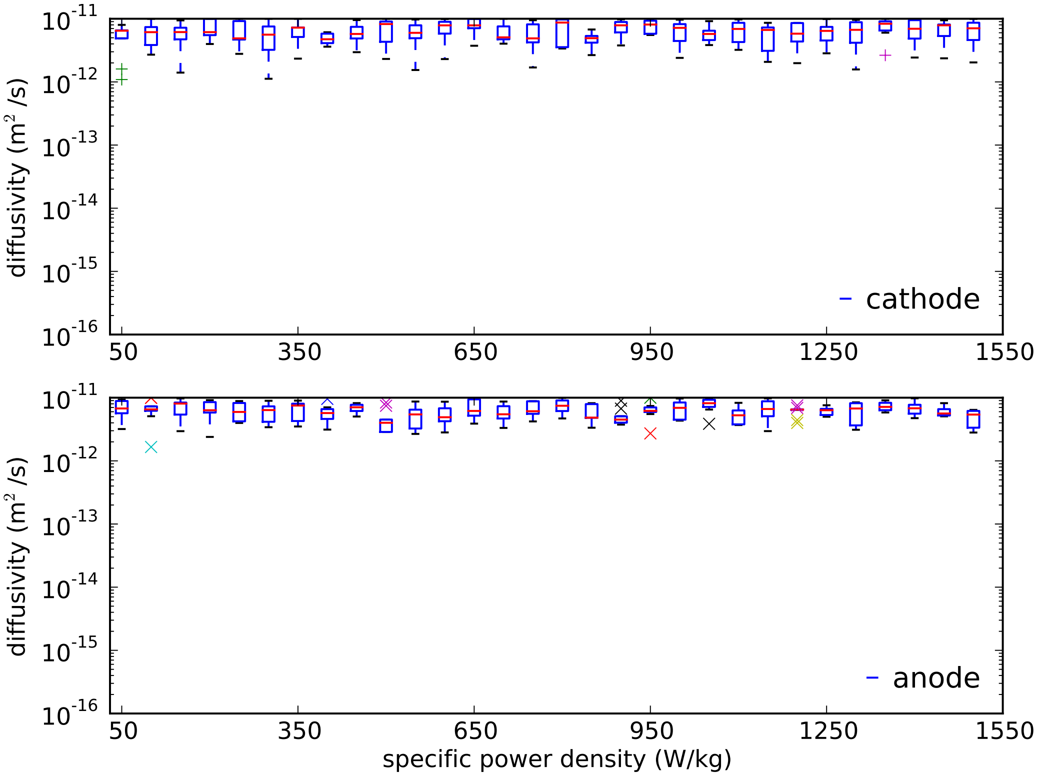

Figure 3.6: Diffusivity variations at optimal cell designs. Diffusivities need to be high at optimal cell designs to facilitate ion movement.

The diffusivity ranges at optimal cell designs are plotted in Figures 3.6, which shows the variations of diffusivity over the entire diffusivity range, and 3.7, and presents the close-up view that spans only one order of magnitude. One can see that for all cases the diffusivity values of the optimal designs converge close to the upper bound, with values ranging from 10^{12} to 10^{11} m^2/s. Given that the diffusivity bound spans 5 orders of magnitude, the optimal diffusivity ranges are small. Du et al. [114] have shown that the performance of the lithium manganese batteries is related to a dimensionless time τ, which is defined as the ratio between the discharge time t_{dis}, and the diffusion time, t_{dif} , i.e.,

$$\tau = \frac{t_{dis}}{t_{dif}}; \quad t_{dif} = \frac{r^2}{D_s} \tag{3.6}$$

where r and D_s are the solid particle radius and bulk diffusivity in the positive electrode,

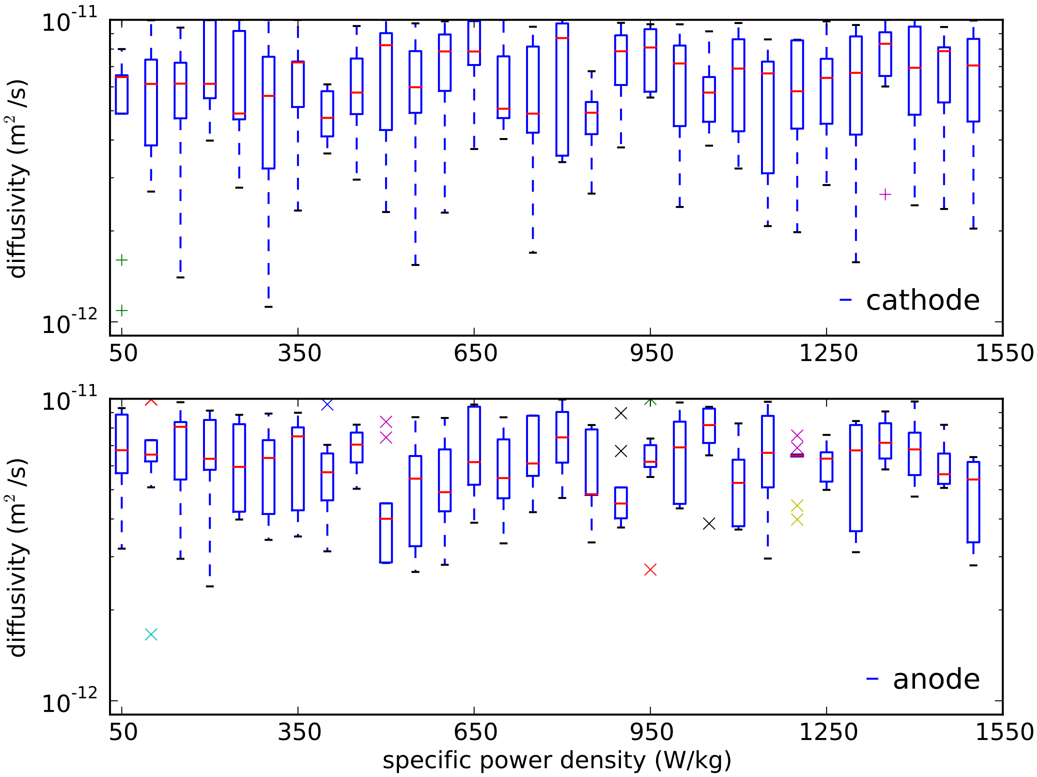

Figure 3.7: Close-up view of diffusivity distributions at optimal cell designs. While the diffusivity values need to be high, they do not converge to any specific values.

respectively. Cell designs for which τ is greater than unity demonstrate very little increase in energy capacity upon further increase in diffusivity. All optimal designs converged to the smallest particle sizes given by the lower bound, and hence this results in very large τ, even at high cycling rates such that the cells are diffusion-limited only when the bulk diffusivity is close to the lower bound of 10^{-16} m^2/s.

To examine the effects of diffusivity on energy density, a one-dimensional sweep of diffusivity is carried out at the optimal design points, with all other design parameters fixed. The differences between the energy densities and the maximum achievable values are plotted as functions of bulk diffusivities and dimensionless time τ in Figure 3.8. Effects of diffusivity on energy density at four representative discharge rates are shown. The values of dimensionless time, τ, at the optimal cell designs for all four cells are much greater than unity. As the value of τ decreases as diffusivity decreases, the energy density of the cell decreases as well, but the reduction is not significant. As shown in the right-side plots in Figure 3.8, the decrease in energy density is more than 1% only when anode τ is close to the

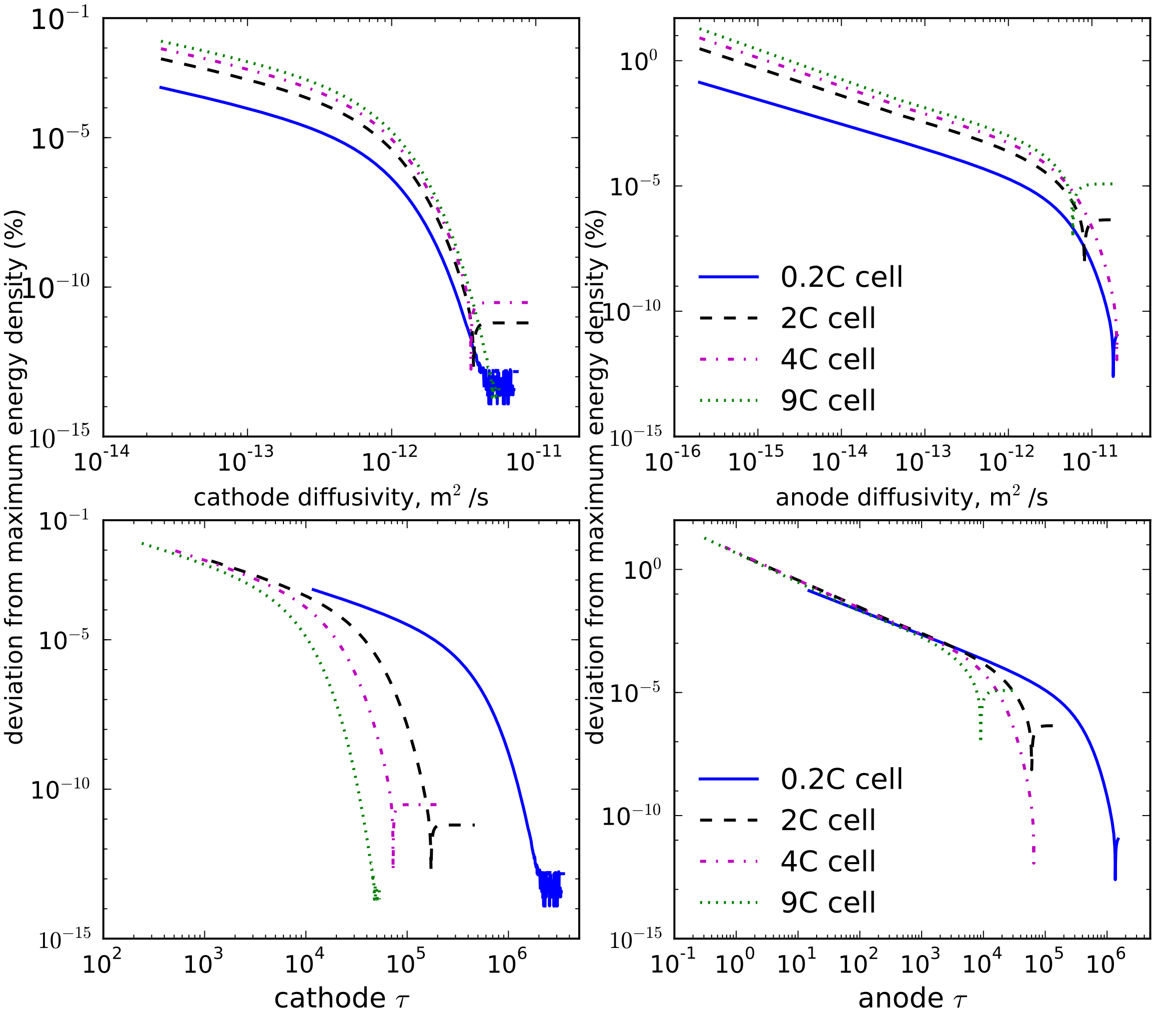

Figure 3.8: Variation of energy density as a function of normalized diffusivity

value of unity, which corresponds to a decrease in diffusivity of three orders of magnitude from its optimal values. Figure 3.8 also indicates that the effects of diffusivity on energy density increases as cell power requirement increases. This is to be expected, as higher cell power requires higher effective diffusion rate, which is directly proportional to the bulk diffusivity.

That an optimal cell design should have diffusivity as large as possible is a trivial solution. However, the objective of the analysis done here is to quantify the effects of diffusivity on cell performance. Results for Table 3.3 and Figure 3.8 show that cells with suboptimal diffusivity suffer only small decreases in energy density if the optimality of other design variables can be guaranteed.

In the current cell model, the bulk material properties are treated as constants, and the effective properties are only functions of porosity via Bruggemans equation [89]. In reality, the bulk properties are functions of the electrode material compositions and particle sizes as well. Zhu et al. [143] showed that the aggregation of carbon additives to active material as function of particle size, carbon-to-active-material mass ratio and temperature. Decreasing particle size was shown to reduce the amount of carbon particles attached to active materials, hence limiting the conductivity. A more refined treatment should include the dependence of material properties on other cell variables, which would lead to more realistic electrode designs.

3.3.6 Practical Battery Optimization

Results shown in the above sections have provided the theoretical guidelines to optimize the battery performance. Maximizing the energy density of a lithium-ion battery cell requires a combination of optimal engineering design provided via numerical optimization as well as precise manufacturing control over the design parameters. Optimal mass ratio has often been cited in the experimental as well as simulation studies as key to maximize the battery capacity [144, 127]. It is mainly a function of the charge capacity of the active materials, however it is also dependent on other aspects such as the OCV curve, the remaining capacity at the cut-off voltage, and the amount of lithium lost to the SEI layer. Consideration of the additional factors causes the mass ratio to deviate from the optimal one given by the charge capacity balance and the precise value can be provided via optimization results.

Morphological change due to external pressure loads on battery needs to be accounted for to ensure the right electrode porosity distribution to meet the mass transfer requirement. Compression on electrodes due to either battery assembly or mechanical loading can alter the porosity composition by as much as 40% [145]. Therefore it is important to simulate the exterior environment of the battery pack to ensure that the post-assembly electrode properties are as close to the theoretical design guideline as possible.

The quality control of the electrode materials is a key aspect in providing high energy density. Optimization results have shown that keeping particle size small is important to minimize diffusion path length. At the same time the uniformity of the particle sizes is critical in ensuring high Coulombic capacity [139] as well. Refined manufacturing process to minimize contact resistance at the current collector/ electrode interfaces also plays a key role to minimize the overpotential that cannot be accounted for the transport-based cell model [127].

3.3.7 Optimizer Performance

The CPU time and the number of iterations taken to reach convergence are plotted in Figure 3.9. Due to the randomized initial starting points, the number of iterations taken to reach convergence differs significantly. The average CPU time decreases as the cell power requirement increases. Optimization for the 50 W/kg/m^2 cell, which corresponds to a cycling rate of 0.2 C, required on average 62 hours to reach convergence; while the 1500 W/kg/m^2 (9 C) cell required about 26 hours. This is because a low powered cell requires more time steps to reach the cutoff voltage, and hence requires longer CPU time per function evaluation.

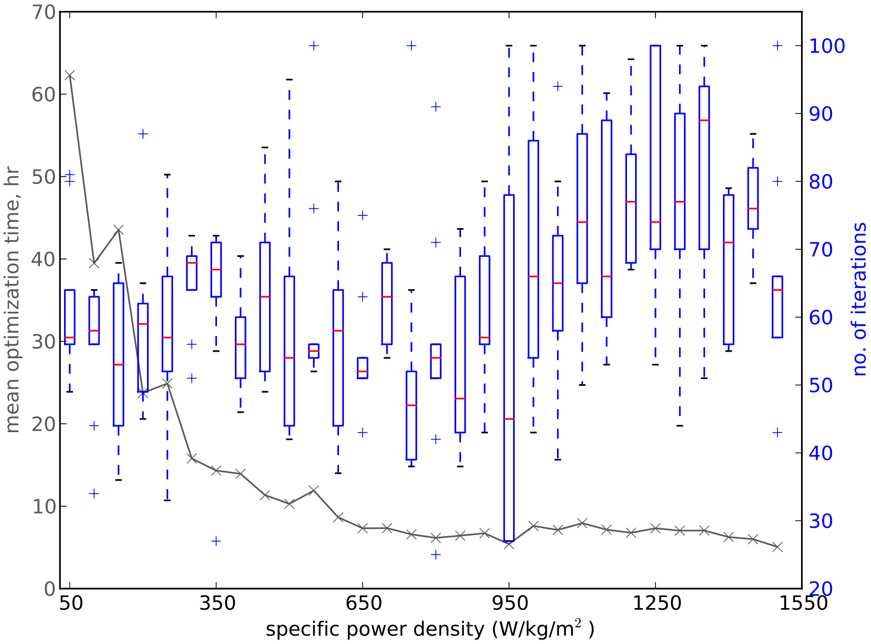

Figure 3.9: Number of iterations and optimization time versus cell power requirement

3.4 Summary

In this chapter, a new numerical framework is developed to address the inadequacy of using ad-hoc rules and parametric analysis to design battery cells. The objective is to automate cell designs and provide mathematically optimal designs. The framework couples the physics-based cell model explained in Section 2.2.1 with a gradient-based optimization algorithm (Section 2.4.2). In the present study the framework is applied to maximize the gravimetric energy density of a lithium-ion cell with manganese dioxide cathode and graphite anode under different discharge scenarios. A complete design of the cell that takes both morphological and transport parameters is shown here, and the numerical relations of how the optimal electrode parameters vary with the power requirement are quantified. The gradient-based optimization framework is able to efficiently find the optimal cell designs for each power requirements.

All optimal cell designs have the smallest possible particle size and separator thickness. This is to minimize diffusion path length and to reduce the non-energy contributing component mass. The electrode thickness decreases and the porosity increases as the cell power increases, in order to satisfy increasing mass transfer requirement. The decrease in electrode thickness and increase in porosity at higher discharge rates can be quantified via the active material mass ratio and the charge capacity ratio at optimal designs. The charge capacity ratios remain at unity for all optimal cells and the computed optimal electrode mass ratio of 2.8 is consistent with the ones reported in literature. To maximize the useful energy density, there are slight variations in the optimal mass ratios as the discharge rate changes. This is to maximize the range of SOC that the cell voltage remains above the cutoff voltage. Bulk transport parameters, such as diffusivity and conductivity, need to be as high as possible, but their effects on energy density are limited. A non-dimensional analysis of the discharge time versus diffusion time indicates that their effects on energy density is only significant if the dimensionless ratio greater than one.

The current framework is able to obtain mathematically optimal designs and provide the exact electrode morphological parameters needed to achieve maximum energy density. Its practicality can be improved by including additional processes due to various capacity fade mechanisms and micro-scale constraints. Factors such as SEI layer formation alter the active material mass ratio as the charge capacity has to be balanced after, by accounting for the consumption of cyclable lithium by various side reactions. The electrode dissolution and lithium plating on charging are likely to limit the minimum particle sizes and separator thicknesses as well. Accounting for these processes would introduce additional constraints to the design problem and further restrict the feasible design space.

CHAPTER 4

Design Optimization of a Battery Pack for Plug-in Hybrid Vehicles

4.1 Introduction

The previous chapter establishes the framework for achieving maximum energy density of a single lithium-ion cell subject to power constraints. Such design methods may be sufficient to compute the optimal battery designs for personal electronics, where the battery design is simple, and the discharge rate is approximately constant. The battery design for EVs, on the other hand, is much more involved, since the discharge rate of the battery cannot be expected to be constant, and the battery pack often contains thousands of cells. Slight variations in cell properties are multiplied in the pack property difference. In addition, the battery pack is required to satisfy multiple objectives and constraints to meet the drivers' demand as well as safety requirements. These criteria include energy density, specific power, voltage, energy efficiency, commercial availability of battery materials, and cost. A properly designed EV battery pack has to take into account all these factors in the design process.

There are different levels of hybrid vehicles with varying DOH, each requiring a purpose-built battery pack. Mild hybrid battery packs are mainly used to assist the ICE and to capture energy through regenerative braking. The discharge depth is shallow and the battery packs are small. Battery packs for PHEVs and EVs have to satisfy vehicle power demand and provide adequate driving range between recharging. However, the energy density of the most advanced batteries is currently still orders of magnitude lower than that of gasoline. As such, the battery packs on PHEVs tend to be heavy, bulky and expensive. This in turn limits the all-electric driving range for these vehicles, and thus optimally designed battery system is essential to maximize the potential benefits of an electric powertrain.

Various types of battery models have been developed to analyze battery performance with respect to various parameters. While numerical models provide an understanding of the physics of battery operation, optimization algorithms provide the means to maximize battery properties and performance in hybrid vehicle operations. Shahi et al. [146] applied a multi-objective optimization approach for the hybridization of a PHEV subject to Urban Dynamometer Driving Schedule (UDDS) and Winnipeg Weekday Duty Cycle (WWDC) drive cycle requirements. Wu et al. [147] described a methodology to minimize the drivetrain cost of a parallel PHEV by optimizing its component sizes. Hung and Wu [148] developed an integrated optimization strategy in which both the component sizing and control strategies are taken into consideration to maximize the energy capacity stored, while minimizing the energy consumed for a given driving cycle. Optimization of combined component sizing and control strategies were explored by Zou et al. [149] to study the hybridization of a tracked vehicle, and by Kim and Peng [150] for the design of fuel cell/battery hybrid vehicles. In all these efforts, however, EV system designers treated the battery either as a black box with energy and power output, or used simple algebraic equations to model the battery performance.

While power management, control strategies, and component sizing play key roles in achieving greater overall vehicle efficiency, a detailed optimization of PHEV battery packs has not been considered. Most of the earlier battery optimization efforts focused on single-cell optimization, where the battery was optimized for maximum energy density [111, 151, 114, 115, 116]. More recent efforts have optimized the energy capacity of battery cells with respect to different power capacities by varying the applied current [126, 117]. Most optimization studies, however, ignored the multitude of hybrid vehicle operational requirements. Specifically, the battery pack has to satisfy: (1) voltage and current constraints for both safety reasons and to minimize power electronic cost, and (2) energy and power requirements for performance. To address these issues, a numerical framework is used to optimize the mass, volume and material costs of the battery pack, while satisfying all the relevant requirements. By combining efficient numerical methods with existing battery models, waste attributed to sub-optimal pack design can be reduced. This type of analysis is especially important as EVs become more mainstream and higher volume, where small variations from the optimal solution, which may only result in slight overdesign (in terms of cost or volume), results in large penalties when compounded over large quantity of vehicles. This type of analysis also provides a rapid, cost effective design tool in the early phases of vehicle development, giving realistic guidelines on what is possible in terms of cost, size, and weight for a given battery chemistry.

In this chapter, optimization of a representative PHEV battery pack is performed using a hybrid optimization strategy explained in Section 2.4.5. Optimization is used to demonstrate that the resulting battery pack is able to fulfill the various PHEV operation requirements most efficiently, hence maximizing the potential gains of PHEV operation. Finally, three federal test drive cycles are used to evaluate the realistic performance of the optimized battery designs by comparing the all-electric driving ranges.

4.2 Problem Formulation

4.2.1 Battery Model

A battery pack model that consists of identical electrochemical cells is arranged in series and parallel, as shown in Figure 4.1. There are n modules arranged in series, and each module consists of m layers arranged in parallel. The cells are arranged in such a way that they have to satisfy the safety (voltage and current) and performance (energy and power) constraints. In reality, the cell properties differ slightly due to manufacturing imprecisions, causing variations in cell capacities. As such, accurate battery pack modeling requires each cell to be treated individually [50]. Charge equalization techniques are employed to balance the cells to enhance battery life and to maintain total capacity as well [152, 153]. Variations in cell properties also cause additional difficulties in estimating the battery SOC.

These additional details in the battery modeling are ignored, as they are not fundamental to the design philosophy outlined in this chapter. Accounting for these issues would increase computational burden without shedding new insights into the pack design. However, using the physics-based cell model as the foundation for the pack model would easily allow cell-to-cell variations and accurately reflect intrinsic cell imbalance due to variations in the amount of active materials in the cells [50].

PHEV operations require large battery packs of high energy density cells to provide adequate all-electric driving range. Currently, only lithium-ion batteries are able to fulfill the requirements. There are various viable lithium-ion electrochemical cells of different energy densities, costs and cycling stability. An energy density comparison of various lithium-ion cells using dimensional analysis has been provided by Du et al. [154]. The cells used for PHEV battery pack is identical to the ones used in the single-cell optimization shown in Chapter 3. The fixed properties of the cell are listed in Table 3.1 and will not be repeated here. In addition to the fixed parameters of Table 3.1, the cycling rate is kept constant and the negative to positive electrode Coulombic capacity ratio is fixed to one in the PHEV battery design. For an ideal cell, equality in the electrode charge capacities results in optimal cell designs, as shown in Figure 3.5. In reality, commercially available lithium-ion cells are made with negative to positive electrode charge capacity ratios larger than one. This is to compensate for cyclable lithium loss due to SEI formation in the initial

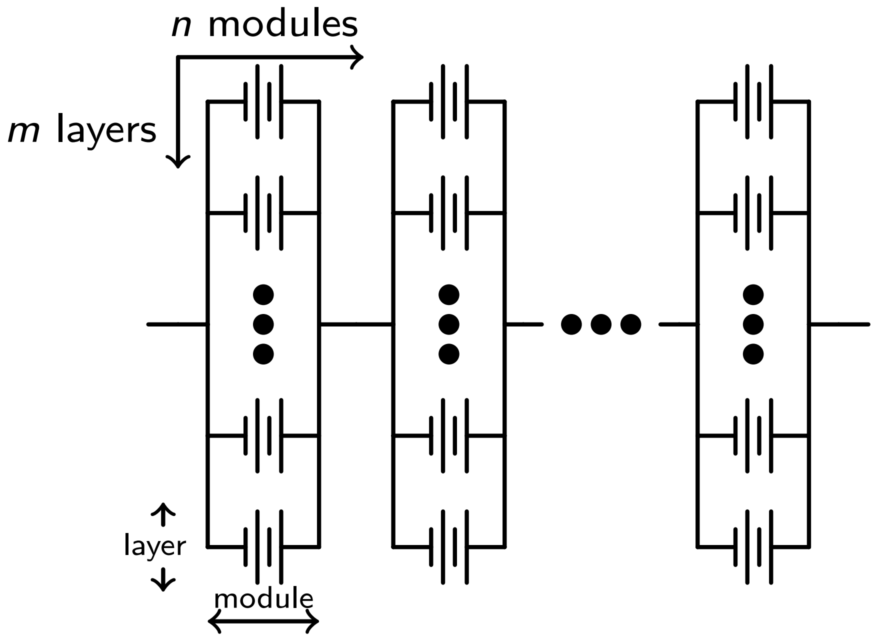

Figure 4.1: Layout of a battery comprised of uniform cells

phase, and to prevent lithium plating from occurring during charging.

In addition to the fixed variables, six free variables (Table 4.1) are selected to determine the optimal cell design and pack configuration that best fulfills the pack requirements. These six variables are selected because they represent design parameters that can be readily manipulated by the battery manufacturer to tailor the battery pack properties. There are other parameters, such as diffusivity and conductivity, as well as electrode particle size, that also affect the performance of the cell. Results from the previous chapter [126] showed that in the absence of degradation mechanisms and side reactions, these other variables should go to the bounds at optimal cell designs. Their relative effects on energy density of the cell were also shown to be less than the morphological parameters chosen for this study [114]. Therefore, these are treated as fixed parameters in this study. Among the six variables, the electrode thicknesses and porosities are morphological parameters that balance the amount of energy content in the cell with the ion transport requirement. A thicker electrode contains more active material for the intercalation process, and hence higher energy capacity. A more porous electrode allows higher rate of ion transport by increasing the effective transport coefficient. However, this reduces the fraction of charge-storing active materials and overall capacity of the cell. The competing effects of higher energy and higher power results in an optimal cell design that must reach a compromise between energy and power. The cutoff voltage determines the lowest SOC in the cell that can still fulfill the power requirement. The peak power available is dependent on the capacity remaining in the battery and must be accurately determined to avoid over-discharging the battery. While the SOC and cell voltage required to calculate peak power can be conveniently extracted from the cell model in the current framework, a more practical approach would involve a multi-parameter, model-based method [155] to estimate the peak power. The last variable is the number of cells connected in parallel within each module, which also determines the maximum current of the pack. The number of modules connected in series is fixed by the maximum voltage of the battery pack, which will be explained in greater detail at the end of this section.

Table 4.1: Design variables are the morphological parameters and battery layout variables that can be easily altered by battery designer.

Parameters	**Lower bound**	**Upper bound**
Cathode thickness (μm)	40.0	250.0
Anode thickness (μm)	40.0	250.0
Cathode porosity (μm)	0.1	0.6
Anode porosity (μm)	0.1	0.6
Cut-off voltage (V)	2.6	3.6
Number of layers	1	30

Three key properties of the battery pack are identified as the objective functions to be minimized: mass, volume and material cost. Each objective can be given as linear functions of the design variables:

$$\begin{aligned}\text{Mass} &= nmA\sum_j\sum_i \epsilon_{ij}\rho_i l_j \\ \text{Volume} &= nmA\sum_j l_j \\ \text{Cost} &= nmA\sum_j\sum_i b_i\epsilon_{ij}\rho_i l_j\end{aligned} \tag{4.1}$$

where n and m are the number of modules and layers in the battery pack, respectively, A is the cross-section area of each cell, ϵ, ρ and b are the volume fraction, the mass density and the unit cost [156] of the constitutive materials, respectively, l is the thickness of the cell component. The index j cycles over the cell components, namely the positive electrode, separator, negative electrode, and the current collectors, while i cycles over the cell materials. Note that if the materials with higher density have higher unit prices, then the cost becomes directly correlated with the mass, and reducing the battery pack mass reduces the cost as well.

Table 4.2: Conversion of pack-level requirements to cell-level constraints

	Pack				**Cell**		
Voltage	V_{pack}	$\leq$	400 V		$n \cdot V_{cell,init}$	$\leq$	400 V
	V_{pack}	$\geq$	280V		$n \cdot V_{cell,end}$	$\geq$	280 V
Current	I_{pack}	$\leq$	420 A	$\Longrightarrow$	$m \cdot I_{cell}$	$\leq$	420 A
Energy	E_{pack}	$\geq$	12 kWh		$nm \cdot E_{cell}$	$\geq$	12 kWh
Power	P_{pack}	$\geq$	120 kW		$nm \cdot P_{cell}$	$\geq$	120 kW
Charge balance					Q_+	=	Q_-

Equations (4.1) show that the objective functions are linear with respect to the design variables. Minimization of the objective functions without proper consideration of constraints results in the trivial solution where all design variables are at their lower bounds. Therefore, a useful battery pack design requires satisfying appropriate design constraints. These safety and performance requirements impose limits on how close to the lower bounds the design variables can go. The constraints for the problem are listed in Table 4.2.

The energy of the battery pack is computed by galvanostatic discharge of the cells at 1 C cycling rate, while the maximum power is the average power available during a 10-second maximum current pulse at the end of the 1 C discharge. The maximum power is computed at the lowest SOC, as this is the point where cell voltage is the lowest. If the battery can meet the power requirement at the end of discharge, it can meet the power requirement throughout its operation. The 10-second current pulse requirement provides a good estimate of the maximum power required for vehicle operation. Based on the constraints outlined in Table 4.2, the maximum voltage limits the number of battery modules connected in series. The maximum voltage in a cell is the OCV at the fully charged state, and the maximum pack voltage divided by this value provides the number of modules allowed in the battery pack. In this study, the number of cells connected in series is fixed at 99. The minimum voltage is computed at the end of the 10-second maximum current pulse and it sets the limit on the depth of discharge of the cells. Hence, the optimization problem can be simplified by replacing the voltage constraints with the fixed number of modules in the pack and the minimum cell voltage to terminate discharge.

4.3 Results

4.3.1 Discharge Profile

A typical discharge profile obtained from the cell-model simulation is shown in Figure 4.2, where both the cell voltage and the current density profiles are plotted. The small insert in Figure 4.2 shows the voltage and current profiles at the transition between the galvanostatic discharge and peak power current pulse. The sudden jump in the cell current creates a discontinuity in the voltage profile, and it is the result of a sudden increase in the current density. The cell voltage decreases rapidly as the amount of charge is depleted at a greater rate at the end of the discharge.

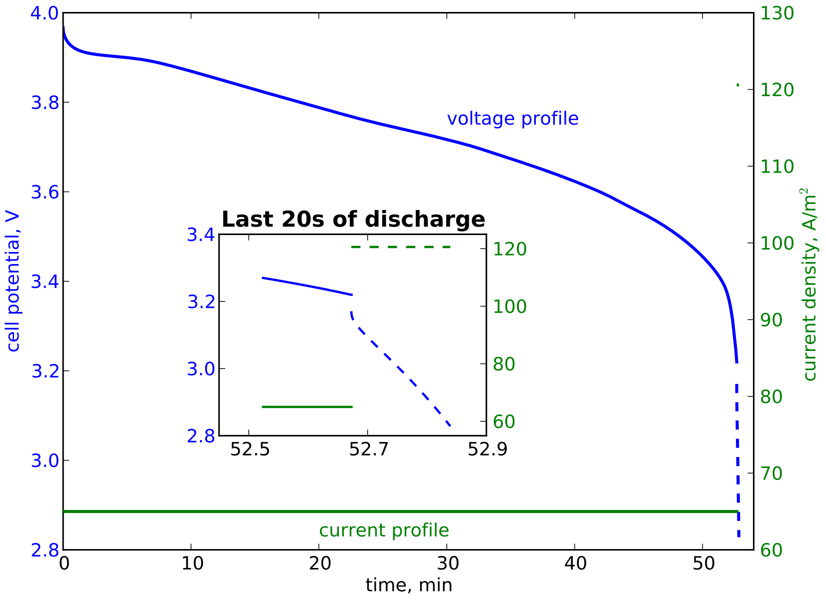

Figure 4.2: Discharge profile for a lithium-ion cell undergoing 1 C constant current discharge (main) followed by a 10-second peak power pulse at the end of the discharge (insert)

The secant method is used to obtain the maximum current during the 10-second pulse. The maximum current is defined as the largest current possible while maintaining the minimum voltage at the end of the pulse. The iterative process for the maximum current computation is shown in Figure 4.3. The final cell voltage decreases monotonically as the pulse current is increased, and the negative correlation between the maximum current and the final cell voltage is shown in the insert.

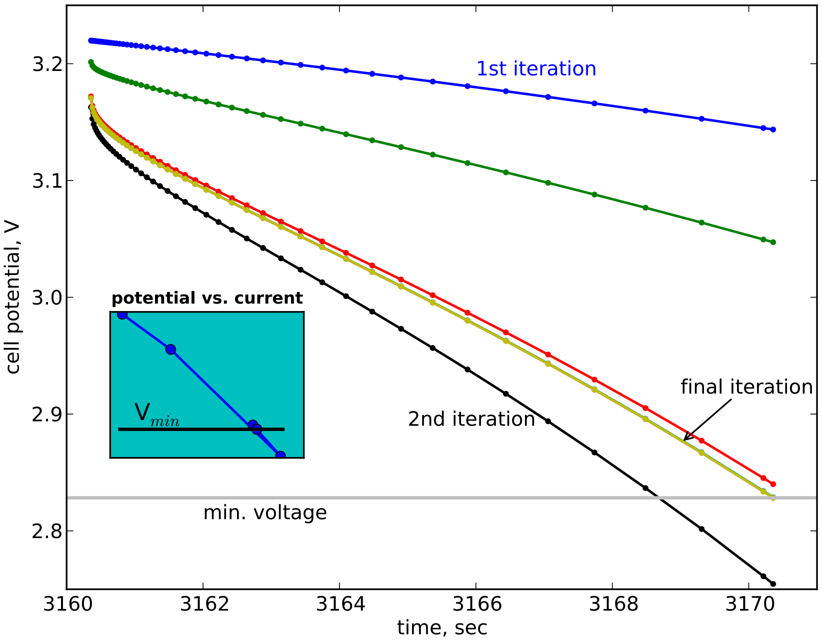

Figure 4.3: Discharge profiles of the 10-second peak current phase. The secant method is used to determine the maximum current such that the cell potential is exactly at the minimum voltage at the end of the discharge (insert)

4.3.2 Optimization Results

As mentioned previously, three different optimization problems are solved to design the PHEV battery pack: 1) battery mass minimization, 2) battery volume minimization, and 3) battery material cost minimization. The six design variables are listed in Table 4.1 and the four constraints are listed in Table 4.2. To compare the performance of the optimized cell designs, three initial pack designs are selected. The first two designs follow the general *ad hoc* guidelines for cell electrode design: the first one is a power cell with thin electrode and high porosity, and the second one is an energy cell with thick electrode and low porosity. The third one is based on the earlier work of single cell optimization subjected to a power constraint [126]. The optimized cell selected for comparison is designed at the same power-to-energy ratio as specified in the problem constraint shown in Table 4.2. The difference between the single cell and pack design philosophy is that single cell optimization is performed at one discharge rate, while the power and energy requirement for the pack design are performed at different discharge conditions, resulting in additional constraints in the design problem. The specifications for the three initial designs and their properties are listed in Table 4.3. All three initial designs satisfy the capacity balance requirement imposed on the problem.

Table 4.3: Battery cell properties of initial designs

	Power cell	**Energy cell**	**Optimized single cell**
Cathode thickness (μm)	129.9	189.8	141.7
Anode thickness (μm)	80.0	120.0	70.0
Cathode porosity	0.4	0.2	0.442
Anode porosity	0.4	0.2	0.322
Cutoff voltage (V)	3.53	3.63	3.53
Number of layers	13	13	13
Mass (kg)	86.89	126.00	87.14
Volume (dm^3)	29.34	39.62	29.52
Cost ($)	1398	1862	1401
Energy capacity [$\geq$ 12kWh]	11.9	11.8	11.9
Maximum current [$\leq$ 420A]	388.0	385.2	389.3
Peak power [$\geq$ 120kW]	121.5	123.3	121.7

Analyses of initial pack designs show that the optimized single cell and power cell designs have similar properties, with the power cell exhibiting slightly better performance. The energy cell design is the worst among the three, as its thick electrodes and low porosity result in an expensive and bulky cell without providing any energy density improvement over the other two. All three initial pack designs require 13 layers of cells in parallel to satisfy the pack constraints. This results in the energy cell designs being the heaviest, most voluminous, and most expensive.

Given that the three separate objective functions are not linear combinations of one another, the optimal design for one objective should not be the optimum for another. Table 4.3 shows that the power cell design performs the best for all three objectives, it is thus not expected to be the true optimal design. In addition, while the power requirement of the pack is exceeded, the energy capacity requirement is not fully satisfied by any of the three initial designs. Therefore, further improvement is possible and can be achieved using numerical optimization.

The gradient-free optimization is first carried out to obtain an approximate estimate of the optimal design and to determine the integer value of number of cell layers. A representative iteration history of cost optimization is shown in Figure 4.4. Note that ALPSO is a population-based optimization method such that at each iteration, there are multiple design points existing simultaneously. The plots shown here contain only the design point that best satisfies the design problem criteria at each iteration, evaluated by the Lagrange function for each particle [97].

Subplots a, b and c in Figure 4.4 show how the six design variables change during

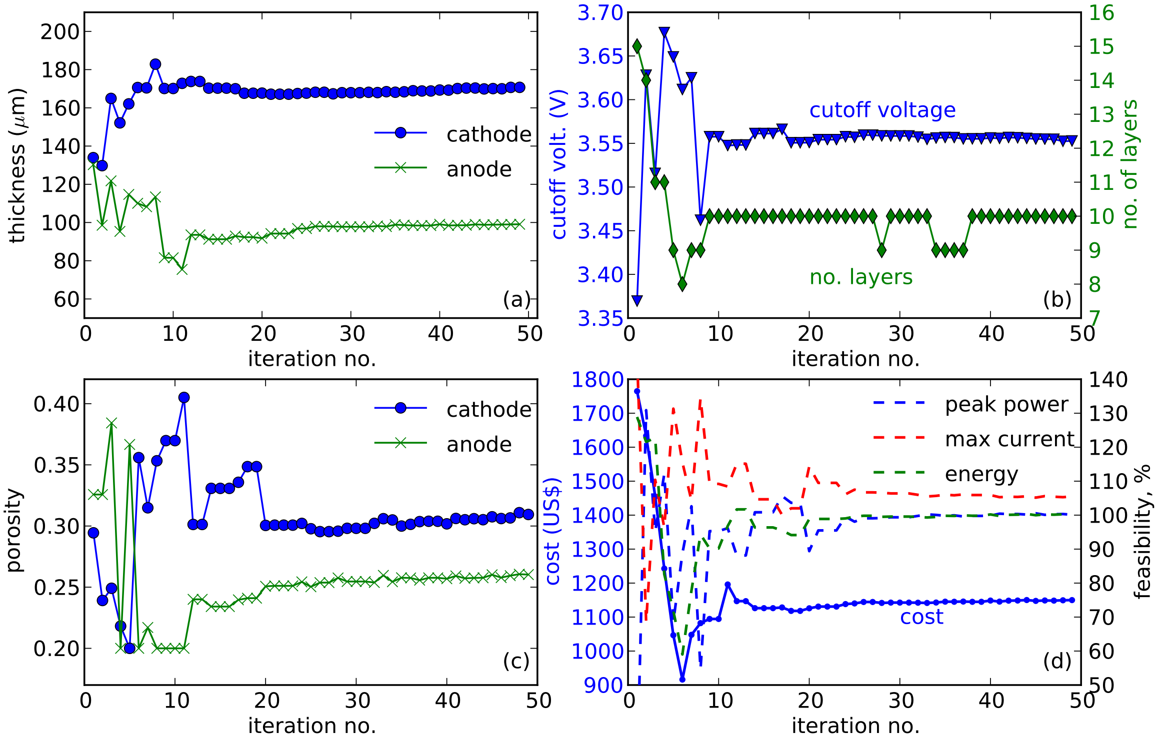

Figure 4.4: Iteration history of an optimization to minimize battery cost showing the evolution of: a) electrode thicknesses, b) cutoff-voltage and no of layers, c) electrode porosities, and d) cost and normalized inequality constraint values

the iteration, while subplot 4.4d shows the evolution of the objective function (solid line) and the normalized constraint values (dashed lines) during the optimization process. The normalized constraint value is given as a percentage, with 100% and above indicating that the constraint is satisfied. The charge balance constraint is an equality constraint that has to be satisfied exactly at all times and hence is not plotted. The optimization history shown in Figure 4.4 can be broken down into three phases. The initial design has large number of layers and this resulted in a high battery cost and extremely high current. The first six iterations reduce the number of layers and hence lower the current to below the maximum allowed value. However, this results in energy and power requirements not being met. Further adjustment of the design variables in the next five iterations results in the cell design converging towards the final cell design, at which point the energy and power constraints are fulfilled exactly. Given the competing effects of energy and power in the battery cell, this result is expected, as the optimal cell design would be one that satisfies but does not exceed both requirements. The maximum current is well below the maximum allowed level, indicating that it is not an active constraint.

Multiple optimizations runs of ALPSO were performed for each optimization problem.

The best results are listed in Table 4.4. Optimizing for mass and material costs results in very similar optimal cell designs. In fact, the optimal design obtained for cost minimization has the lowest battery pack mass as well. Given that reduction in battery mass naturally leads to less materials and hence lower cost, this result is not surprising. While the difference between the minimal-mass weight and minimal-cost weight is within the convergence tolerance of the optimizer, it also indicates that ALPSO is unable to locate the true optima in this situation, such that the final result found for mass minimization problem is sub-optimal.

Properties	**Objective function**		
	Mass	**Volume**	**Cost**
Mass (kg)	74.97	75.67	74.90
Volume (dm^3)	24.91	24.02	24.48
Cost ($)	1153	1169	1147
Cathode thickness (μm)	169.8	141.9	168.8
Anode thickness (μm)	104.7	86.4	99.8
Cathode porosity	0.321	0.272	0.305
Anode porosity	0.314	0.252	0.269
Cutoff voltage (V)	3.52	3.53	3.53
Number of layers	9	10	9
Energy capacity [$\geq$ 12kWh]	12.0	12.0	12.0
Maximum current [$\leq$ 420A]	398.4	395.0	396.6
Peak power [$\geq$ 120kW]	120.1	119.9	120.1

Table 4.4: Preliminary designs after gradient-free optimization. Results shown are the best-available ones due to stochastic nature of the ALPSO algorithm.

A comparison between Tables 4.3 and 4.4 shows decreases of 13.4%, 18.1%, and 17.9% in mass, volume and cost respectively from initial to optimal designs. Compared with the best initial cell designs, all three optimal designs have thicker electrodes and lower porosities. Therefore, each cell has higher energy density, while still satisfying the power requirement. The energy and power requirements are satisfied with far fewer cells (9 or 10 layers vs. 13), and hence better overall pack properties.

There are some differences between the three optimized designs. The mass and cost minimization problems produce optimal cell designs that have thick electrodes, such that the cell has as much active material for lithium ion intercalation as possible. This is to maximize the energy density of the cell, and to reduce the total amount of materials needed. While the cost minimization problem results in a battery pack lighter than the one obtained from the mass minimization problem, the difference is within the convergence tolerance of ALPSO. Volume minimization, on the other hand, produces an optimal cell design that has thinner electrodes with lower porosities. This results in a cell design that has lower gravimetric energy density, but higher volumetric energy density compared to the designs for the other two problems.

Table 4.5: Refined optimal designs obtained using gradient-based optimizations

Properties	**Objective function**		
	Mass	**Volume**	**Cost**
Mass (kg)	$\underline{74.77}$	79.53	75.06
Volume (dm^3)	24.49	$\underline{23.85}$	24.37
Cost (\$)	$\underline{1146}$	1241	$\underline{1146}$
Cathode thickness (μm)	169.2	111.7	169.4
Anode thickness (μm)	99.4	64.3	97.5
Cathode porosity	0.310	0.220	0.300
Anode porosity	0.270	0.150	0.245
Cutoff voltage (V)	3.53	3.55	3.54
No. of layers	9	12	9
Energy capacity [$\geq$ 12kWh]	12.0	12.0	12.0
Maximum current [$\leq$ 420A]	395.9	392.5	394.4
Peak power [$\geq$ 120kW]	119.9	120.1	119.8

The optimal cell designs are further improved by using SNOPT to refine the continuous cell variables. The gradient-based optimization is initiated at the optimal designs obtained from ALPSO. The number of layers in each module, which is a discrete variable, is fixed at the values around the optimal number of layers obtained via ALPSO, while the gradient-based optimizer fine-tunes the continuous variables. The results obtained using SNOPT are listed in Table 4.5. Again the mass minimization and cost minimization solutions are almost identical, and the material cost difference between the two is less than one dollar. The volume minimization problem produces a battery pack with much thinner electrodes and lower porosities. Comparing the SNOPT and ALPSO volume minimization results, the cathode and anode thicknesses are 21.3% and 25.6% thinner, respectively, while the porosities are 19.1% and 40.5% lower. The number of cells required increases by 20%. The low electrode porosity means the cell design is less adequate for handling high discharge rates. However, this is alleviated by having a larger number of cells connected in parallel, and hence a smaller current density through each cell. The SNOPT optimal design has higher mass and material cost, but lower volume. While utilizing larger number of cells with lower energy density may seem counter-intuitive, it demonstrates the ability of the optimizer to drive the design to achieve the objective, which in this particular instance is to minimize the volume of the pack.

Results in Table 4.5 show that improvements from gradient-free optimization to gradient-based optimization results are less than 1% for all three optimization problems. This is mainly due to the flatness of the design space near the optimum, and there is little gain in pinpointing the exact location of the optimal designs, as evidenced by the 8% difference in negative electrode porosity between ALPSO and SNOPT results. Such differences, however, may become more important as more details about cell modeling are included. For instance, manganese dissolution rate has been shown to correlate to the interfacial surface area in the porous electrode [157]. Increase in cathode porosity increases interfacial surface area and could potentially cause accelerated cell degradation. Inclusion of additional degradation mechanisms would likely add nonlinearity to the design space, further restricting the feasible design regions.

One common problem with gradient-based optimization is that it often converges to local optimum solutions instead of global best ones. To show that the solutions are indeed global optima, and that the design space near the solutions does not have local optima, the contour plots of the objective functions near the optimal regions are plotted. The region plotted is a 2-dimensional plane defined by the three optimal design points of mass, volume and cost, respectively. The plane is obtained by projecting the design space onto the plane spanned by the coordinates of the three optimal design points. These three points are transformed into the non-dimensional coordinates $(0, 0), (1, 0), (0, 1)$, respectively, on the plane. The shaded area on Figure 4.5 indicates the region where the energy, power, voltage and current requirements are all satisfied. The blue curve indicates the narrow band that fulfills the charge balance requirement, while the black lines show the design space that satisfies the integer requirement imposed on the number of layers.

In the plots shown in Figure 4.5, one can see that the objective functions vary smoothly in the feasible design space. The mass and cost contours vary monotonically in the feasible design space, while there is a local volume maximum for the volume contour plot. All three optimal design points are located on the boundary of the feasible space, again confirming that the constraints are active in this design problem. The location of the optimal designs are further restricted by the charge capacity equality constraints and the integer requirement on the number of cell layers. Based on the information available in Figure 4.5, it is clear that the optimal designs are indeed the best possible designs in the 2-dimensional plane shown here. Such information, together with the smoothness of the objective functions, gives us confidence about the global optimality of the results. The similarity between mass and cost optimal designs can also be explained from the contour plots in Figure 4.5. Comparison of the mass and cost contours reveal that the two objectives are very similar to one another in the given plane. The gradients for both objectives point in the same x-direction, and in

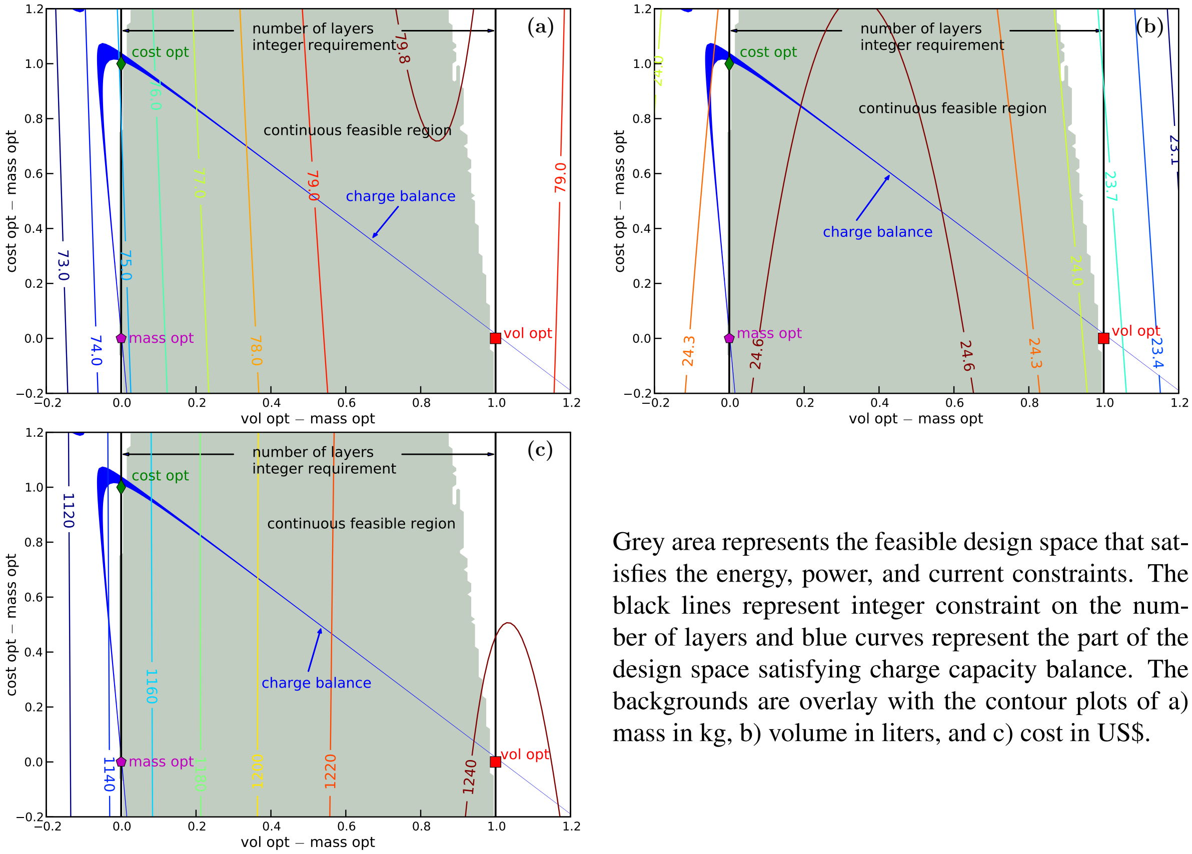

Grey area represents the feasible design space that satisfies the energy, power, and current constraints. The black lines represent integer constraint on the number of layers and blue curves represent the part of the design space satisfying charge capacity balance. The backgrounds are overlay with the contour plots of a) mass in kg, b) volume in liters, and c) cost in US$.

Figure 4.5: Contour plots of objective functions on the plane spanning the three optimal design points

both cases the best objective functions are on the left boundary of the feasible space. The similarities of the objectives result in mass and cost optimal designs being very close to each other in the actual design space.

The optimal cell design for mass minimization problem is compared with the optimal single-cell design results from the previous work [126], in which the optimal cell has the maximum energy density at constrained discharge rates. Comparison to the optimal cell at 1C discharge rate shows the PHEV pack cell design has thinner electrodes and higher porosities. This is due to the additional peak power requirement at the end of discharge, which imposes a higher ion transport requirement. The resulting cell design, while not optimal in terms of energy density, is able to meet both the energy and power requirements simultaneously, which is more important, given the variations in power demand under normal driving conditions.

Table 4.6: Properties of the vehicle used to complete the driving cycle

Properties	**Values**
Vehicle mass (kg)	1500
Passenger mass (kg)	150
Rolling resistance coeff.	0.01
Drag coefficient	0.30
Frontal area (m^2)	2.0
Motor efficiency	0.85
Drivetrain efficiency	0.8
Generator efficiency	0.85
Regenerative braking factor	0.1
Miscellaneous power (kW)	1.0

4.3.3 Driving Cycle Test

While the optimal designs obtained using the aforementioned optimization framework show better overall properties than the initial design, it is important to show that they translate to actual performance advantage in the operation of the PHEV. In this case, it is useful to compare the performance of the battery packs by simulating discharge for standard federal testing driving cycles. A standard sedan with the properties listed in Table 4.6 is used to compute the battery power required to complete the driving cycles. The required power is computed using the vehicle model shown in Section 2.3, and taking the motor and drivetrain efficiency factors, η_d and η_m, into account as well:

$$P_{batt} = \frac{P_{veh}}{\eta_d \eta_m} \tag{4.2}$$

While the drivetrain and motor efficiencies change with the power and velocity of the vehicle, they are assumed to be constant in this case.

The battery packs are discharged through the three standard federal driving cycles: UDDS, SC03 and US06, whose speed and corresponding power profiles are shown in Figure 4.6. The UDDS and SC03 cycles both mimic city driving conditions. The SC03 cycle is the more aggressive. US06 simulates highway driving condition. The highway acceleration requirements impose higher power demands on the battery, with power demands peaking at 100 kW. The battery is discharged from an initial SOC of approximately 0.8 until the minimum voltage of 280 V is reached and the total distance covered for each of the driving cycle is calculated. Calculations have shown that the minimum voltage of 280 V corresponds to a SOC level of approximately 5%. In reality, the depth of the discharge

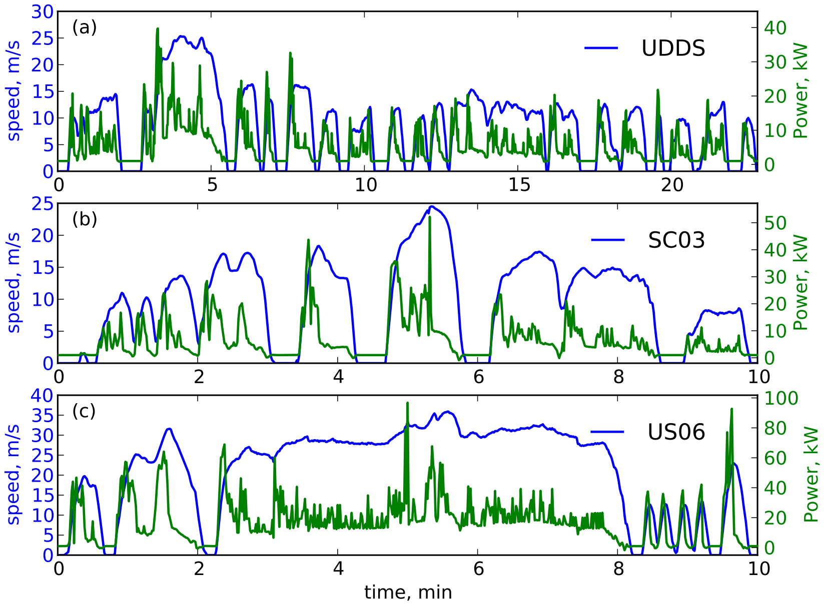

Figure 4.6: Federal driving cycle speed profiles and the corresponding battery power requirement:

of EV battery packs is much less than that, hence the all-electric range obtained here will be higher than what can be expected from actual EVs with a similar battery pack.

Both the initial design and optimal battery packs are discharged through the simulated driving cycles. The voltage and SOC profiles of the minimum mass optimal battery pack and the initial design discharged through the simulated US06 driving cycle are shown in Figure 4.7. The open-circuit voltage (OCV) curve is plotted on the same figure for comparison. The SOC profile shows that the optimal battery pack lasts longer than the initial design battery pack, resulting in 3.5% longer electric range. The initial battery design contains more cells in parallel compared to the optimal battery pack, and therefore each cell is subjected to a smaller current density. This results in higher battery pack voltage in the initial design, and less energy lost per cell due to internal resistance. However, the higher energy density of the optimal battery pack cells still results better performance overall.

The all electric ranges for various battery pack designs subject to the three driving cycles are listed in Table 4.7. For all three driving cycles, the optimal battery pack designs outperform the initial battery pack designs in terms of all-electric range. The most improvement is in the SC03 cycle discharge, for which the electric ranges of minimum-volume and minimum-cost battery packs are almost 10% better than the initial design.

While the electric driving range of the optimal battery pack designs show significant improvement over the initial design, a better measure of the battery performance is the

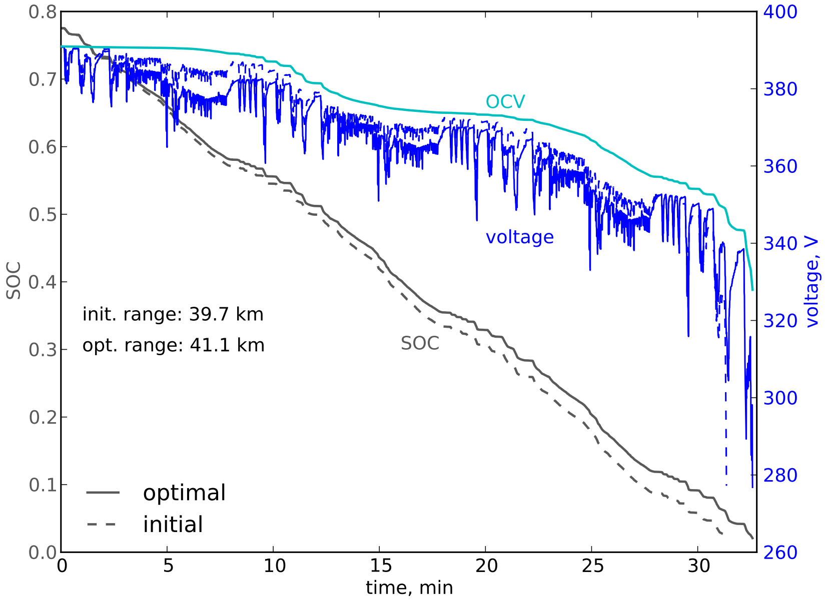

Figure 4.7: Comparison of the voltage and SOC profiles of the initial design and minimum-mass optimal battery pack discharged through the simulated US06 driving cycle

Table 4.7: All electric driving range for various battery designs

	Battery design			
Drive cycle	**Initial**	**Min. mass**	**Min. volume**	**Min. cost**
UDDS	53.7 km	57.2 km	58.1 km	58.1 km
SC03	48.6 km	52.5 km	53.4 km	53.4 km
US06	39.7 km	41.1 km	42.1 km	41.8 km

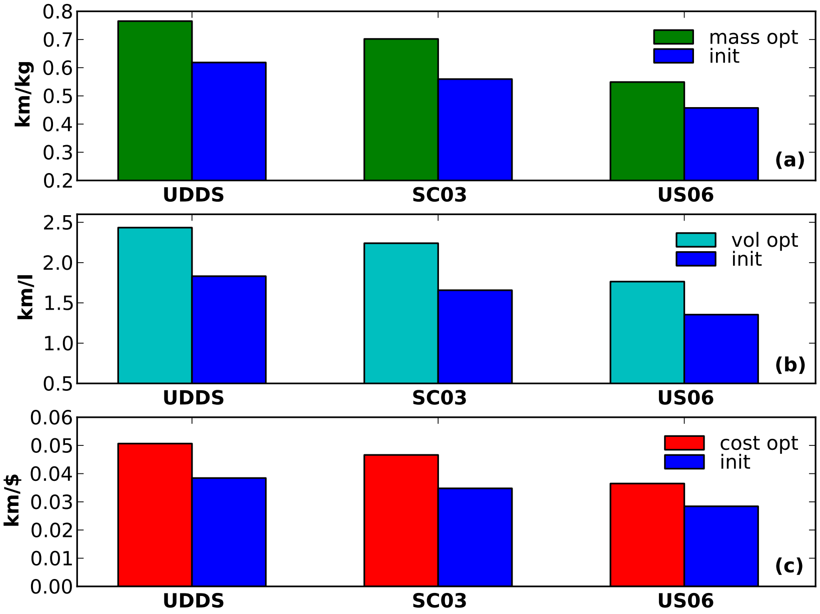

Figure 4.8: Comparison of battery performance between initial and optimal designs using driving cycle data

distance traveled per unit of battery performance metric, where the metric is either mass, volume or material cost. Figure 4.8 compares the performance of the optimal battery designs with the best initial design. While the initial and optimal designs have similar all-electric drive range, the optimal designs clearly have better performance per unit of battery performance metric. On average, the optimal battery packs show 23.1% improvement in distance per unit of battery mass, 32.8% improvement in distance per unit volume and 31.4% improvement in distance per unit cost.

The results in Table 4.7 also show that the minimum-volume battery pack has the longest electric range among the optimal battery pack designs. The disparity between the electric driving ranges of the various optimal battery packs demonstrates that while the battery packs satisfy similar energy and power requirements, the performance is dependent on the driving cycle, or control variables governing the discharge of the battery. This points to the possible advantage of performing a design-control coupled optimization. In addition, only the all-electric operating mode rather than the overall performance of the PHEV drive is considered. The problem definition is limited to minimizing the properties of the battery pack, and this allows decoupling of the battery from other drivetrain components. To truly optimize the operation of the PHEV, the hybrid mode, during which both engine and electric power are in use, and the driving conditions that favor the hybrid mode need to be considered as well. The degree of hybridization in the PHEV, which is the ratio of electric motor power to the total drivetrain power, is shown to affect the optimality of the drivetrain components performance [19]. Therefore, the overall hybridization scheme of a PHEV is defined by the battery, electric motor, and internal combustion engine collectively [146]. Inclusion of various components also necessitates the coupling of power control strategies with design parameters to determine the optimal performance. Kim and Peng [150] showed that the “power management and design” optimization improved fuel economy by 17% relative to “power management only” optimization. Consideration of the engine and electric motor sizes could allow for battery design that best meets the peak power demand during climbing and acceleration, while keeping the engine operation at maximum efficiency.

4.4 Summary

This chapter extends the battery optimization framework shown in Chapter 3 to the design of a PHEV battery pack. Given the nonlinear and mixed-integer nature of the pack design problem, a hybrid optimization approach that takes advantage of type of optimizer is developed. A gradient-free optimizer is first used to obtain an approximate estimate of the optimal design and to obtain the optimal integer design variables. The design is then further refined using the gradient-based optimization. Most EV system optimization tends to treat the battery as a black box or a simplified circuit model, thus ignoring the transport laws governing the behavior of the electrochemical cells. The framework developed here provides detailed battery design in the context of EV operation. It enables optimization of the battery pack layout, as well as the morphological design parameters of the individual cells.

Three optimization problems of minimizing the battery pack mass, volume, and cost are demonstrated using the optimization framework. Comparisons between the initial designs using general guidelines and the optimal designs show overall improvements of 13.9%, 18.7% and 18.0% in battery mass, volume, and cost, respectively, thus validating the necessity of a numerical approach to the battery pack design. The optimal designs also perform better in real drive cycle simulations. The improvements in battery pack properties can be translated to 23.1% increase in distance traveled per unit mass, 32.8% increase in distance per unit volume, and 31.4% increase in distance per unit cost. The electrochemical cell in this case is assumed to be ideal, so additional capacity fade mechanisms should be considered in the future.

The design methodology shown here is useful in obtaining the best possible initial designs, from which further refinement can be carried out by accounting for additional details, such as degradation mechanisms and manufacturing constraints. The driving cycle comparison shows that the three optimal battery pack designs, while satisfying the same set of constraints, have slightly different all-electric driving ranges. The minimum volume battery pack has the furthest driving range for all three federal driving cycles. This is due to the difference between design discharge condition and the actual driving cycle conditions. Therefore, it could be useful to perform a cell design optimization that uses the driving cycle power requirement as the discharge profile. Multi-point design schemes [26] can be employed to ensure the obtained optimal solution is not specific cycle beating.

CHAPTER 5

Multi-Cell Design Optimization for Electric Vehicle Battery Packs

5.1 Introduction

The previous chapter demonstrates the design optimization of a battery packs for PHEV operation. The optimization algorithm is able to minimize the battery pack mass, volume or cost subject to various constraints. The problem formulation follows the conventional philosophy of using uniform cells for battery pack design and altering the cell power-to-energy ratio for different battery packs. However, given that energy and power are competing objectives, cell designs that have to satisfy both are sub-optimal in both aspects. Therefore, it is unclear whether a uniform-cell pack design is the best way to fulfill both requirements in an EV application.

The Pareto front in Figure 5.1 shows that the power-to-energy function of optimal cell designs is nonlinear function—as the discharge current is increased, the power capability of the optimal cell design is increasing at a rate faster than it is losing energy capacity. There are two reasons affecting the power to energy relation of optimal cell designs. As the power requirement is reduced, the rate of ion transport required in the electrode is reduced as well. The optimal electrode is one that contains more active materials and less electrolyte. Therefore, the lower-power optimal cell design gains additional energy density compared to the higher-power optimal cells. In addition, Equation (2.9) shows that the power lost to the internal resistance is proportional to the square of the current. As the cell power is reduced, the amount of power lost to overcome the internal resistance is reduced as a quadratic function of current density, thus further increasing the energy density of the optimal cells.

The Ragone plots shown on Figures 3.3 and 5.1 indicate that the energy density of a lower-power optimal cell design decreases rapidly as the power requirement is increased beyond its design point, while a higher-power optimal cell is unable to increase its energy

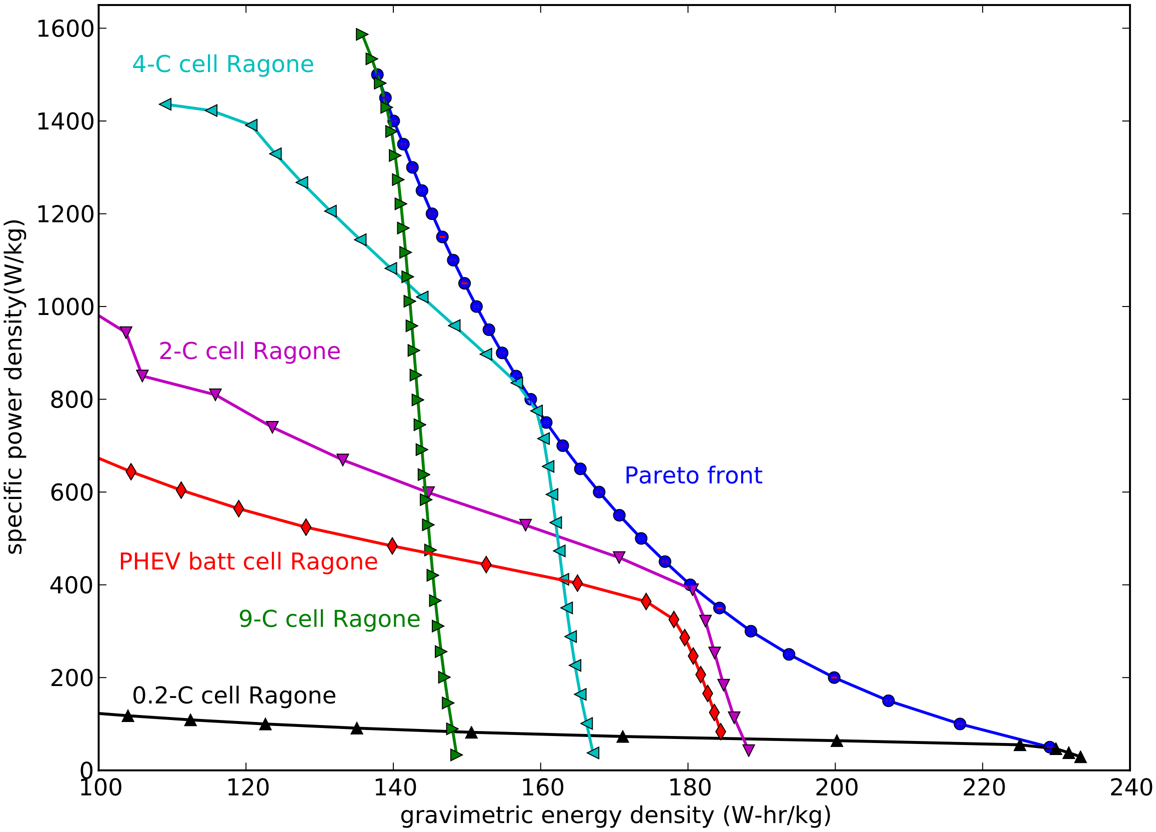

Figure 5.1: Pareto front of optimal single-cell designs on a normal scale, comparing the single-cell design with pack cell design

density significantly as the cell discharge power is decreased, resulting in cell discharge characteristics deviating significantly from the Pareto front. There is not one cell that performs the best across a wide range of power spectrum. The battery pack in an EV is expected to operate across a wide range of discharge scenarios as road conditions and driver throttle input varies. The requirement for both high energy density and adequate power capability results in a cell design that is non-optimal from a single-cell discharge perspective, as shown by the energy and power densities of the minimal-mass pack cell design plotted in Figure 5.1. The concave shape of the power-energy curve and the non-optimality of the pack cell design suggest that it may be advantageous to utilize cell designs that are either power-specific or energy-specific, such that they lie on the power-energy Pareto front instead of a cell design that is a compromise.

Another reason for utilizing multi-cell pack design comes about when we consider the variation of internal resistance with current and SOC. Figure 5.2 compares the total internal resistance variations of cells undergoing the UDDS federal driving cycle discharge introduced in Chapter 4. The black points are the internal resistance of the initial power-cell designs, and the green points are the internal resistance of the minimal-mass optimal cell designs. The initial cell design has much higher porosity in both electrodes, resulting in lower energy density, and hence higher battery pack mass due to lower resistance to mass transfer. However, its internal resistance is consistently lower than that of the optimal cell designs. The difference is most obvious during peak power demands, such as when SOC is approximately 0.55, where the internal resistance of the optimal cell designs are more than double of that of the initial cell designs. Calculation shows that the 1.2% of nominal energy capacity is used to overcome the internal resistance for the initial cell designs, while in the optimal designs, it is 3.8%.

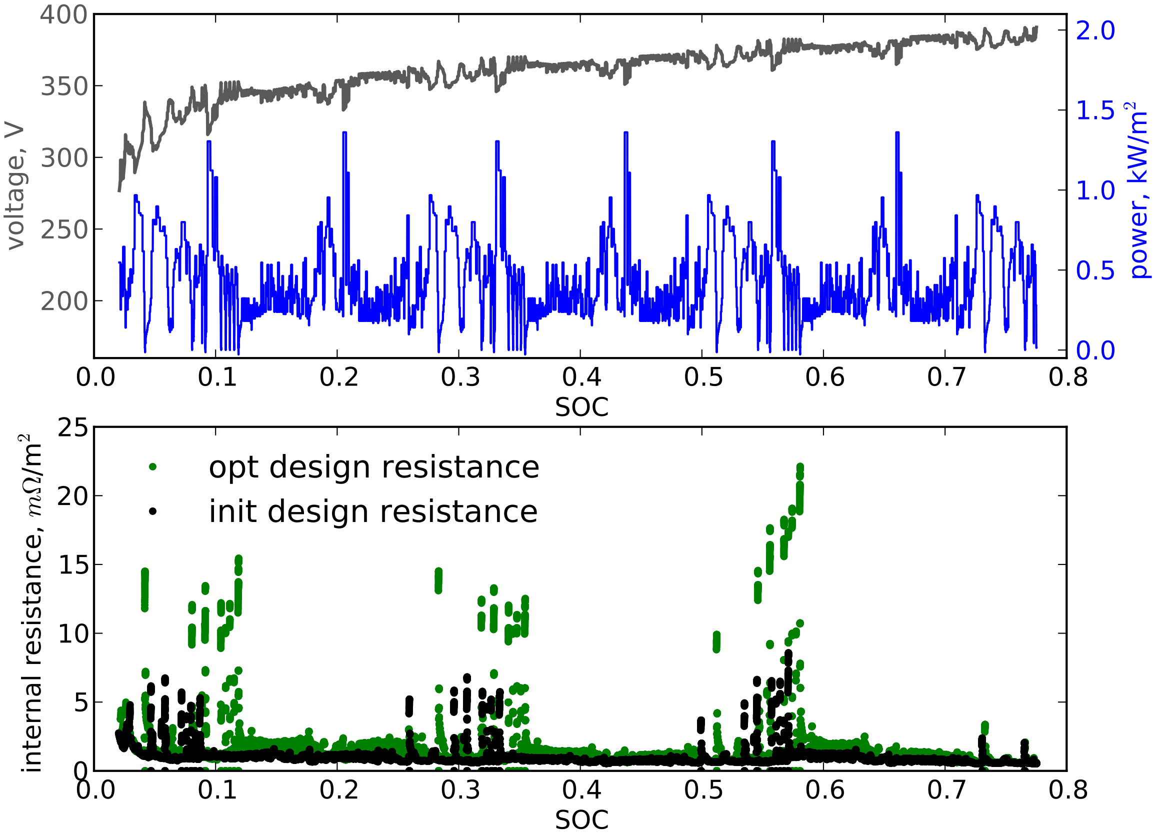

Figure 5.2: Comparison of cell internal resistance between the initial PHEV pack design and the optimized pack design

Figure 5.2 shows that while the optimally-designed uniform-cell pack is able to achieve the lowest battery pack properties—such as mass, volume, or cost—it is not the most efficient way of utilizing the stored energy capacity. It can be inferred that while the a single type of cell is optimal for a constant discharge rate, it is possible that a multi-cell design can potentially minimize energy lost to overcome internal resistance during a varied discharge scenario, such as during a typical driving cycle. The high-energy cells can be used to provide constant power at low discharge requirement, while high-power cells can be used to meet peak power demand and capture energy from regenerative braking. To fully utilize such a system, a complex control strategy that is SOC and power dependent is required.

Various multi-chemistry energy storage systems have been proposed by combining different batteries, fuel cells with lithium-ion batteries [150], or lithium-ion batteries with super-capacitors [158, 159]. The choice between batteries, fuel cells and capacitors is one between cost, energy density, power, and cycling stability. As stated in Chapter 1, lithium-ion cells have very high energy density and good power and cycling behavior; fuel cells have the highest energy density among the three but highest infrastructure cost; super-capacitors, on the other hand, have high power densities and very long cycling stability. The problem with super-capacitors, though, is that its energy density is orders of magnitude lower than that of lithium-ion battery [160]. While capacitors can supplement the instantaneous peak power, their small energy density makes them unsuitable for large battery packs, such as those required in a PHEV or EV. Most of the lithium-ion/capacitor packs that have been designed are for mild hybrid vehicles to provide moderate gain in efficiency, rather than for full-scale vehicle operation, such as in an EV. In addition, its advantage in power density has been diminished as modern purpose-built batteries are able to achieve power densities comparable to that of capacitors [161]. Having two different energy storage systems also adds to the complexity and costs of the already expensive EV architecture, as additional components—such as DC-to-AC converters—are needed to enable compatibility between the various systems.

Figure 5.1 shows that even within a single lithium-ion chemistry, altering design variables—such as electrode thickness and porosity—can produce cells with orders of magnitude more power and power density. Therefore, it is foreseeable that a battery pack with multiple battery cells of the same chemistry can be produced to satisfy the varying discharge requirements.

The research done on modeling and optimization of a single lithium-ion cell and a uniform-cell battery pack was explored in the previous two chapters. The idea of a battery pack with multiple cell designs has been previously proposed [69, 19]. However, there are no studies on establishing the designs of such multi-cell systems. Multi-cell batteries have been used in medical devices, such as pace-makers [162, 163], where a low-power circuit is used to control and monitor the device, while a second high-power output circuit delivers the electrical pulses. In this case, the power requirements of the constant-discharge low-power control circuit and pulse-discharge output circuit are known and independent of one another. Specialized cells with multiple electrodes tailored for such discharge conditions have been created and subsequently patented [164, 165].

Various research groups and companies have developed multi-cell battery systems for automobiles as well. Earlier efforts focused on developing a dual-battery system that consists of a main unit and reserve pack for emergency vehicle start [166]. This concept has been extended by Tesla to a full EV hybrid-battery pack [167], in which a second battery pack is used only when the extended range mode is selected, or the SOC of the main battery pack is critically low. General Electric demonstrated an electric bus fitted with a dual battery system in 2010 as well [168], where a high-energy density sodium battery is coupled with a high-power lithium battery to fulfill the EV performance requirement.

What has is missing is a systematic study and quantification of the advantages of such concepts over traditional uniform-cell designs. The objective of this chapter is to characterize the performance of a multi-cell battery pack design with respect to cell design parameters, and to compare that with a uniform-cell battery pack design. The conditions under which a multi-cell design is advantageous are established and the improvements of such designs are quantified as well.

5.2 Problem Formulation

In this section a new battery pack design that contains multiple cell designs is proposed. In this case, a full EV that is driven purely by electricity is considered as the baseline vehicle. The battery pack for an EV has to satisfy a minimum of two criteria, namely the energy and power requirements. Figure 5.3 illustrates a simple multi-cell battery configuration, where the energy and power requirements are fulfilled by separate high-energy density and high-power cells. To simplify subsequent computation, the power requirement is solely satisfied by the power cells, while the energy requirement is satisfied by the combined energy of both types of cells. The number of cells in series for each pack is the same, and the battery packs are connected in parallel. This configuration ensures that each battery pack has the same maximum voltage, such that the two battery packs can be used individually or together to power the EV.

To simplify the analyses in the subsequent sections, only one type of battery chemistry is considered in the multi-cell battery design. The cell designs are varied to produce cells of different power-to-energy ratio. The design variables in consideration here are the same as those listed in Table 4.1, namely: battery layout, electrode thicknesses, and electrode porosities.

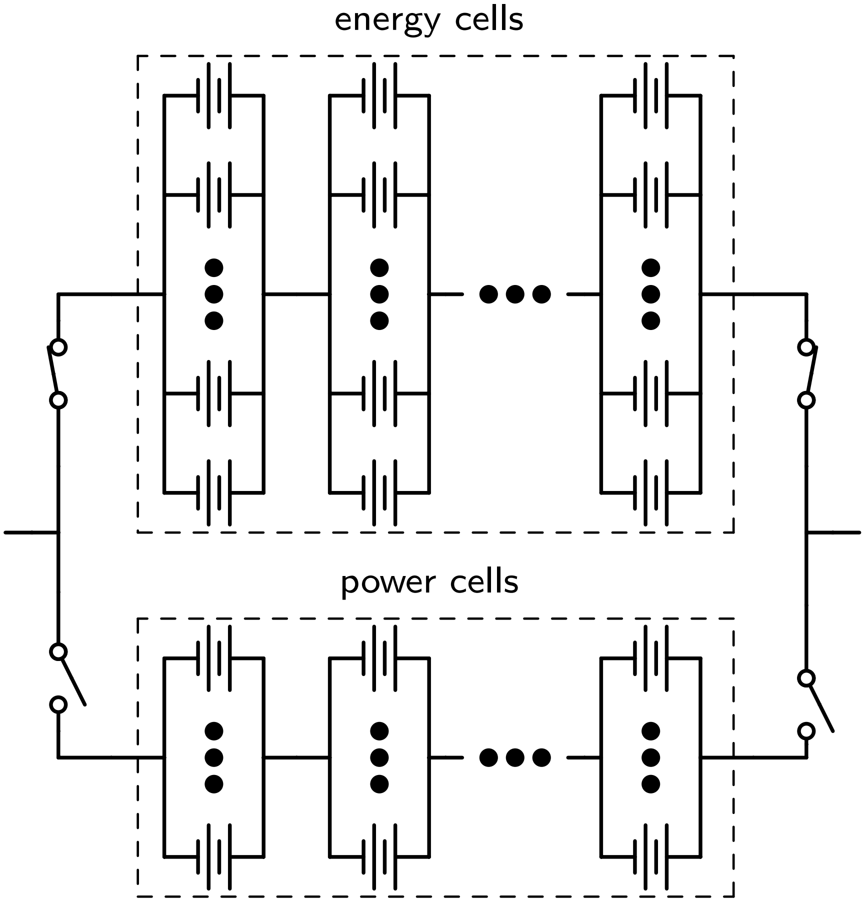

Figure 5.3: Layout of a battery pack with multiple cell designs. The power and energy packs are connected in series so as to not exceed the voltage limits of other electrical components.

5.3 Simplified Analysis

To compare the performance of a multi-cell battery pack with a uniform-cell battery pack, and to examine how the power and energy ratio of the different cells affect the battery pack properties, the equations governing the design methodology have to be derived. The battery pack is analyzed in the criterion space, where the energy and power of cells are the parameters in consideration. These parameters in turn depend on cell variables, such as those highlighted in Table 3.2, whose effects can be modeled via a cell model. For the work shown here, the mass of the battery pack is the objective that is to be minimized.

The requirement of the multi-cell battery pack follows the specifications listed Table 4.2. This is to ensure consistency in pack design for comparison. For a given battery pack with energy requirement E_{req} and power requirement P_{req}, the mass of the power cells, M_{pow}, is given by:

$$M_{pow} = \frac{P_{req}}{p} \tag{5.1}$$

where p is the maximum achievable power density of the power cells. The peak power requirement in this case is calculated from a 10-second maximum current pulse at the end of discharge. It is very unlikely that the battery will be completely drained from the 10-second pulse discharge. Any energy capacity remaining from the 10-second pulse discharge contributes towards the energy requirement. Furthermore, the maximum power attainable is dependent on how much energy is used to contribute towards the energy requirement. Hence, the power density of the power cell can be given as a function of its energy density:

$$p = \mathcal{F}(u_{pow}), \quad 0 \leq u_{pow} \leq u_{max} \tag{5.2}$$

where u_{pow} is the energy density of the power cell and u_{max} corresponds to the nominal energy density of the cell, i.e., when the power requirement is zero. Hence $u_{max} \geq u_{egy}$. The total mass of the power cells can be rewritten in terms of u_{pow}:

$$M_{pow} = \frac{P_{req}}{\mathcal{F}(u_{pow})} \tag{5.3}$$

The energy contribution of the power cells, E_{pow}, is:

$$E_{pow} = u_{pow} \cdot M_{pow} = u_{pow} \frac{P_{req}}{\mathcal{F}(u_{pow})} \tag{5.4}$$

Since the combined energy from the power and energy cells have to meet the pack requirement, the mass of the energy cells can be obtained from the additional energy required to meet the pack energy demand:

$$\begin{aligned} M_{egy} &= \tfrac{E_{req} - E_{pow}}{u_{egy}} \\ &= \tfrac{1}{u_{egy}} \left[E_{req} - u_{pow} \tfrac{P_{req}}{\mathcal{F}(u_{pow})} \right] \end{aligned} \tag{5.5}$$

Hence the mass of the battery pack can be expressed solely as a function of the energy density of the power cells as follows:

$$\begin{aligned} M_{pack} &= M_{egy} + M_{pow} \\ &= \tfrac{P_{req}}{\mathcal{F}(u_{pow})} + \tfrac{1}{u_{egy}} \left[E_{req} - u_{pow} \tfrac{P_{req}}{\mathcal{F}(u_{pow})} \right] \\ &= \tfrac{P_{req}}{\mathcal{F}(u_{pow})} \left(1 - \tfrac{u_{pow}}{u_{egy}} \right) + \tfrac{E_{req}}{u_{egy}} \end{aligned} \tag{5.6}$$

The energy cells can be assumed to undergo discharge at a constant rate that is inversely proportional to the energy capacity of the pack. There is an optimal cell design that attains the maximum energy density at that particular discharge rate. The maximum achievable energy density is assumed for the energy cells. Given that the optimal energy density is a constant for a particular discharge rate, Equation (5.6) is only a function of the power cell energy density, u_{pow}. How the battery pack mass varies with the power cell energy density in turn depends on the function $\mathcal{F}(u_{pow})$.

The value of u_{pow} for which the minimum pack mass is obtained can be calculated by taking the derivative:

$$\frac{dM_{pack}}{du_{pow}} = \frac{P_{req}}{u_{egy}\mathcal{F}(u_{pow})} \left[1 + \frac{u_{egy} - u_{pow}}{\mathcal{F}(u_{pow})} \frac{d\mathcal{F}}{du_{pow}} \right] \tag{5.7}$$

By equating the derivatives in Equation (5.7) to zero, the energy density of the power cell that gives minimum battery mass can be obtained as:

$$\frac{u_{pow} - u_{egy}}{\mathcal{F}(u_{pow})} \frac{d\mathcal{F}}{du_{pow}} = 1 \tag{5.8}$$

For a uniform-cell design, a single type of cell has to provide both the power and the energy requirements. Given the problem definition in Section 5.2, the uniform-cell design becomes a multi-cell pack design but with power cells only. Hence, the required energy density of the cell can be obtained from Equation (5.5):

$$\begin{aligned} E_{req} - u_{pow} \tfrac{P_{req}}{\mathcal{F}(u_{pow})} &= 0 \\ \Longrightarrow \tfrac{u_{pow}}{\mathcal{F}(u_{pow})} &= \tfrac{E_{req}}{P_{req}} \end{aligned} \tag{5.9}$$

The equations above allow the battery designer to examine how the performance of the cells affect the battery pack design using a reduced-order model in the criterion space, where the battery pack property is a function of power and energy density only. The design of a multi-cell pack involves judiciously selecting the right combination of power and energy cells, such that the battery pack property is optimized. The cell designs can be subsequently determined by interpolating between the optimal cell designs at the required energy and power.

5.4 Theoretical Multi-cell Battery Analysis

Equation (5.6) shows that the multi-cell battery pack mass is dependent on the energy density of the power cell as well as its power versus energy relation, which is a function of the battery's material properties and cell parameters. The analysis of battery pack mass variation can be simplified by assuming certain generic functions for $\mathcal{F}(u_{pow})$. This enables optimal battery pack mass to be derived analytically. The situations in which the multi-cell battery pack has better properties than the uniform-cell design can be readily identified as well. The dependence of maximum power density on energy density can be assumed to obey a simple power-law function of the form:

$$F(u) = a - b \cdot u^c \tag{5.10}$$

The power coefficient c is given three representative values of 0.5, 1.0, and 2.0 to simulate the power to energy functions. These values allows the analytical functions to cover a wide range of battery discharge characteristics. In addition, a quadratic function is added for comparison as well. Reasonable values for a and b that reflect realistic bounds on energy and power densities are selected to complete the functions.

Figure 5.4 plots how the battery pack mass varies with the energy density of the power cells. The energy capacity of the battery pack is 30 kWh, and the required power is 150 kW. The battery pack mass variations with different power to energy curves, and the comparison with the mass of a uniform-cell battery pack are plotted on the bottom half of Figure 5.4. For all cases, the theoretical cells are assumed to have the same maximum energy density of 210 Wh/kg and maximum power density of 10 kW/kg.

The battery pack masses for all four curves converge to the same point when the power density of the cells is maximum. This is the result of the power to energy curves having the same $y - axis$ intersection when the energy density is zero. One can also see that if the relationship between the energy and power is linear, there is no difference in battery pack mass as the energy density of the power cell is varied. Therefore, there is no advantage in terms of mass between the multi-cell and uniform-cell pack designs.

For a battery with a convex power to energy function, i.e., $\mathcal{F}(u) = a - b \cdot u^{0.5}$, the uniform-cell pack design is lighter than the multi-cell pack design. However, Figure 5.1 shows that the power to energy relations of optimal cell designs can be concave. In this

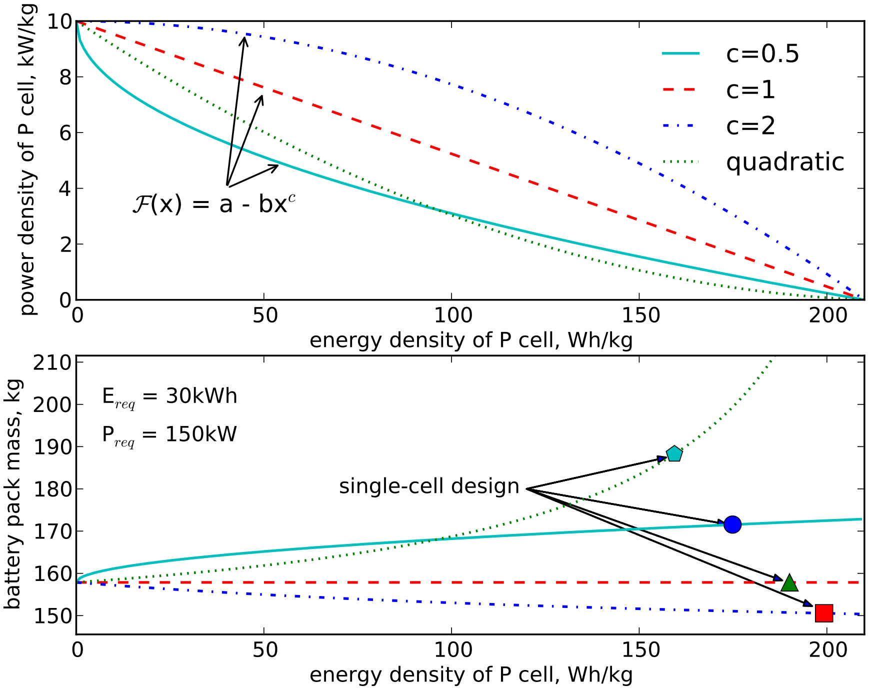

Figure 5.4: Top: variation of power density as functions of energy density. Bottom: mass for a 30kWh and 120kW battery pack as functions of energy density

case, it is more advantageous to have cell designs that are on the extreme ends of the function, such that the power and energy requirements are satisfied entirely by different types of cells. The lightest battery pack consists of energy cells and power cells with maximum power density and zero energy density.

Figure 5.4 shows the differences between of multi-cell and uniform-cell designs for a particular battery pack. The battery characteristic that favors the multi-cell pack design has been identified. To examine how the advantages vary with the battery pack specifications, a grid is used to compare battery pack masses of 6–48 kWh and 70–250 kW (Figure 5.5). The energy and power ranges encompass battery packs of a diverse group of commercially available EVs, and the subsequent analysis can be used to examine how the multi-cell design affect the battery pack mass. On the same plot, the mass of cells needed to satisfy only the energy requirement for different packs is shown. The energy-only battery mass provides the minimum bounds on the battery pack mass. As expected, the mass of energy cells increases with the pack energy requirement, and is independent of the power requirement.

The mass of the multi-cell battery pack is calculated using Equation (5.9). Analyses concentrate on the cases in which a multi-cell design outperforms a uniform-cell design. For situations when the uniform-cell design is optimal, the battery pack design simply follows the design methodology outlined in Chapter 4.

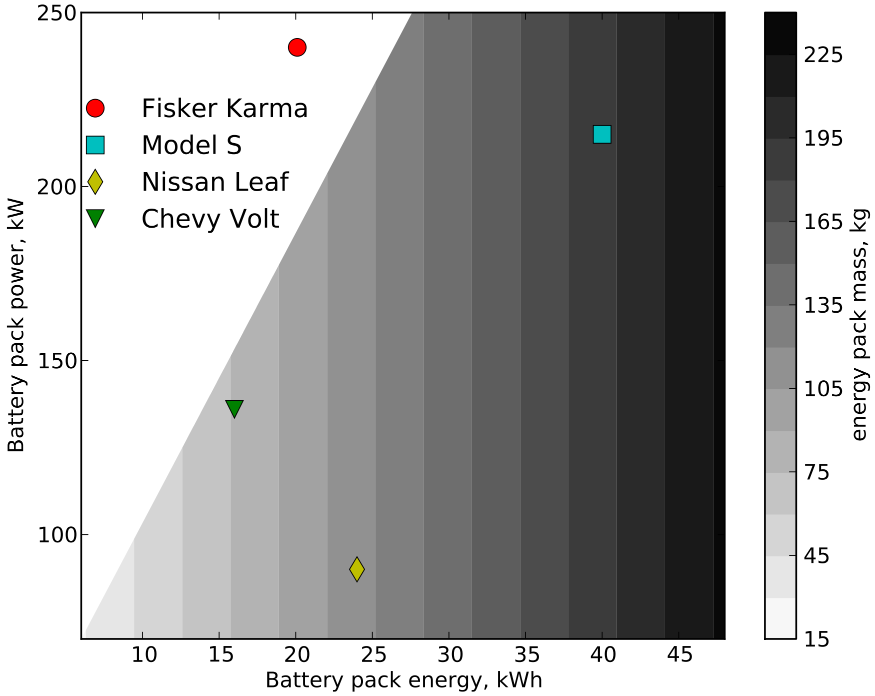

Figure 5.5: Mass of energy cells as a function of battery pack energy and power requirement. The specifications of some commercially available EV battery packs are shown as well.

Figure 5.6 shows the variation of the optimal battery pack mass when the multi-cell design approach yields the lighter battery pack. Note that there are two different power-to-energy functions for which the multi-cell approach is better, and they both result in the identical multi-cell design of maximum-power and zero-energy power cells. These results indicate that the mass is mostly a function of the energy capacity requirement. This is because the amount of cells required to satisfy the power requirement is much lower than that required for energy capacity.

The uniform-cell battery packs for the two cases when the multi-cell approach produces lighter packs are computed as well. The mass difference between multi-cell and uniform-cell designs are plotted in Figure 5.7. The quadratic power to energy relation results in a uniform-cell pack design that is heavier compared to those with power-law power-to-energy function, and thus the weight-saving advantage of the multi-cell approach is greater as well. The maximum reduction in mass is about 20% for the quadratic power-to-energy function battery, while for the concave power-law function it is about 14% .

Figure 5.7 also indicates that the fraction of mass reduction achieved using the multi-cell approach is proportional to the power-to-energy ratio of the battery pack in both scenarios. This result can be inferred from the bottom graph in Figure 5.4: As the power to

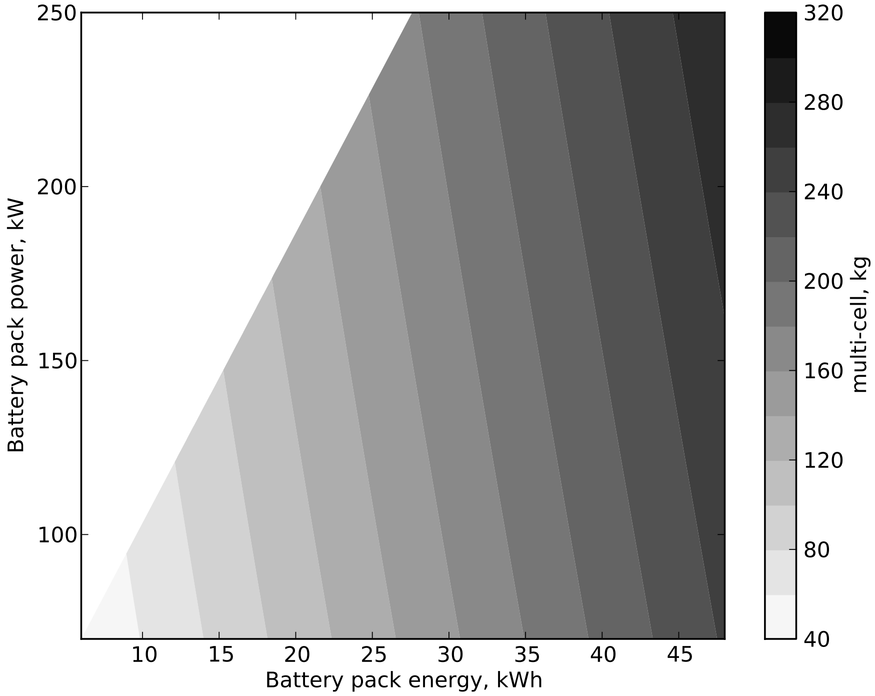

Figure 5.6: Mass of multi-cell pack designs as function of pack energy and power requirements

energy ratio increases, there is a greater compromise in the uniform-cell design to satisfy both requirement. For the multi-cell approach, increasing power at fixed energy requirement results in a linear increase in battery mass, as the only change involves stacking more power cells into the battery pack. This results in a greater mass difference between the uniform-cell and multi-cell designs. It is also worth noting that given the different shapes of the power to energy function, the advantage of using a multi-cell design at higher power-to-energy ratio is increasing at a faster rate for the quadratic power to energy function, while it is increasing at a decreasing rate for the power-law power-to-energy function.

5.5 Optimization Results

To examine how the multi-cell battery pack compares with the uniform-cell designs in reality, a lithium-ion cell with manganese spinel cathode and MCMB anode is used. The fixed properties of the cell are listed in Table 3.1. The multi-cell design process requires optimization of the individual cell designs as well as optimization of the cell combinations. Numerical optimization is performed to obtain the following:

- Maximum energy density cells at different discharge rates

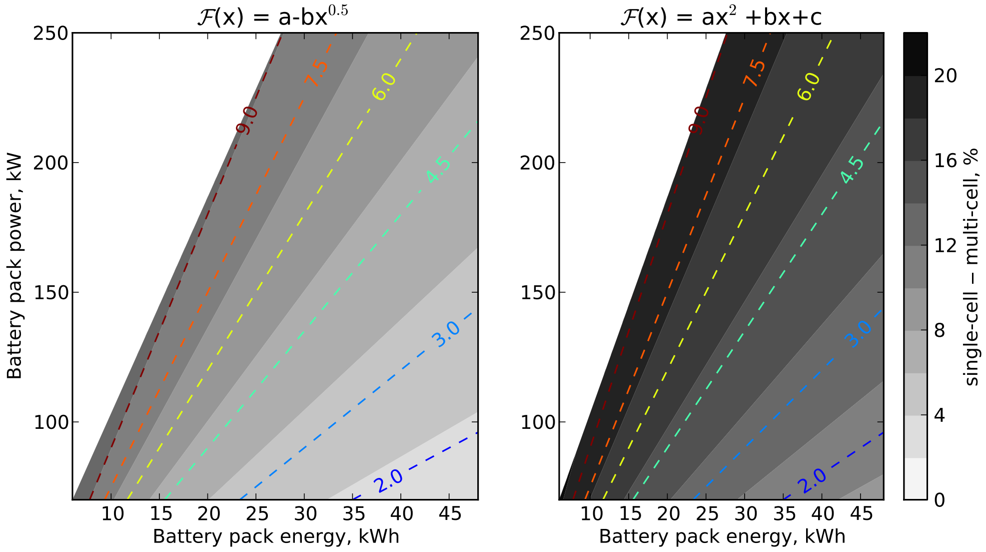

Figure 5.7: Difference between multi-cell and uniform-cell pack designs

- Minimum mass uniform-cell battery packs
- Maximum power to energy curve for the power cells by minimizing the cell mass at different power-to-energy ratios
- Minimum mass multi-cell battery packs by determining the power cell energy density that achieves optimal pack mass.

A brief explanation of each of the optimization process is provided in the following sections.

5.5.1 Energy Cell Optimization

The energy cells in a multi-cell pack are only required to meet energy capacity of the battery pack, therefore its design process is relatively straight forward. The theoretical analysis in the previous section assumes that energy cells for all battery packs have identical energy density. This is a simplification, as batteries of different energy capacity discharge at different cycling rate. Inverse proportionality is assumed between the discharge rate and battery pack energy capacity. Using the generic PHEV specifications listed in Table 4.2 as the baseline, a battery pack of 12 kWh is assumed to have a galvanostatic discharge rate of 1 C. Therefore, a 6 kWh battery pack is discharged at 2 C while a 48 kWh pack is discharged at a rate of 0.25 C. The maximum energy density is then obtained as a function of the cycling rate by using the single cell design optimization process outlined in Chapter 3. The resulting energy density as a function the cycling rate is plotted in Figure 5.8. The mass of energy cells for different battery packs can then be obtained by using the appropriate energy density for at specific cycling rates.

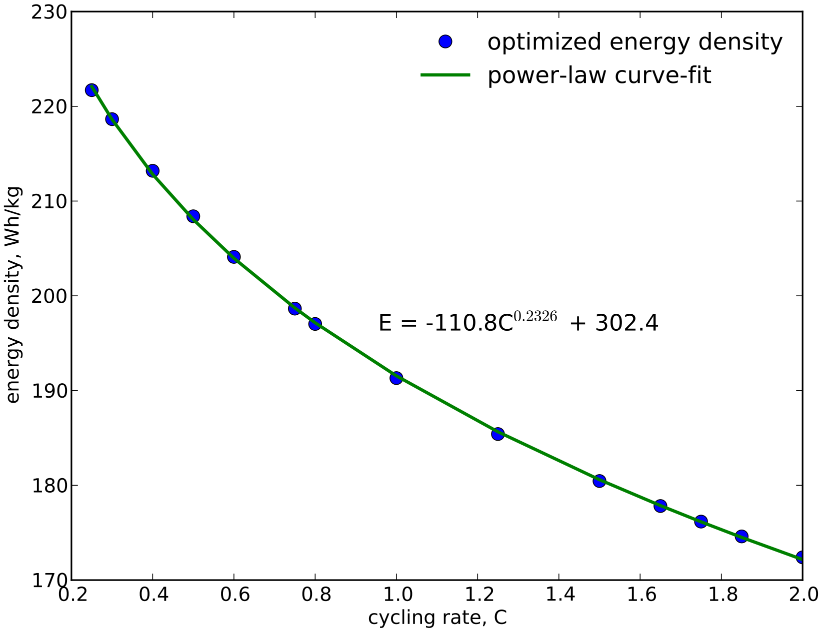

Figure 5.8: Energy density of energy cells as a function of galvanostatic cycling rate, with the power-law curve fit shown as well.

5.5.2 Uniform-cell Battery Pack Optimization

The mass of the optimal uniform-cell battery pack is obtained using the battery pack design methodology outlined in Chapter 4. The design constraints are relaxed by removing the maximum current constraints due to the variations in power requirements. While the number of cells in series is fixed at 99, the integer requirement on the number of layers is removed to obtain the best possible cell designs. The mass of the battery pack is plotted in Figure 5.9. The trends shown here are similar to those in Figure 5.12. The increase in uniform-cell battery pack mass is mostly a function of energy capacity and weakly dependent on the power requirement.

5.5.3 Power Cell Optimization

In the context of multi-cell battery design, the role of the power cells is to provide maximum amount of energy while maintaining certain end-of-discharge power output. Hence

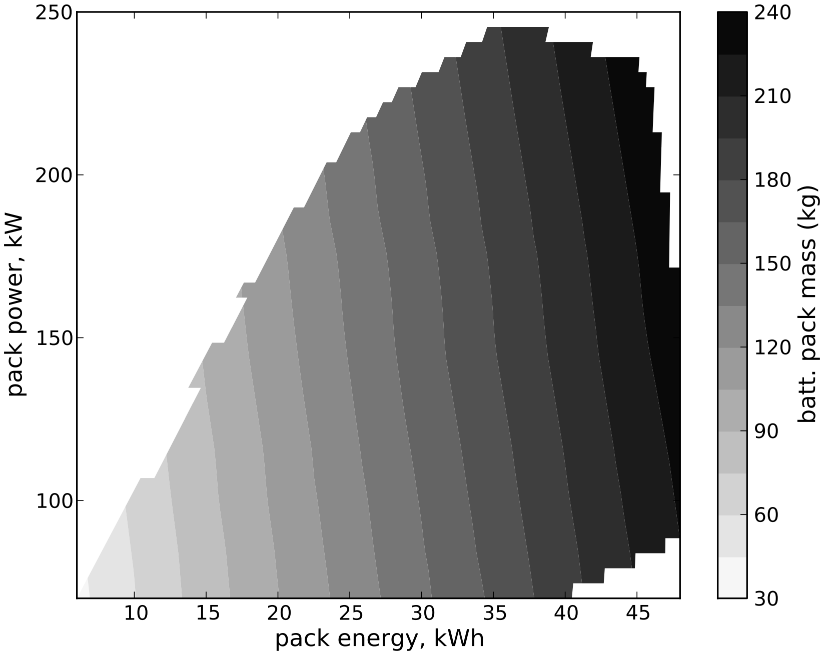

Figure 5.9: Mass of uniform-cell battery pack designs

the optimal cell designs are obtained by maximizing the energy density subject to power constraints. The power and energy discharge conditions are the same as the ones used in Chapter 4—the energy density of the cell is computed from galvanostatic discharge, while the maximum power output is the average power of the 10-second peak current pulse discharge. The resulting power versus energy curve is shown in Figure 5.10.

To examine how the power-to-energy ratio varies in the cell, the power density and energy density are plotted against the cutoff voltage at which the galvanostatic discharge rate ends and the peak power pulse current begins. The cutoff voltage is used as a proxy to estimate the fraction of charge capacity used for power or energy discharge. The resulting plot shown in the top graph of Figure 5.10 indicates that the variations of the energy and power with the cutoff voltage follow similar trend: As the cutoff voltage is increased, both the rate of energy density decrease and the rate of power density increase are accelerated. The trend shown here is more indicative of the material properties, such as the shape of the OCV curve.

A comparison between the energy and maximum power density is shown in the bottom half of Figure 5.10. The blue dots in the top graph of Figure 5.10 are all the iteration points of the optimizations, while the red circles represent the Pareto optimal points that have the best power density to energy density ratio. A best-fit curve of the Pareto optimal points is used to determine the relationship between maximum power and energy density. The

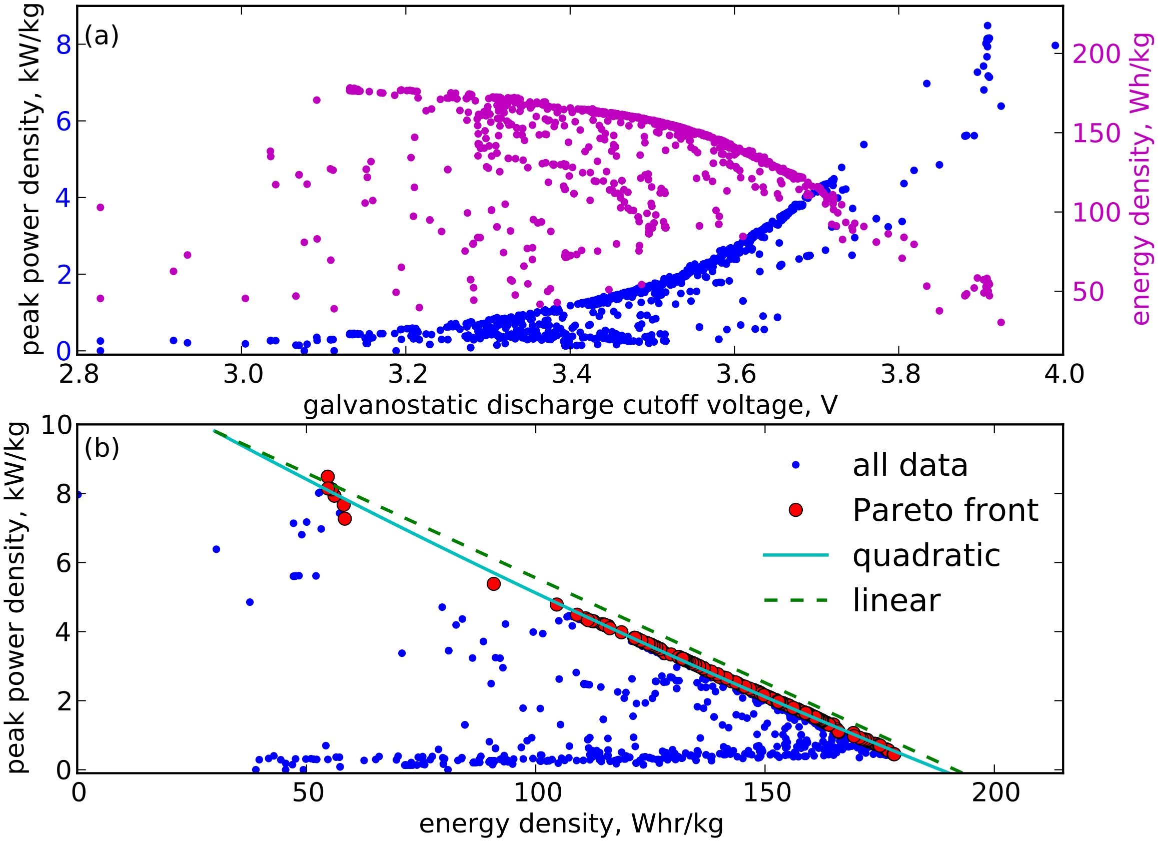

Figure 5.10: Power versus energy function of the power cells; the power to energy function is only weakly quadratic

relationship of power to energy ratio obtained from optimization is only weakly quadratic in this case. The quadratic curve fit of the Pareto front only differs slightly from the linear interpolation. The proximity of the Pareto front to a linear interpolation suggests that the improvement of multi-cell battery packs is small relative to uniform-cell battery packs.

5.5.4 Multi-cell versus Uniform-cell Optimization

The multi-cell battery pack mass can be obtained by combining the optimal energy cells and the power cells for the required energy and power capacity. Using the curve fit of power to energy relation of power cells, the power cell energy density that minimizes battery pack mass is first obtained. The energy and power cell masses can then be obtained based on the optimal power cell energy density. The difference between the uniform-cell battery pack mass and the mass of cells required to satisfy energy constraint is shown in Figure 5.11. As expected, the difference between the uniform-cell and energy-only battery pack is a function of the power requirement of the battery pack. Note that the maximum difference between the uniform-cell and energy-only battery pack mass is only about 15% for the grid of battery packs given, and thus the possible mass saving of the multi-cell battery pack is limited.

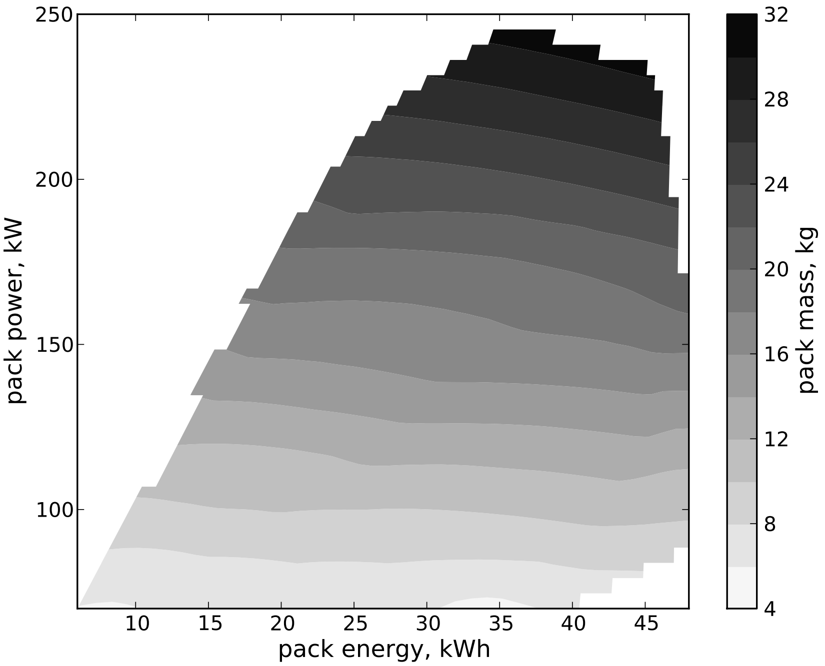

Figure 5.11: Difference between uniform-cell battery pack and pure energy cell mass

The combined energy cells and power cells form the multi-cell battery packs and the total mass as a function of pack power and energy requirement is shown in Figure 5.12. The battery mass is again mostly a function of the energy capacity, and it is only weakly dependent on the power requirement. Given the shape of the optimal power to energy density curve of the power cell (Figure 5.10), the resulting minimum-mass multi-cell battery packs consist of pure energy and pure power cells, similar to the results presented in Section 5.4.

The mass fraction of the power-cells is shown in Figure 5.13. The power-cell mass fraction increases as a function of the power-to-energy ratio of the battery pack, as more power cells are needed to satisfy the power demand at higher power-to-energy ratios. The power cells accounts for less than 15% of the total battery mass, and therefore its influence on the total battery mass is limited.

The difference between the multi-cell and uniform-cell battery pack masses obtained through cell model simulation is shown in Figure 5.14, as a percentage of the uniform-cell battery pack mass. The results show that the multi-cell battery packs are lighter than the uniform-cell battery packs, with a maximum reduction in mass of approximately 6%. This is much less than the reduction in mass shown in Section 5.4, where the maximum

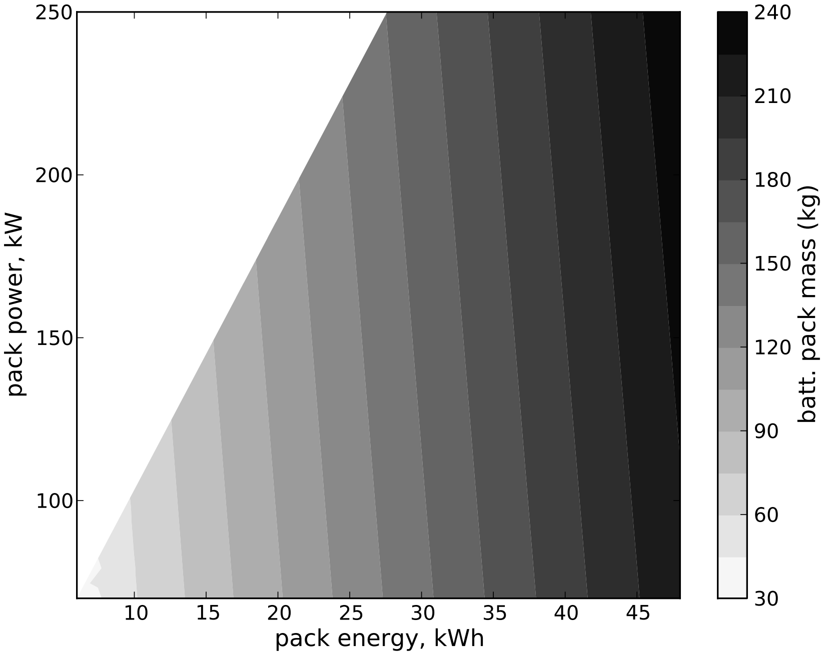

Figure 5.12: Mass of multi-cell battery pack designs

reduction in mass is close to 20%. The decreased in improvement is due to the power-to-energy curve of the power-cells. The theoretical power-to-energy curve is assumed to have a concave shape, while the actual curve obtained via optimization is more close to the linear profile. This reduces the advantages of using separate cells for different requirement.

Figure 5.14 also shows that the difference between the multi-cell and uniform-cell designs is mostly a function of the power requirement. For battery packs of low power requirement, there is little difference between the power and energy cells, regardless of the pack energy capacity. The difference increases steadily as the pack power requirement increases. This is in contrast with the results shown in Figure 5.7, where the mass difference is a function of the power-to-energy ratio of the battery pack.

5.5.5 Practical Design Considerations

The results shown in the previous sections indicate that the optimal multi-cell pack design consists of power-cells with maximum power density and zero energy density. In another words, the power-cells are expected to completely discharge within 10 seconds. Such cells have minimal thickness and high porosity to satisfy the high mass transfer rate due to the peak current demand. However, their energy capacity is extremely limited. Given that each current pulse is a deep discharge for the cell, the cells will be undergoing multiple

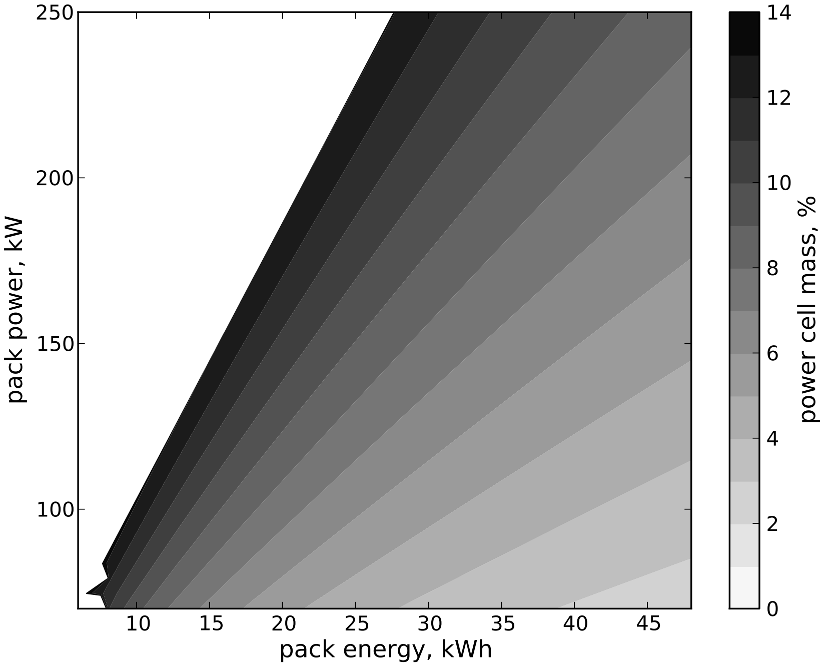

Figure 5.13: Fraction of pack mass that is power cell

charge and discharge cycles within a typical drive cycle in order to meet the power peaks. Such discharge behavior is likely to cause rapid degradation of the cells, thus negating any weight-saving advantages in the battery pack design.

Hence, it is more practical to design a multi-cell battery pack requiring power-cells to have some minimal energy capacities for practical considerations. In the following analysis, the energy density of the power-cells is limited to a minimum of 50 Wh/kg. The battery pack energy requirement are satisfied by both energy and power cells. Figure 5.15 shows that the resulting battery packs are still lighter than the uniform-cell packs, but that the weight reduction is diminished.

5.6 Summary

A new multi-cell battery pack design approach is explored in this chapter. Current EV battery packs utilize a single type of cells to meet both power and energy requirements of vehicle operations. While multi-cell or multi-chemistry energy storage systems have been explored by various other authors, there still lacks a systematic study of the possible benefits of such battery pack design. The objective of this chapter is to derive simplified equations to analyze the performance of such batteries and to compare the multi-cell with the uniform-cell battery packs.

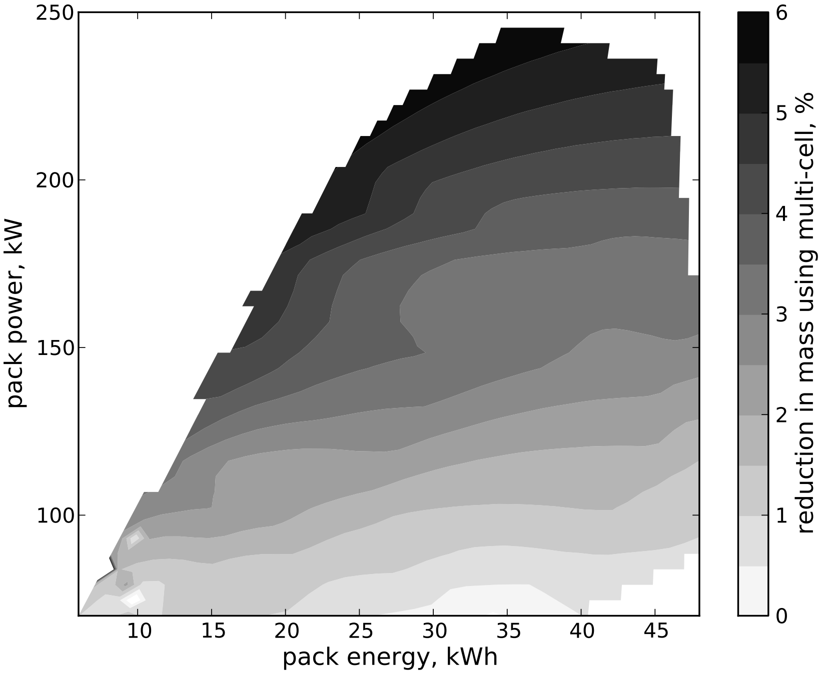

Figure 5.14: Difference between uniform-cell and multi-cell battery pack mass

The multi-cell design separates the battery pack into power and energy cells, where each cell type is responsible for a particular constraint. It is shown that the multi-cell design approach depends on the power-to-energy relation of the cells in use. When the power-to-energy function has a concave shape, the multi-cell design is more advantageous than the uniform-cell approach. Multi-cell battery pack designs with manganese spinel-MCMB lithium-ion cells are demonstrated, and they are found to be up to 6% lighter than the uniform-cell pack designs.

There are practical hurdles to be overcome before the implementation of such pack designs is feasible. While the multi-cell design may lead to better battery properties in terms of mass or volume, its cost is likely to increase as multiple type of cells are installed within the same battery pack, thereby increasing material and manufacturing cost. In addition, using separate power and energy cells also lead to the possibility of completely discharging the power cells before the energy cells are discharged. This leads to the EV being unable to meet the power demand at low SOC, or to the power-cells requiring onboard charging via the energy-cells or via a second energy source. However, the multi-cell concept can be advantageous in the long run, as more specialized batteries are produced for various applications. In this chapter, the multi-cell design consists of a single type of lithium-ion chemistry with varying electrode designs to achieve different power to energy ratios. The multi-cell concept can be readily extended to different lithium-ion chemistries such that the

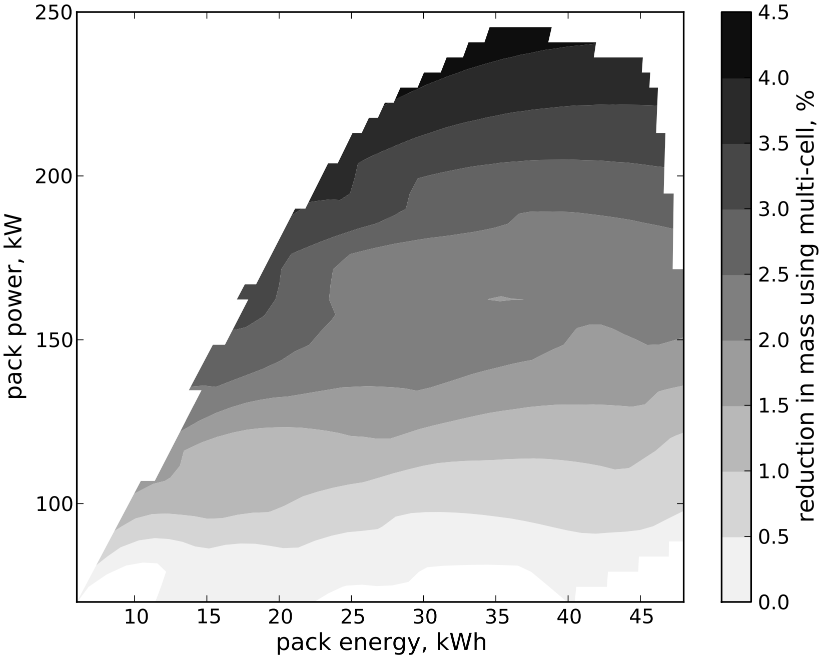

Figure 5.15: Difference between uniform-cell and multi-cell battery pack mass with minimum 50 Wh/kg energy density

optimal battery pack design consists of different cells for different discharge rate or cycling stability.

CHAPTER 6

Conclusions and Recommendations

6.1 Concluding Summary

This dissertation is a numerical optimization study directed towards the improvement of battery designs. The objectives are to develop numerical frameworks that can automate the optimization of battery designs for practical applications. The optimal solutions can provide guidelines and devise new strategies to further enhance battery performance. Three battery design problems were discussed in this work. Chapter 3 analyzes the optimization of a single lithium-ion cell with respect to the electrode morphological parameters, as well as the transport properties. The objective is to maximize the gravimetric energy density, and to quantify the effects of various parameters on energy density. Chapter 4 extends the framework to the more practical problem of the design of a PHEV battery pack. The objective is to minimize the battery pack mass, volume and cost. Chapter 5 then combines the design frameworks in the previous two chapters and explores the possibility of a multi-cell design approach in battery pack design. The summary of the contributions and findings are briefly recounted here.

A numerical framework coupling a detailed electrochemistry model with an optimizer is able to efficiently determine the optimal cell designs suitable for various applications. A complete design that includes all relevant parameters is considered in Chapter 3, where the objective is to maximize the gravimetric energy density of a single lithium-ion cell subject to constrained power. For an ideal lithium-ion cell, the electrode particles should be as small as possible to minimize diffusion-related overpotential, while the bulk transport parameters need to be as large as possible. However, its relative effects EW diminished for the optimal designs, as the small particle sizes significantly reduced the characteristic diffusion time. The resulting cell is not diffusion limited in the solid phase. The optimization results also enables the quantification of the decrease in thickness and increase in porosity as the power requirement increases. The mathematical relation between the optimal electrode parameters can be computed via the active mass ratio, and it is found to be almost constant for all power constraints.

A battery pack designed for PHEV operation requires consideration of separate energy and power constraints. Additional voltage and current limits have to be taken into account as well. A hybrid optimization scheme utilizing both gradient-free and gradient-based optimizers is used to tackle the pack design problem. This simplifies the design process by considering multiple design constraints simultaneously. The optimization algorithm is applied to minimize the mass, volume and cost for a generic PHEV battery pack. The optimized designs have battery pack properties that are superior to *ad hoc* designs that follow general guidelines. They can sustain longer all-electric driving ranges when subject to federal drive cycle discharge simulations as well. An optimized battery pack provides realistic bounds on the possible configurations for a given battery chemistry, and gives the best possible starting points in a battery design cycle.

Given that the discharge of a cell at any off-design condition results in rapid loss of either power or energy density away from the Pareto front, the optimal battery pack cells obtained in Chapter 4 are a compromise between power and energy at different discharge rates. A new design approach that uses multiple cells to satisfy power and energy requirements separately is explored. It is more favorable to utilize the multi-cell approach for cells with concave power-to-energy relations. By utilizing cells at the extreme ends of the power to energy function, the multi-cell battery is shown to be lighter than the single-cell pack designs.

The methods and results presented in this dissertation provide contributions towards battery and EV system design process. Single cell optimization quantifies the optimal electrode parameters and sets guidelines in dealing with the interactions between various design variables. The PHEV pack design methodology provides an efficient tool for estimating the best cell designs and battery layout to meet vehicle requirement. Minimization with respect to different objective function shows the importance of an objective-oriented process to achieve the best possible design for particular function. Finally, the multi-cell approach demonstrates how a more complex optimization process can be used to further advance the design of battery packs.

6.2 Realistic Cell Considerations

For all three design problems shown here, the cell model assumes an ideal electrochemical cell and ignores any cell degradation mechanisms that may result from any extreme cell designs. These mechanisms are important when considering the overall life cycle performance. While some of the capacity fade reactions have been discussed throughout the dissertation, they are treated more systematically in this section. Phenomena not considered in the current cell model that may be important for other types of battery cells are discussed here as well. These processes may be discussed independently, but they are tightly coupled and do not occur separately from each other.

For cell designs that include aging mechanisms, the evaluation of the cell performance with respect to one discharge cycle would be insufficient. A cell design that has maximum initial energy density or performance only to suffer catastrophic capacity loss or power fade within a small number of cycles would be a poor design. Additional constraints that set lower bounds on the end-of-life energy density or modifications to the objective function that accounts for cumulative useful energy over the entire lifetime should be included.

6.2.1 Volume Change in Solid Phase

Volume fraction change in the graphite anode and manganese spinel cathode is small and is neglected in the cell model, however it is not the case for some of the other materials, such as silicon in anodes. Volume change up to factors of 3–4 can be expected during intercalation. The large volume increase means that the ion transport equation in the solid phase cannot be simplified to the diffusion equation (2.3).

Volume change in the electrode affects the cell performance in several ways. First, volume change causes change in porosity. Reduction in porosity during intercalation increases cell impedance, leading to loss of power. The effects of porosity change is further enhanced at high cycling rates. Drastic volume change can also cause contact loss of active material particles, resulting in capacity fade due to loss of cyclable lithium and available intercalation sites [169].

Accounting for the effects of volume expansion in the cell model requires coupling of a physics-based degradation model to determine how design variables, such as particle size and volume fraction, contribute to contact loss. Factors such as particle packing density and size influence the effect of volume change [170] and need to be considered as well. Significant change in porosity requires modeling the porosity as a dynamic parameter that changes with the current density and direction.

6.2.2 Modeling of Additives

The solid matrix in the electrode is made up of active material, conduction additives, and polymer binders that hold everything in place. Therefore, the actual properties of the solid material are functions of the solid matrix composition, and not constant in a homogeneous electrode. The solid conductivity, for instance, depends on the interaction between the carbon additives and the active material, which is a function of both active material particle size, and carbon additives to active material mass ratio [143]. Larger active material particles exert greater attraction forces on the carbon additives, while a higher mass fraction increases the probability of additives attaching the active material.

Instead of treating conductivity as an independent variable whose effect is only modified by the porosity, conductivity can be modeled as a function the solid phase composition, where the mass fraction of active material, polymer binder, and carbon additives are the independent variables. The cell optimization problem then becomes a balance between maximizing the amount of energy-contributing energy material, the need to maintain sufficient electronic conductivity using additives and to reduce concentration polarization by ensuring adequate porosity in the electrode.

6.2.3 Solid-Electrolyte Interface Formation

One of the primary causes of lithium loss in the cell is the decomposition of electrolyte at the negative electrode/electrolyte interface to form a passivated SEI layer during the initial cycles [169]. This is due to the anode operating at voltages that are outside the electrochemical stability window of electrolyte components. SEI formation is an irreversible process that consumes cyclable lithium. However the SEI layer is also beneficial in preventing further decomposition of solvent and at the same time allows lithium ions to pass through.

Ideally, a good cell design should encourage an SEI layer that is both chemically and mechanically stable. The latter is especially important for electrodes experiencing large volume change during cycling. To accurately model the formation, growth and subsequent stabilization of SEI layer, physics-based interaction between electrode active material and electrolyte and influence of SEI thickness on electrolyte diffusivity should be included in the cell model [171]. Electrode design also has to take lithium loss due to SEI layer into account when determining the optimal mass ratio.

6.2.4 Intercalation-Induced Stress

Factors such as volume change and SEI formation all affect the intercalation-induced stress experienced by the solid particles. The amount of stress depends on the shape and size of particles, and it is interrelated through the local surface flux, and ion concentration gradient [56]. Multi-scale modeling has shown that lithium intercalation for large particles is diffusion limited and that the resulting diffusion-stress coupling causes mismatching strains and stresses [116]. High stress is also experienced in nanoscale particles due to surface stress effect [172].

Stress and particle fracture inclusion in the cell design process requires modeling of local material and transport properties, such as local particle geometry and flux density. Simulation of the entire cell at the particle level requires three-dimensional modeling of all electrode particles to replace the Butler–Volmer equation.

6.3 Recommendations for Future Work

The main focus of this dissertation was to maximize the gravimetric energy density of lithium-ion cells, and to improve battery pack designs using numerical optimization. The homogeneous electrode treatment and the lack of cell degradation considerations highlighted in the previous section limit the scope of the dissertation. Several aspects can be undertaken to expand on the existing framework to improve the practical impact of the optimization results.

First, detailed micro-structure modeling can be incorporated into the cell model to provide high-fidelity cell design optimization. It has been shown that there is discrepancy between the effective transport coefficients and the estimates using Bruggeman's relation [173], and porosity alone cannot fully account for the variations in the effective transport coefficients in a porous material [174]. A second parameter, such as tortuosity, may be required to provide more accurate predictions of the material properties.

To account for effects of microscale geometries on cell performance, a multi-scale cell model is needed. However, the transient microscale simulation of the entire cell can be prohibitively expensive for optimization purposes. A surrogate multi-scale approach can be applied to provide microscale information to the cell-level model [174]. A response surface is generated using a large number of microscale simulations in a representative elementary volume. In this case different particle geometries and orientations have to be considered and statistical analysis can be used to quantify their effects on the local mass transfer rate within the electrode. Subsequent computations at the cell level will be based on the metamodel that is much faster to execute.

A more complete way to perform multi-cell battery pack optimization than the one presented in Chapter 5 is to couple the electrode design parameters, battery layout, and control variables that determine the optimal discharge profiles for different cells. Sequential optimization of the battery pack design followed by an optimal control strategy often leads to non-optimal overall systems as the coupling between the battery pack design and control parameters is not captured. Therefore, simultaneous optimization of the various disciplines in a multidisciplinary optimization framework is required to obtain the true optimal system design. Such formulation would also remove the necessity of having fixed energy and power capacities as the constraints and simply focus on maximizing the electric driving ranges of the battery pack. To prevent the optimal battery pack from becoming tailored for a particular driving cycle, an aggregate objective function could be used to determine a multi-point optimal design, such that the optimal solution is one that performs the best across the different driving cycles.

BIBLIOGRAPHY

[1] IEA. *Key World Energy Statistics 2010*. OECD/IEA, 2010.

[2] IATA. IATA economic briefing: Airline fuel and labour cost share, February 2010. URL: `http://www.iata.org/whatwedo/Documents/economics/Airline_Labour_Cost_Share_Feb2010.pdf`.

[3] Andrew B. Lambe and Joaquim R. R. A. Martins. Extensions to the design structure matrix for the description of multidisciplinary design, analysis, and optimization processes. *Structural and Multidisciplinary Optimization*, 46:273–284, August 2012. `doi:10.1007/s00158-012-0763-y`.

[4] Michigan Public Service Commission. Comparisons of average rates (in cents per kwh) for MPSC-regulated electric utilities in michigan, October 2013. URL: `www.dleg.state.mi.us/mpsc/electric/download/rates1.pdf`.

[5] Chris Brady. *The Boeing 737 Technical Guide*. Tech Pilot Services, 2012.

[6] The CAFE Foundation. The 2011 Green Flight Challenge sponsored by Google, 2011. URL: `cafefoundation.org/v2/gfc_2011_results.html`.

[7] Tine Tomažič, Vid Plevnik, Gregor Veble, Jure Tomažič, Franc Popit, Sašo Kolar, Radivoj Kikelj, Jacob W Langelaan, and Kirk Miles. Pipistrel taurus G4: on creation and evolution of the winning aeroplane of NASA Green Flight Challenge 2011. *Strojniški vestnik-Journal of Mechanical Engineering*, 57(12):869–878, 2011.

[8] Marzieh Barghamadi, Ajay Kapoor, and Cuie Wen. A review on Li-S batteries as a high efficiency rechargeable lithium battery. *Journal of The Electrochemical Society*, 160(8):A1256–A1263, 2013.

[9] Myounggu Park, Xiangchun Zhang, Myoungdo Chung, Gregory B Less, and Ann Marie Sastry. A review of conduction phenomena in Li-ion batteries. *Journal of Power Sources*, 195(24):7904–7929, 2010.

[10] EIA. Annual energy review. *Energy Information Administration, US Department of Energy: Washington, DC*, 2011. URL: `www.eia.doe.gov/emeu/aer`.

[11] EIA. Inventory of U.S. greenhouse gas emissions and sinks: 1990 – 2011. *U.S. Environmental Protection Agency, Washington, DC*, 2013. URL: `www.epa.gov/climatechange/ghgemissions/usinventoryreport.html`.

[12] IATA. Vision 2050: Shaping aviations future.

[13] IATA. Financial forecast: Losses expected to continue into 2010, September 2009. URL: `www.iata.org/publications/economics/Documents/Industry_Outlook_Sep09.pdf`.

[14] IATA. Financial forecast - prospects for 2014 look good (in parts), September 2013. URL: `www.iata.org/whatwedo/Documents/economics/iata-economic-briefing-financial-forecast-september-2013.pdf`.

[15] Joyce E Penner. *Aviation and the Global Atmosphere: Special Report of the IPCC Working Groups I and III in Collaboration with the Scientific Assessment Panel to the Montreal Protocol on Substances that Deplete the Ozone Layer*. Cambridge University Press, 1999.

[16] EIA. Monthly energy review september 2013. *U.S. Energy Information Administration*, 2013. URL: `http://www.eia.gov/totalenergy/data/monthly/pdf/sec7_5.pdf`.

[17] Don Anair and Amine Mahmassani. State of charge: Electric vehicles global warming emissions and fuel-cost savings across the united states. Technical report, June 2012.

[18] Michel Armand and J-M Tarascon. Building better batteries. *Nature*, 451(7179):652–657, 2008.

[19] James Larminie and John Lowry. *Electric vehicle technology explained*. Wiley Online Library, 2012.

[20] John M German. *Hybrid powered vehicles*. SAE International, 2003.

[21] Andreas Dinger, Ripley Martin, Xavier Mosquet, Maximilian Rabl, Dimitrios Rizoulis, Massimo Russo, and Georg Sticher. Batteries for electric cars: Challenges, opportunities, and the outlook to 2020. *Boston Consulting Group*, 2010.

[22] Alphonsus L Drum. Electrically-propelled aircraft, 1924.

[23] James L Felder, Hyun Dae Kim, and Gerald Brown. Turboelectric distributed propulsion engine cycle analysis for hybrid-wing-body aircraft. In *47th AIAA Aerospace Sciences Meeting*, number 2009-1132. AIAA, 2009.

[24] A Gibson, David Hall, Mark Waters, P Masson, B Schiltgen, and T Foster. The potential and challenge of turboelectric propulsion for subsonic transport aircraft. *AIAA*, 276:2010, 2010.

[25] Amir S Gohardani, Georgios Doulgeris, and Riti Singh. Challenges of future aircraft propulsion: a review of distributed propulsion technology and its potential application for the all electric commercial aircraft. *Progress in Aerospace Sciences*, 47(5):369–391, 2011.

[26] Rhea P. Liem and Joaquim R. R. A. Martins. Multifidelity aerostructural optimization of a long-range aircraft configuration with uncertain missions and operating conditions. In *Proceedings of the 54th AIAA/ASME/ASCE/AHS/ASC Structures, Structural Dynamics, and Materials Conference*, Boston, MA, April 2013.

[27] Cesar A Luongo, Philippe J Masson, Taewoo Nam, Dimitri Mavris, Hyun D Kim, Gerald V Brown, Mark Waters, and David Hall. Next generation more-electric aircraft: a potential application for hts superconductors. *Applied Superconductivity, IEEE Transactions on*, 19(3):1055–1068, 2009.

[28] JA Rosero, JA Ortega, E Aldabas, and LARL Romeral. Moving towards a more electric aircraft. *Aerospace and Electronic Systems Magazine, IEEE*, 22(3):3–9, 2007.

[29] Marty K Bradley and Christopher K Droney. Subsonic ultra green aircraft research: Phase I final report. 2011.

[30] Hyun Dae Kim. Distributed propulsion vehicles. In *27th International Congress of the Aeronautical Sciences*, 2010.

[31] Siemens. World's first serial hybrid electric aircraft to fly at Le Bourget, 2011. URL: `http://www.siemens.com/press/pool/de/pressemitteilungen/2011/corporate_communication/AXX20110666e.pdf`.

[32] Jason Paur. Hybrid power comes to aviation, July 2009. URL: `www.wired.com/autopia/2009/07/hybrid-aviation`.

[33] Yuneec. Yuneec E430 electric aircraft specifications, 2013. URL: `yuneeccouk.site.securepod.com/Aircraft_specification.html`.

[34] Yuri Gawdiak, Bruce J Holmes, Bruce K Sawhill, James Herriot, David Ballard, Jeremy Eckhause, Dou Long, Robert Hemm, Jeremiah Creedon, Charles Murphy, Terry Thompson, Fred Wieland, Mike Marcolini, Mark Moore, and Monica Alcabin. Air transportation strategic trade space modeling and assessment through analysis of on-demand air mobility with electric aircraft. In *12th AIAA Aviation Technology, Integration, and Operations (ATIO) Conference and 14th AIAA/ISSM*. AIAA.

[35] Mark D Moore. Concept of operations for highly autonomous electric zip aviation. *12th AIAA Aviation Technology, Integration, and Operations (ATIO) Conference and 14th AIAA/ISSM*, (AIAA 2012-5472), 2012.

[36] Michael D Patterson, Brian J German, and Mark D Moore. Performance analysis and design of on-demand electric aircraft concepts. In *12th AIAA Aviation Technology, Integration, and Operations (ATIO) Conference and 14th AIAA/ISSM*, number AIAA 2012-5474. AIAA, 2012.

[37] Darryll J Pines and Felipe Bohorquez. Challenges facing future micro-air-vehicle development. *Journal of aircraft*, 43(2):290–305, 2006.

[38] Ohad Gur and Aviv Rosen. Optimizing electric propulsion systems for unmanned aerial vehicles. *Journal of aircraft*, 46(4):1340–1353, 2009.

[39] Frederick G Harmon, Andrew A Frank, and Jean-Jacques Chattot. Conceptual design and simulation of a small hybrid-electric unmanned aerial vehicle. *Journal of aircraft*, 43(5):1490–1498, 2006.

[40] Mirac Aksugur and Gokhan Inalhan. Design methodology of a hybrid propulsion driven electric powered miniature tailsitter unmanned aerial vehicle. *Journal of Intelligent and Robotic Systems*, 57(1-4):505–529, 2010.

[41] JY Hung and LF Gonzalez. On parallel hybrid-electric propulsion system for unmanned aerial vehicles. *Progress in Aerospace Sciences*, 51:1–17, 2012.

[42] Joaquim R. R. A. Martins and Andrew B. Lambe. Multidisciplinary design optimization: A survey of architectures. *AIAA Journal*, 51(9):2049–2075, Sep 2013. `doi:10.2514/1.J051895`.

[43] Ping Liu, Elena Sherman, and Alan Jacobsen. Design and fabrication of multifunctional structural batteries. *Journal of Power Sources*, 189(1):646–650, 2009.

[44] James P Thomas and Muhammad A Qidwai. The design and application of multifunctional structure-battery materials systems. *JOM Journal of the Minerals, Metals and Materials Society*, 57(3):18–24, 2005.

[45] Ronald F Gibson. A review of recent research on mechanics of multifunctional composite materials and structures. *Composite structures*, 92(12):2793–2810, 2010.

[46] K David Huang and Sheng-Chung Tzeng. Development of a hybrid pneumatic-power vehicle. *Applied Energy*, 80(1):47–59, 2005.

[47] Dong Zhang, Branko N Popov, and Ralph E White. Modeling lithium intercalation of a single spinel particle under potentiodynamic control. *Journal of The Electrochemical Society*, 147(3):831–838, 2000.

[48] Gang Ning and Branko N Popov. Cycle life modeling of lithium-ion batteries. *Journal of The Electrochemical Society*, 151(10):A1584–A1591, 2004.

[49] Bor Yann Liaw, Ganesan Nagasubramanian, Rudolph G Jungst, and Daniel H Doughty. Modeling of lithium ion cells - a simple equivalent-circuit model approach. *Solid state ionics*, 175(1):835–839, 2004.

[50] Matthieu Dubarry, Nicolas Vuillaume, and Bor Yann Liaw. From single cell model to battery pack simulation for Li-ion batteries. *Journal of Power Sources*, 186(2):500–507, 2009.

[51] BS Bhangu, P Bentley, DA Stone, and CM Bingham. Nonlinear observers for predicting state-of-charge and state-of-health of lead-acid batteries for hybrid-electric vehicles. *Vehicular Technology, IEEE Transactions on*, 54(3):783–794, 2005.

[52] Marc Doyle, Thomas F Fuller, and John Newman. Modeling of galvanostatic charge and discharge of the lithium/polymer/insertion cell. *Journal of the Electrochemical Society*, 140(6):1526–1533, 1993.

[53] John Newman and Karen E Thomas-Alyea. *Electrochemical systems*. Wiley-Interscience, 2004.

[54] Shriram Santhanagopalan, Qingzhi Guo, Premanand Ramadass, and Ralph E White. Review of models for predicting the cycling performance of lithium ion batteries. *Journal of Power Sources*, 156(2):620–628, 2006.

[55] CY Wang, WB Gu, and BY Liaw. Micro-macroscopic coupled modeling of batteries and fuel cells i. model development. *Journal of The Electrochemical Society*, 145(10):3407–3417, 1998.

[56] Xiangchun Zhang, Wei Shyy, and Ann Marie Sastry. Numerical simulation of intercalation-induced stress in Li-ion battery electrode particles. *Journal of the Electrochemical Society*, 154(10):A910–A916, 2007.

[57] Amit Gupta, Jeong Hun Seo, Xiangchun Zhang, Wenbo Du, Ann Marie Sastry, and Wei Shyy. Effective transport properties of $LiMn_2O_4$ electrode via particle-scale modeling. *Journal of The Electrochemical Society*, 158(5):A487–A497, 2011.

[58] Pankaj Arora, Ralph E White, and Marc Doyle. Capacity fade mechanisms and side reactions in lithium-ion batteries. *Journal of the Electrochemical Society*, 145(10):3647–3667, 1998.

[59] P Ramadass, Bala Haran, Parthasarathy M Gomadam, Ralph White, and Branko N Popov. Development of first principles capacity fade model for Li-ion cells. *Journal of the Electrochemical Society*, 151(2):A196–A203, 2004.

[60] John Christensen and John Newman. Stress generation and fracture in lithium insertion materials. *Journal of Solid State Electrochemistry*, 10(5):293–319, 2006.

[61] Jonghyun Park, Jeong Hun Seo, Gregory Plett, Wei Lu, and Ann Marie Sastry. Numerical simulation of the effect of the dissolution of $LiMn_2O_4$ particles on Li-ion battery performance. *Electrochemical and Solid-State Letters*, 14(2):A14–A18, 2011.

[62] Bor Yann Liaw, Rudolph G Jungst, Ganesan Nagasubramanian, Herbert L Case, and Daniel H Doughty. Modeling capacity fade in lithium-ion cells. *Journal of Power Sources*, 140(1):157–161, 2005.

[63] Steve Siler. Pump it up: We refuel a hydrogen fuel-cell vehicle, November 2008. URL: `www.caranddriver.com/features/pump-it-up-we-refuel-a-hydrogen-fuel-cell-vehicle`.

[64] William M Haynes, David R Lide, and Thomas J Bruno. *CRC Handbook of Chemistry and Physics 2012-2013*. CRC press, 2012.

[65] M Stanley Whittingham. Electrical energy storage and intercalation chemistry. *Science*, 192(4244):1126–1127, 1976.

[66] DW Murphy, FJ Di Salvo, JN Carides, and JV Waszczak. Topochemical reactions of rutile related structures with lithium. *Materials Research Bulletin*, 13(12):1395–1402, 1978.

[67] K Mizushima, PC Jones, PJ Wiseman, and JB Goodenough. Li$_x$CoO$_2$(0¡ x¡-1): A new cathode material for batteries of high energy density. *Materials Research Bulletin*, 15(6):783–789, 1980.

[68] MM Thackeray, WIF David, PG Bruce, and JB Goodenough. Lithium insertion into manganese spinels. *Materials Research Bulletin*, 18(4):461–472, 1983.

[69] David Linden and Thomas B Reddy. *Handbook of batteries*. Mcgraw-Hill, 2002.

[70] J Wang, SY Chew, ZW Zhao, S Ashraf, David Wexler, J Chen, SH Ng, SL Chou, and HK Liu. Sulfur–mesoporous carbon composites in conjunction with a novel ionic liquid electrolyte for lithium rechargeable batteries. *Carbon*, 46(2):229–235, 2008.

[71] Byoung Ho Jeon, Jin Hee Yeon, and In Jae Chung. Preparation and electrical properties of lithium–sulfur-composite polymer batteries. *Journal of materials processing technology*, 143:93–97, 2003.

[72] Yuriy V Mikhaylik and James R Akridge. Polysulfide shuttle study in the li/s battery system. *Journal of the Electrochemical Society*, 151(11):A1969–A1976, 2004.

[73] Qianfan WeiáSeh, Zhi andZhang, Weiyang Li, Guangyuan Zheng, Hongbin Yao, and Yi Cui. Stable cycling of lithium sulfide cathodes through strong affinity with a bifunctional binder. *Chemical Science*, 4(9):3673–3677, 2013.

[74] Uday Kasavajjula, Chunsheng Wang, and A John Appleby. Nano-and bulk-silicon-based insertion anodes for lithium-ion secondary cells. *Journal of Power Sources*, 163(2):1003–1039, 2007.

[75] Doron Aurbach. Review of selected electrode–solution interactions which determine the performance of li and li ion batteries. *Journal of Power Sources*, 89(2):206–218, 2000.

[76] Hui Wu, Guihua Yu, Lijia Pan, Nian Liu, Matthew T McDowell, Zhenan Bao, and Yi Cui. Stable Li-ion battery anodes by in-situ polymerization of conducting hydrogel to conformally coat silicon nanoparticles. *Nature communications*, 4, 2013.

[77] KM Abraham and Z Jiang. A polymer electrolyte-based rechargeable lithium/oxygen battery. *Journal of The Electrochemical Society*, 143(1):1–5, 1996.

[78] G Girishkumar, B McCloskey, AC Luntz, S Swanson, and W Wilcke. Lithium-air battery: Promise and challenges. *The Journal of Physical Chemistry Letters*, 1(14):2193–2203, 2010.

[79] P Poizot, S Laruelle, S Grugeon, L Dupont, and JM Tarascon. Nano-sized transition-metal oxides as negative-electrode materials for lithium-ion batteries. *Nature*, 407(6803):496–499, 2000.

[80] Dave Hurst and John Gartner. Electric vehicle market forecasts - global forecasts for light duty hybrid, plug-in hybrid, and battery electric vehicles: 2013-2020. Technical report.

[81] Jo Dewulf, Geert Van der Vorst, Kim Denturck, Herman Van Langenhove, Wouter Ghyoot, Jan Tytgat, and Kurt Vandeputte. Recycling rechargeable lithium ion batteries: Critical analysis of natural resource savings. *Resources, Conservation and Recycling*, 54(4):229–234, 2010.

[82] Jinqiu Xu, HR Thomas, Rob W Francis, Ken R Lum, Jingwei Wang, and Bo Liang. A review of processes and technologies for the recycling of lithium-ion secondary batteries. *Journal of Power Sources*, 177(2):512–527, 2008.

[83] Aswin Kumar. The lithium battery recycling challenge. *Waste Management World*, 12, August 2011. URL: `www.waste-management-world.com/articles/print/volume-12/issue-4/features/the-lithium-battery-recycling-challenge.html`.

[84] Thomas G. Goonan. Lithium use in batteries. Technical report.

[85] K Zaghib, J Shim, A Guerfi, P Charest, and KA Striebel. Effect of carbon source as additives in lifepo4 as positive electrode for lithium-ion batteries. *Electrochemical and Solid-State Letters*, 8(4):A207–A210, 2005.

[86] Seung-Taek Myung, Myung Hun Cho, Hyeon Taik Hong, Tae Hyuk Kang, and Chi-Su Kim. Electrochemical evaluation of mixed oxide electrode for li-ion secondary batteries: $Li_{1.1}Mn_{1.9}O_4$ and $LiNi_{0.8}Co_{0.15}Al_{0.05}O_2$. *Journal of power sources*, 146(1):222–225, 2005.

[87] Thomas F Fuller, Marc Doyle, and John Newman. Simulation and optimization of the dual lithium ion insertion cell. *Journal of the Electrochemical Society*, 141(1):1–10, 1994.

[88] Karen Thomas, John Newman, and Robert Darling. Mathematical modeling of lithium batteries. *Advances in lithium-ion batteries*, pages 345–392, 2002.

[89] Von DAG Bruggeman. Berechnung verschiedener physikalischer konstanten von heterogenen substanzen. i. dielektrizitätskonstanten und leitfähigkeiten der mischkörper aus isotropen substanzen. *Annalen der Physik*, 416(7):636–664, 1935.

[90] Richard Pollard and John Newman. Mathematical modeling of the lithium-aluminum, iron sulfide battery i. galvanostatic discharge behavior. *Journal of The Electrochemical Society*, 128(3):491–502, 1981.

[91] Francis B Hildebrand. *Advanced Calculus for Applications*. Prentice-Hall, 1976.

[92] Brian Bradie. *A Friendly Introduction to Numerical Analysis: With C and MATLAB Materials on Website*. Person Prentice Hall, 2006.

[93] Hongwen He, Rui Xiong, and Jinxin Fan. Evaluation of lithium-ion battery equivalent circuit models for state of charge estimation by an experimental approach. *Energies*, 4(4):582–598, 2011.

[94] Jorge Nocedal and Stephen J. Wright. *Numerical Optimization*. Springer, 2nd edition, 2006.

[95] Kathleen R Fowler, Jill P Reese, Chris E Kees, JE Dennis Jr, C Tim Kelley, Cass T Miller, Charles Audet, Andrew J Booker, Gilles Couture, Robert W Darwin, et al. Comparison of derivative-free optimization methods for groundwater supply and hydraulic capture community problems. *Advances in Water Resources*, 31(5):743–757, 2008.

[96] Jorge J Moré and Stefan M Wild. Benchmarking derivative-free optimization algorithms. *SIAM Journal on Optimization*, 20(1):172–191, 2009.

[97] Peter W. Jansen and Ruben E. Perez. Constrained structural design optimization via a parallel augmented Lagrangian particle swarm optimization approach. *Computers & Structures*, 89:1352–1366, 2011. doi:10.1016/j.compstruc.2011.03.011.

[98] Ruben E. Perez, Peter W. Jansen, and Joaquim R. R. A. Martins. pyOpt: a Python-based object-oriented framework for nonlinear constrained optimization. *Structural and Multidisciplinary Optimization*, 45(1):101–118, January 2012. doi:10.1007/s00158-011-0666-3.

[99] Philip E Gill and Walter Murray. The computation of Lagrange-multiplier estimates for constrained minimization. *Mathematical Programming*, 17(1):32–60, 1979.

[100] Kai Sedlaczek and Peter Eberhard. Using augmented lagrangian particle swarm optimization for constrained problems in engineering - using augmented Lagrangian particle swarm optimization for constrained problems in engineering. *Structural and Multidisciplinary Optimization*, 32(4):277–286, 2006.

[101] P.E. Gill, W. Murray, and M.A. Saunders. SNOPT: An SQP algorithm for large-scale constraint optimization. *SIAM Journal of Optimization*, 12(4):979–1006, 2002.

[102] Joaquim R. R. A. Martins and John T. Hwang. Review and unification of methods for computing derivatives of multidisciplinary computational models. *AIAA Journal*, 51(11):2582–2599, 2013. doi:10.2514/1.J052184.

[103] Joaquim R. R. A. Martins, Peter Sturdza, and Juan J. Alonso. The complex-step derivative approximation. *ACM Transactions on Mathematical Software*, 29(3):245–262, 2003. doi:10.1145/838250.838251.

[104] Wolfram Stadler. *Multicriteria Optimization in Engineering and in the Sciences*, volume 37. Springer, 1988.

[105] Wei Shyy, Young-Chang Cho, Wenbo Du, Amit Gupta, Chien-Chou Tseng, and Ann Marie Sastry. Surrogate-based modeling and dimension reduction techniques for multi-scale mechanics problems. *Acta Mechanica Sinica*, 27(6):845–865, 2011.

[106] Nestor V Queipo, Raphael T Haftka, Wei Shyy, Tushar Goel, Rajkumar Vaidyanathan, and P Kevin Tucker. Surrogate-based analysis and optimization. *Progress in Aerospace Sciences*, 41(1):1–28, 2005.

[107] Tushar Goel, Rajkumar Vaidyanathan, Raphael T Haftka, Wei Shyy, Nestor V Queipo, and Kevin Tucker. Response surface approximation of pareto optimal front in multi-objective optimization. *Computer Methods in Applied Mechanics and Engineering*, 196(4):879–893, 2007.

[108] W Choi and A Manthiram. Comparison of metal ion dissolutions from lithium ion battery cathodes. *Journal of The Electrochemical Society*, 153(9):A1760–A1764, 2006.

[109] XL Li, K Du, JM Huang, FY Kang, and WC Shen. Effect of carbon nanotubes on the anode performance of natural graphite for lithium ion batteries. *Journal of Physics and Chemistry of Solids*, 71(4):457–459, 2010.

[110] Marc Doyle, Thomas F Fuller, and John Newman. The importance of the lithium ion transference number in lithium/polymer cells. *Electrochimica Acta*, 39(13):2073–2081, 1994.

[111] John Newman. Optimization of porosity and thickness of a battery electrode by means of a reaction-zone model. *Journal of the Electrochemical Society*, 142(1):97–101, 1995.

[112] Venkat Srinivasan and John Newman. Design and optimization of a natural graphite/iron phosphate lithium-ion cell. *Journal of the Electrochemical Society*, 151(10):A1530–A1538, 2004.

[113] Sarah G Stewart, Venkat Srinivasan, and John Newman. Modeling the performance of lithium-ion batteries and capacitors during hybrid-electric-vehicle operation. *Journal of The Electrochemical Society*, 155(9):A664–A671, 2008.

[114] Wenbo Du, Amit Gupta, Xiangchun Zhang, Ann Marie Sastry, and Wei Shyy. Effect of cycling rate, particle size and transport properties on lithium-ion cathode performance. *International Journal of Heat and Mass Transfer*, 53(17):3552–3561, 2010.

[115] Venkatasailanathan Ramadesigan, Ravi N Methekar, Folarin Latinwo, Richard D Braatz, and Venkat R Subramanian. Optimal porosity distribution for minimized ohmic drop across a porous electrode. *Journal of The Electrochemical Society*, 157(12):A1328–A1334, 2010.

[116] Stephanie Golmon, Kurt Maute, and Martin L Dunn. Multiscale design optimization of lithium ion batteries using adjoint sensitivity analysis. *International Journal for Numerical Methods in Engineering*, 92(5):475–494, 2012.

[117] De Sumitava, Paul WC Northrop, Venkatasailanathan Ramadesigan, and Venkat R Subramanian. Model-based simultaneous optimization of multiple design parameters for lithium-ion batteries for maximization of energy density. *Journal of Power Sources*, 227:161–170, 2013.

[118] Joel C Forman, Saeid Bashash, Jeffrey L Stein, and Hosam K Fathy. Reduction of an electrochemistry-based Li-ion battery model via quasi-linearization and Padé approximation. *Journal of The Electrochemical Society*, 158(2):A93–A101, 2011.

[119] Venkatasailanathan Ramadesigan, Vijayasekaran Boovaragavan, J Carl Pirkle, and Venkat R Subramanian. Efficient reformulation of solid-phase diffusion in physics-based lithium-ion battery models. *Journal of The Electrochemical Society*, 157(7):A854–A860, 2010.

[120] Long Cai and Ralph E White. Reduction of model order based on proper orthogonal decomposition for lithium-ion battery simulations. *Journal of The Electrochemical Society*, 156(3):A154–A161, 2009.

[121] Paul WC Northrop, Venkatasailanathan Ramadesigan, Sumitava De, and Venkat R Subramanian. Coordinate transformation, orthogonal collocation, model reformulation and simulation of electrochemical-thermal behavior of lithium-ion battery stacks. *Journal of The Electrochemical Society*, 158(12):A1461–A1477, 2011.

[122] Wenbo Du, Nansi Xue, Amit Gupta, Ann M Sastry, Joaquim RRA Martins, and Wei Shyy. Optimization of limn2o4 electrode properties in a gradient-and surrogate-based framework. *Acta Mechanica Sinica*, 29(3):335–347, 2013.

[123] Philip E. Gill, Walter Murray, and Michael A. Saunders. SNOPT: An SQP algorithm for large-scale constrained optimization. *SIAM Review*, 47(1):99–131, 2005. `doi:10.1137/S0036144504446096`.

[124] Elizabeth D. Dolan and Jorge J. Moré. Benchmarking optimization software with performance profiles. *Mathematical Programming*, 91:201–213, 2002. 10.1007/s101070100263. URL: `http://dx.doi.org/10.1007/s101070100263`.

[125] Kalyanmoy Deb, Amrit Pratap, Sameer Agarwal, and TAMT Meyarivan. A fast and elitist multiobjective genetic algorithm: Nsga-ii. *Evolutionary Computation, IEEE Transactions on*, 6(2):182–197, 2002.

[126] Nansi Xue, Wenbo Du, Amit Gupta, Wei Shyy, Ann Marie Sastry, and Joaquim R. R. A. Martins. Optimization of a single lithium-ion battery cell with a gradient-based algorithm. *Journal of the Electrochemical Society*, 160(8):A1071–A1078, 2013.

[127] Marc Doyle, John Newman, Antoni S Gozdz, Caroline N Schmutz, and Jean-Marie Tarascon. Comparison of modeling predictions with experimental data from plastic lithium ion cells. *Journal of the Electrochemical Society*, 143(6):1890–1903, 1996.

[128] MD Levi and D Aurbach. Diffusion coefficients of lithium ions during intercalation into graphite derived from the simultaneous measurements and modeling of electrochemical impedance and potentiostatic intermittent titration characteristics of thin graphite electrodes. *The Journal of Physical Chemistry B*, 101(23):4641–4647, 1997.

[129] JR Dygas, M Kopeć, F Krok, D Lisovytskiy, and J Pielaszek. Conductivity and dielectric relaxation phenomena in lithium manganese spinel. *Solid State Ionics*, 176(25):2153–2161, 2005.

[130] DV Ragone. *Review of battery systems for electrically powered vehicles*. Society of Automotive Engineers, 1968.

[131] Peter Bäuerlein, Rudolf Herr, Matthias Kloss, Jörg Kümpers, Matthias Maul, and Eberhard Meissner. Advanced lithium ion cells with lithium manganese spinel. *Journal of power sources*, 81:585–588, 1999.

[132] T Horiba, K Hironaka, T Matsumura, T Kai, M Koseki, and Y Muranaka. Manganese type lithium ion battery for pure and hybrid electric vehicles. *Journal of power sources*, 97:719–721, 2001.

[133] Wilmont F Howard and Robert M Spotnitz. Theoretical evaluation of high-energy lithium metal phosphate cathode materials in Li-ion batteries. *Journal of Power Sources*, 165(2):887–891, 2007.

[134] Charles Monroe and John Newman. Dendrite growth in lithium/polymer systems a propagation model for liquid electrolytes under galvanostatic conditions. *Journal of the Electrochemical Society*, 150(10):A1377–A1384, 2003.

[135] Tetsuya Kawamura, Masami Makidera, Shigeto Okada, Kazumichi Koga, Norio Miura, and Jun-ichi Yamaki. Effect of nano-size $LiCoO_2$ cathode powders on Li-ion cells. *Journal of power sources*, 146(1):27–32, 2005.

[136] Thierry Drezen, Nam-Hee Kwon, Paul Bowen, Ivo Teerlinck, Motoshi Isono, and Ivan Exnar. Effect of particle size on $limnpo_4$ cathodes. *Journal of Power Sources*, 174(2):949–953, 2007.

[137] Mohamed Aklalouch, Rosa M Rojas, José Maria Rojo, Ismael Saadoune, and José Manuel Amarilla. The role of particle size on the electrochemical properties at 25 and at 55 c of the licr0. 2ni0. 4mn1. 4o4 spinel as 5v-cathode materials for lithium-ion batteries. *Electrochimica acta*, 54(28):7542–7550, 2009.

[138] Jane Yao, GX Wang, Jung-ho Ahn, HK Liu, and SX Dou. Electrochemical studies of graphitized mesocarbon microbeads as an anode in lithium-ion cells. *Journal of power sources*, 114(2):292–297, 2003.

[139] Robert Darling and John Newman. Modeling a porous intercalation electrode with two characteristic particle sizes. *Journal of The Electrochemical Society*, 144(12):4201–4208, 1997.

[140] Gowri S Nagarajan, JW Van Zee, and RM Spotnitz. A mathematical model for intercalation electrode behavior - i. effect of particle-size distribution on discharge capacity. *Journal of The Electrochemical Society*, 145(3):771–779, 1998.

[141] JM Tarascon and D Guyomard. The $Li_{1+x}Mn_2O_4$/C rocking-chair system: a review. *Electrochimica Acta*, 38(9):1221–1231, 1993.

[142] Y-H Chen, C-W Wang, Gao Liu, X-Y Song, VS Battaglia, and Ann Marie Sastry. Selection of conductive additives in li-ion battery cathodes a numerical study. *Journal of The Electrochemical Society*, 154(10):A978–A986, 2007.

[143] M Zhu, J Park, and AM Sastry. Particle interaction and aggregation in cathode material of li-ion batteries: a numerical study. *Journal of The Electrochemical Society*, 158(10):A1155–A1159, 2011.

[144] Dominique Guyomard and Jean-Marie Tarascon. Rocking-chair or lithium-ion rechargeable lithium batteries. *Advanced Materials*, 6(5):408–412, 1994.

[145] C-W Wang, Y-B Yi, AM Sastry, J Shim, and KA Striebel. Particle compression and conductivity in li-ion anodes with graphite additives. *Journal of the Electrochemical Society*, 151(9):A1489–A1498, 2004.

[146] Shashi K Shahi, G Gary Wang, Liqiang An, Eric Bibeau, and Zhila Pirmoradi. Using the Pareto set pursuing multiobjective optimization approach for hybridization of a plug-in hybrid electric vehicle. *Journal of Mechanical Design*, 134:094503–1–6, 2012.

[147] Xiaolan Wu, Binggang Cao, Xueyan Li, Jun Xu, and Xiaolong Ren. Component sizing optimization of plug-in hybrid electric vehicles. *Applied Energy*, 88(3):799–804, 2011.

[148] Yi-Hsuan Hung and Chien-Hsun Wu. An integrated optimization approach for a hybrid energy system in electric vehicles. *Applied Energy*, 98:479–490, 2012.

[149] Yuan Zou, Fengchun Sun, Xiaosong Hu, Lino Guzzella, and Huei Peng. Combined optimal sizing and control for a hybrid tracked vehicle. *Energies*, 5(11):4697–4710, 2012.

[150] Min-Joong Kim and Huei Peng. Power management and design optimization of fuel cell/battery hybrid vehicles. *Journal of Power Sources*, 165(2):819–832, 2007.

[151] Christian Fellner and John Newman. High-power batteries for use in hybrid vehicles. *Journal of Power Sources*, 85(2):229–236, 2000.

[152] Yuang-Shung Lee and Ming-Wang Cheng. Intelligent control battery equalization for series connected lithium-ion battery strings. *Industrial Electronics, IEEE Transactions on*, 52(5):1297–1307, 2005.

[153] Stephen W Moore and Peter J Schneider. A review of cell equalization methods for lithium ion and lithium polymer battery systems. *SAE Publication*, pages 01–0959, 2001.

[154] Wenbo Du, Nansi Xue, Ann M Sastry, Joaquim RRA Martins, and Wei Shyy. Energy density comparison of Li-ion cathode materials using dimensional analysis. *Journal of The Electrochemical Society*, 160(8):A1187–A1193, 2013.

[155] Fengchun Sun, Rui Xiong, Hongwen He, Weiqing Li, and Johan Eric Emmanuel Aussems. Model-based dynamic multi-parameter method for peak power estimation of lithiumion batteries. *Applied Energy*, 96(0):378 – 386, 2012.

[156] Kevin G Gallagher, Dennis Dees, and Paul Nelson. Phev battery cost assessment, 2011.

[157] Dong H Jang, Young J Shin, and Seung M Oh. Dissolution of spinel oxides and capacity losses in 4 V Li/$\mathrm{Li}_x\mathrm{Mn}_2\mathrm{O}_4$ cells. *Journal of The Electrochemical Society*, 143(7):2204–2211, 1996.

[158] Antti Lajunen. Evaluation of the benefits of using dual-source energy storage in hybrid electric vehicles. In *Vehicle Power and Propulsion Conference (VPPC), 2010 IEEE*, pages 1–6. IEEE, 2010.

[159] João P Trovão, Paulo G Pereirinha, Humberto M Jorge, and Carlos Henggeler Antunes. A multi-level energy management system for multi-source electric vehicles–an integrated rule-based meta-heuristic approach. *Applied Energy*, 105:304–318, 2013.

[160] Andrew F Burke. Batteries and ultracapacitors for electric, hybrid, and fuel cell vehicles. *Proceedings of the IEEE*, 95(4):806–820, 2007.

[161] John Christensen, Venkat Srinivasan, and John Newman. Optimization of lithium titanate electrodes for high-power cells. *Journal of the Electrochemical Society*, 153(3):A560–A565, 2006.

[162] Theodore P Adams, Dennis A Brumwell, Joseph S Perttu, and Charles G Supino. Dual battery power system for an implantable cardioverter defibrillator, December 13 1994. US Patent 5,372,605.

[163] Craig L Schmidt. High power implantable battery with improved safety and method of manufacture, April 24 2007. US Patent 7,209,784.

[164] Hong Gan and Esther S Takeuchi. Electrochemical battery for conversion of low rate energy into high rate energy by parallel discharging, August 22 2001. EP Patent 1,126,539.

[165] David M Spillman and Esther S Takeuchi. Electrochemical cell having multiplate and jellyroll electrodes with differing discharge rate regions, December 26 2000. US Patent 6,165,638.

[166] Thomas J Dougherty, Alan J Klebenow, Edward N Mrotek, David A Thuerk, and Maurice C Michaud. Dual battery system, November 10 1992. US Patent 5,162,164.

[167] Sarah G Stewart, Scott Ira Kohn, Kurt Russell Kelty, and Jeffrey Brian Straubel. Electric vehicle extended range hybrid battery pack system, March 6 2013. US Patent App. 13/787,421.

[168] Todd Alhart. GE demonstrates electric bus of the future, December 2010. URL: `www.genewscenter.com/Press-Releases/GE-Demonstrates-Electric-Bus-of-the-Future-2d43.aspx#downloads`.

[169] J Vetter, P Novak, MR Wagner, C Veit, K-C Möller, JO Besenhard, M Winter, M Wohlfahrt-Mehrens, C Vogler, and A Hammouche. Ageing mechanisms in lithium-ion batteries. *Journal of Power Sources*, 147(1):269–281, 2005.

[170] JO Besenhard, J Yang, and M Winter. Will advanced lithium-alloy anodes have a chance in lithium-ion batteries? *Journal of Power Sources*, 68(1):87–90, 1997.

[171] Xianke Lin, Jonghyun Park, Lin Liu, Yoonkoo Lee, AM Sastry, and Wei Lu. A comprehensive capacity fade model and analysis for li-ion batteries. *Journal of The Electrochemical Society*, 160(10):A1701–A1710, 2013.

[172] Christopher M DeLuca, Kurt Maute, and Martin L Dunn. Effects of electrode particle morphology on stress generation in silicon during lithium insertion. *Journal of Power Sources*, 196(22):9672–9681, 2011.

[173] Dirk Kehrwald, Paul R Shearing, Nigel P Brandon, Puneet K Sinha, and Stephen J Harris. Local tortuosity inhomogeneities in a lithium battery composite electrode. *Journal of The Electrochemical Society*, 158(12):A1393–A1399, 2011.

[174] Wenbo Du. *Multi-Scale Modeling, Surrogate-Based Analysis, and Optimization of Lithium-Ion Batteries for Vehicle Applications*. PhD thesis, University of Michigan, 2013.